


Ultrasound-responsive microbubbles and nanodroplets: A pathway to targeted drug delivery

Review Article**Author(s):**

Shakya, Gazendra; Cattaneo, Marco; Guerriero, Giulia; Prasanna, Anunay; Fiorini, Samuele; [Supponen, Outi](#) 

Publication date:

2024-03

Permanent link:

<https://doi.org/10.3929/ethz-b-000656596>

Rights / license:

[Creative Commons Attribution 4.0 International](#)

Originally published in:

Advanced Drug Delivery Reviews 206, <https://doi.org/10.1016/j.addr.2023.115178>



Ultrasound-responsive microbubbles and nanodroplets: A pathway to targeted drug delivery

Gazendra Shakya, Marco Cattaneo, Giulia Guerriero, Anunay Prasanna, Samuele Fiorini, Outi Supponen*

Institute of Fluid Dynamics, D-MAVT, Sonneggstrasse 3, ETH Zurich, Zurich, 8092, Switzerland

ARTICLE INFO

Keywords:

Microbubbles
Nanodroplets
Sonoporation
Cellular permeabilization
Endocytosis
Blood-brain barrier (BBB)
Enhanced Permeability and Retention effect (EPR)

ABSTRACT

Ultrasound-responsive agents have shown great potential as targeted drug delivery agents, effectively augmenting cell permeability and facilitating drug absorption. This review focuses on two specific agents, microbubbles and nanodroplets, and provides a sequential overview of their drug delivery process. Particular emphasis is given to the mechanical response of the agents under ultrasound, and the subsequent physical and biological effects on the cells. Finally, the state-of-the-art in their pre-clinical and clinical implementation are discussed. Throughout the review, major challenges that need to be overcome in order to accelerate their clinical translation are highlighted.

Contents

1. Introduction	2
1.1. Ultrasound-responsive agents for therapy	2
1.2. Pathway to drug delivery	3
2. Fabrication of ultrasound-responsive agents	3
2.1. Microbubble and droplet fabrication	3
2.2. Agent size constraints	4
2.3. Agent functionalization	5
3. Agent delivery	5
3.1. Agent dose <i>in vivo</i>	5
3.2. Enhanced Permeability and Retention (EPR) effect	6
4. Acoustic response	6
4.1. Microbubble response to ultrasound	6
4.2. Shell variability effects on microbubble response	7
4.3. Confinement effects on microbubble response	9
4.4. Drug release from microbubble shell	9
4.5. Microbubble stability under ultrasound	9
4.6. Mechanical Index (MI) as a parameter to predict microbubble-induced effects	9
4.7. Acoustic vaporization of phase-change agents	11
4.8. Dynamics of vaporized droplets	12
5. Agent-cell interaction	13
5.1. Mechanical action of bubbles near a substrate	13
5.2. Cellular mechanical permeabilization via microbubbles	14
5.3. Mechanical action and cellular mechanical permeabilization via phase-change droplets	16
5.4. Biophysical response of cells	17

* Corresponding author.

E-mail address: outis@ethz.ch (O. Supponen).

5.5. Experimental models to study enhanced permeabilization	18
5.6. Mechanical properties of cells and tissues	18
6. Drug delivery	19
6.1. Brain drug delivery	19
6.2. Solid tumors drug delivery	21
7. Future outlooks and conclusion	22
Declaration of competing interest	23
Data availability	23
Acknowledgements	23
References	23

1. Introduction

Systemic drug delivery suffers from two main limitations. First, it lacks specificity in targeting the treatment site. Drugs may circulate throughout the body, affecting both healthy and diseased tissues, which can lead to unwanted side effects. Second, it faces limited penetration because some drugs encounter difficulties in crossing physiological barriers, such as the endothelium and in particular, the blood-brain barrier (BBB). Therefore, the therapeutic results of medications typically fall short due to the limited ability of the drug to reach and act at the intended target [1]. To overcome these limitations, various novel intravascular delivery systems have been developed to achieve targeted drug delivery. These include solid nanoparticles [2], nanocrystals [3], protein-based agents [4], cell-based agents [5], polymer-drug conjugates [6], liposomes [7,8], and more. These carriers are engineered to encapsulate drugs, protect them from degradation, and release them at the desired location. Nevertheless, they encounter the same biological barriers to delivery as other therapeutics, which ultimately restricts their clinical efficacy. On the other hand, ultrasound-responsive agents, such as microbubbles and nanodroplets, have demonstrated meeting both the demands of high specificity and deep penetration. They achieve targeted delivery through interface functionalization and by leveraging the high spatial resolution offered by clinical ultrasound systems, and they enhance penetration by transiently rupturing biological barriers via the mechanical stress generated by the agents' kinetic activity in response to ultrasound. Significantly, as of now, the utilization of ultrasound-activated microbubbles stands as the sole non-invasive, localized, and reversible method for opening the BBB and administering drugs to the brain [9]. This technique has proven to be an effective treatment for the early onset of Alzheimer's, Huntington's and Parkinson's diseases [10–12], brain tumors [13–15], and amyotrophic lateral sclerosis [16]. The therapeutic potential of ultrasound-responsive agents also extends beyond the central nervous system, encompassing the cardiovascular system and all highly vascularized tissues and organs. They can effectively deliver plasmid DNA and drugs for treating myocardial infarction [17], atherosclerosis [18], and solid tumors [19,20].

1.1. Ultrasound-responsive agents for therapy

Micron-sized bubbles are the most frequently used agents for ultrasound-mediated drug delivery. Bubbles have an innate ability to focus acoustic energy, which can frequently result in detrimental and undesirable consequences. One illustrative instance is the cavitation of bubbles within underwater turbines, where bubbles form and then collapse, resulting in substantial damage to the machinery [21]. However, when controlled, this energy-focusing ability can be harnessed for a large number of biomedical applications. Upon harmonic acoustic driving, the bubbles undergo a periodic succession of expansion and compression phases, which leads to the emission of sound and the generation of mechanical stress on the surroundings. The first effect established bubbles as a widely used ultrasound contrast agent in perfusion imaging across multiple organs [22–26]. The second outcome has

opened avenues for their utilization in therapeutic applications such as sonothrombolysis, for dissolving blood clots in acute ischemic stroke ([27,28], as well as facilitating drug delivery for the treatment of a wide range of diseases. The bubbles employed in clinical applications have a diameter of less than 10 μm to avoid flow blockages in capillary vessels, and hence, are referred to as microbubbles. Fortunately, the resonance frequencies of microbubbles within this size range conveniently match the working frequencies of clinically approved diagnostic ultrasound systems, which range from 1 MHz to 10 MHz, ensuring optimal efficiency in converting acoustic energy into bubble kinetic motion. A major advantage of using microbubbles as a therapeutic agent lies in their commercial availability and clinical approval for ultrasound imaging applications (examples of approved microbubbles include Optison™ from GE HealthCare, Sonazoid™ from GE HealthCare, Lumason/SonoVue® from Bracco Diagnostics, and Definity® from Lantheus Medical Imaging, Inc.).

Micron- and sub-micron-sized liquid droplets are another class of ultrasound-responsive agents. These droplets can be considered as microbubble precursors that can be vaporized into bubbles using acoustic activation. This process, known as Acoustic Droplet Vaporization (ADV), was first introduced in the 1990s as an alternative method to enhance ultrasound contrast [29–31]. The rapid vaporization of droplets, as a result of ADV, can contribute to the enhanced vascular permeability, which can improve drug uptake in tissues, and in extreme cases, even cause cell death [32–36]. Hence, droplets are currently being studied as potential agents in several therapeutic applications including gas embolotherapy [37], ablation techniques such as lithotripsy [38], histotripsy [39], and thermal ablation [40], as well as targeted drug delivery [41]. Alternatively, droplet vaporization can also be achieved using techniques such as optical excitation [42], magnetic excitation [43], microwave excitation [44], or combination of any of the above [45]. Nanodroplets present most of the advantages of microbubbles as ultrasound-responsive agents with certain additional benefits. With respect to their microbubble counterparts, nanodroplets have longer circulation lifetimes *in vivo* due to their smaller size, which prevents rapid clearance by phagocytic cells, and provides higher stability against dissolution [46]. Additionally, since nanodroplets are limited scatterers of sound until they are converted into microbubbles, the acoustic field is less distorted while passing through nanodroplet clouds. This ensures better focus of the acoustic beam within the tissue, enabling better targeting of nanodroplets and preventing unnecessary bioeffects due to the scattering [47]. Furthermore, nanodroplets (and in general nanocarriers) can also extravasate in the leaky vasculature of tumor tissue [48] leading to localized creation of microbubbles upon drop vaporization for highly targeted drug delivery and contrast enhancement [47]. However, the major limitations of using droplets as compared to microbubbles, are the prohibitively high acoustic pressure amplitudes for activation [46,49], and the limited control of the vaporization-induced mechanical action.

Other ultrasound-responsive agents include solid particles that entrap and stabilize tiny gas pockets. These particles (usually sub-micrometric) can be used as cavitation nuclei to generate bubbles, and hence provide the therapeutic advantages of microbubbles on-demand.

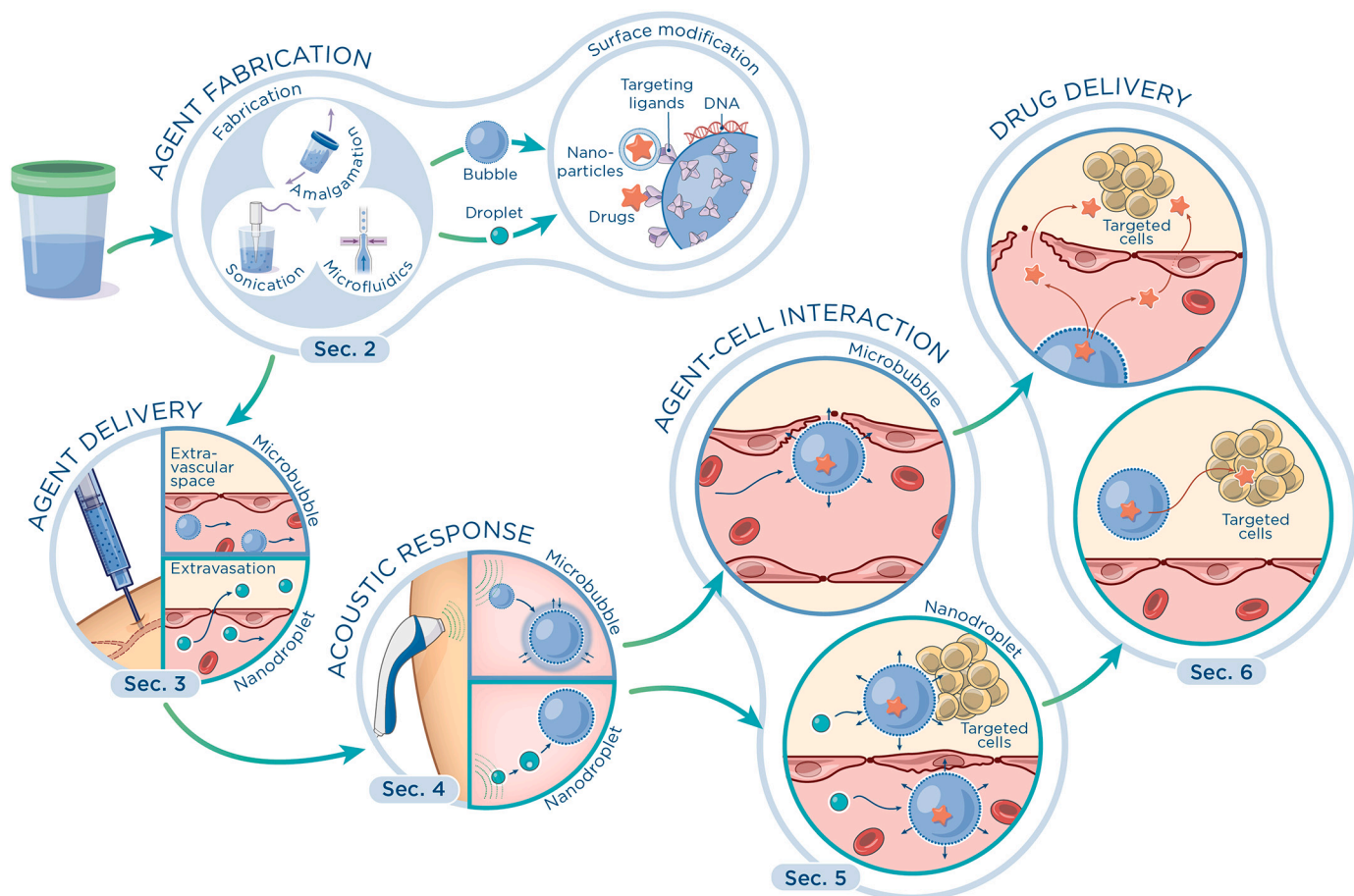


Fig. 1. Schematic overview highlighting the role of ultrasound-responsive agents and their pathway throughout the drug delivery process. Illustration by Gaia Codoni.

These particles can take various forms ranging from polymeric cup-shaped nanoparticles [50], to gold nanocones [51], to mesoporous silica nanoparticles [52]. However, the scope of this review is limited to the most common ultrasound-responsive agents, namely, microbubbles and nanodroplets. Throughout this review, unless specified otherwise, “agent” indicates both microbubbles and nanodroplets.

1.2. Pathway to drug delivery

Despite the numerous successful pre-clinical and clinical trials using ultrasound-responsive agents, the intricate physical, biophysical, and biological processes involved in the enhanced permeability mechanism pose a formidable challenge to relate the specific agent activity with the resulting bioeffects, and therefore, exert full control on the therapeutic procedure. Furthermore, the response of individual ultrasound-responsive agents inherently varies, influenced by their unique microstructure and the surrounding microenvironment’s geometry and physical properties. Additionally, the mechanisms identified *in vitro* may differ from those observed *in vivo*. This review aims to provide a comprehensive and critical examination of the existing body of knowledge regarding microbubbles and nanodroplets, and their use in therapy. The pressing open questions which hinder the clinical translation of these agents are particularly emphasized. The structure of this review covers sequentially the distinct phases comprising the therapy based on ultrasound-responsive agents, which are graphically summarized in Fig. 1. We will begin by delving into the fabrication process of these agents and their drug-loading capabilities (Sec. 2). Following that, we will explore the intricate journey of these agents within the body, shedding light on the challenges associated with their successful delivery to specific target areas (Sec. 3). Moving forward, we will dive into

the acoustic response of these agents, examining the theoretical aspects governing their behavior, the effect of confinement, their stability when subjected to ultrasound, and the development of safety metrics to assess their bioeffects (Sec. 4). Subsequently, we will investigate the mechanical effects induced by these agents on the vasculature wall and the resulting biological responses that contribute to enhanced drug permeability (Sec. 5). Lastly, our journey will culminate with an exploration of the intricacies involved in delivering drugs to target tissues (Sec. 6).

2. Fabrication of ultrasound-responsive agents

The initial step in the drug delivery pathway involves creating specialized agents designed to facilitate ultrasound-induced targeted drug delivery. In the following sections, we will explore various methods for agent fabrication, discuss drug-agent conjugation, and highlight their respective limitations.

2.1. Microbubble and droplet fabrication

Microbubbles and droplets share similar structural chemistry and fabrication mechanisms (see Fig. 2). Both agents contain a core material, composed of a gas, (for microbubbles), or liquid (for droplets), and a surfactant shell that stabilizes the core material against dissolution by reducing the surface tension at the interface. There are a variety of gas species that have been used for microbubbles. Commercial microbubbles contain an inert, non-metabolizable, heavy molecular weight gas, typically perfluorocarbons (PFC), such as octafluoropropane (OFP, C_3F_8 , in Optison™ and Definity/Luminy™) or perfluorobutane (PFB, C_4F_{10} , in Sonazoid™), or sulfur hexafluoride (SF_6 , in Lumason/Sonovue™), to prevent dissolution and improve the stability

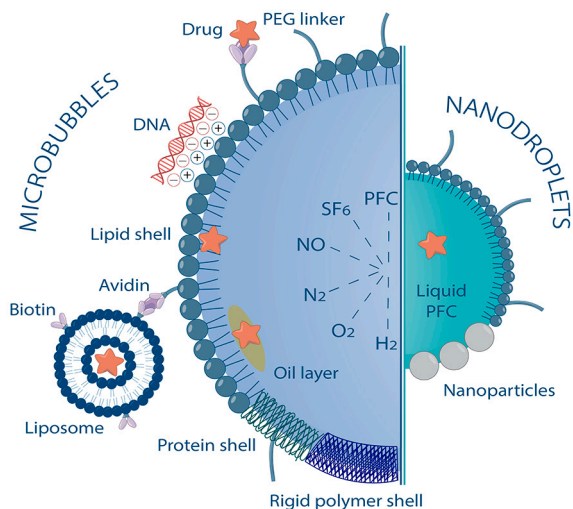


Fig. 2. The schematic depicts the possible components of the core, the different types of shell materials, and the diverse drug-encapsulation techniques that are employed for microbubbles and nanodroplets. Nanodroplets with a lipid shell have similar functionalization capabilities as a lipid-coated microbubble.

of the bubbles [53]. The gas content of microbubbles fabricated in-house is more diverse and tailored to their specific applications. In addition to PFC and SF₆, therapeutic gases such as nitric oxide (NO) [54,55], oxygen (O₂) [56,57], and hydrogen (H₂) [58] can be used for therapeutic applications. Furthermore, gases such as air [59], nitrogen (N₂) [60], as well as various mixtures [55,57] have also been used. However, there are still uncertainties regarding the persistence lifetimes of the gas core *in vivo* which will be discussed in Sec. 3.

There is also a similar variability in the choice of surfactants, but for better bio-compatibility, proteins, and phospholipids are the most popular choices. The first clinically-approved microbubbles were the albumin-coated Albunex[®] and Optison[™] (approved in 1993 and 1997, respectively) [61]. Albumin shells are fairly rigid, which makes them less responsive to ultrasound and often raises concerns about their potential immunogenicity due to their animal-derived origin [61]. In response to these limitations, the adoption of phospholipid shells has become the prevailing method for producing microbubbles. Lipid-coated microbubbles are more echogenic, biocompatible, and easy to manufacture [62]. Lipids naturally adsorb on gas-liquid interfaces, arranging themselves into a monolayer with lipid hydrophilic head groups oriented outward. A diverse array of lipids is available to tailor both the stability and functionality of bubbles. The common formulation of the phospholipid shell consists of two components: a matrix lipid that stabilizes the shell by providing cohesion, and an emulsifying lipid, usually containing a polymeric group, such as polyethylene glycol (PEG), that helps with the lipid assembly, prevents coalescence, provides stealth capability against the immune system, and acts as a tether for further functionalizations.

Several studies have been dedicated to evaluating the adverse effects of commercial contrast-enhanced ultrasound agents. Clinical studies performed to assess the safety of Optison[™] and Definity[®] reported minimal patients who suffered severe adverse reactions due to the agents [63,64]. Similar studies performed for Sonazoid[™] [65] and the SF₆-based Lumason/Sonovue[®] [66] have shown that the microbubbles were safe in both clinical and animal studies, and patients showing acute or adverse effects were few and far in between.

Emulsions for ADV, on the other hand, are made of micrometric and nanometric liquid PFC droplets stabilized by a shell. The biocompatibility of PFCs has been reported extensively and they have been used in several clinical applications [67,68]), including in microbubbles, as mentioned previously. Light perfluorocarbons, such as OFP and PFB are generally used as droplet cores due to their high vapor pressures which

makes them easier to vaporize [69]. Nevertheless, combined with their high water-solubilities, this also makes them thermodynamically unstable. For this reason, the use of heavier PFCs, such as perfluoropentane (PFP, C₅F₁₂) and perfluorohexane (PFH, C₆F₁₄), which present lower vapor pressures and water-solubility is favored, despite their reduced vaporizability. Similarly to microbubbles, surfactants such as proteins, fluorosurfactants, and phospholipids can be employed as shell materials [70]. Other typical shell materials for encapsulation include polymers [71,72] and solid nanoparticles [73,74].

Amalgamation and tip-sonication are the two most common techniques to fabricate microbubbles and droplets. Both processes involve mechanical agitation to incorporate the dispersed phase (which will constitute the core of the agents [75,76]) into the aqueous continuous phase. Amalgamation mechanically mixes the two phases whereas tip-sonication employs surface agitation to entrap the dispersed phase into the continuous phase [62,75,76]. Both processes generate bubbles and droplets with a polydisperse size distribution, ranging from sub-micrometer to tens of micrometers in diameter. If monodispersity in the bubble sizes is required, differential centrifugation has been shown to be an effective solution to isolate specific bubble sizes [62]. Similarly, microfluidic techniques have also been developed to generate microbubbles as well as droplets with better consistency and control over their sizes. These are usually flow-focusing devices, where the dispersed phase flow is focused in between two continuous phase flows through a physical constriction or a tight junction, in order to pinch off uniform sized packets of dispersed phase fluid [77,78]. However, microfluidic fabrication techniques suffer from complicated setups and lower throughput than traditional fabrication techniques, such as sonication. New membrane emulsification techniques using Shirasu Porous Glass (SPG) membranes have also been developed providing higher fabrication speeds, although with poor agent monodispersity when compared to microfluidic techniques [79,80]. Another popular technique to generate droplets is using the method of microbubble condensation, where existing microbubbles are subjected to the appropriate pressure and temperature to condense them into droplets [81]. Readers interested in the details of microbubble and nanodroplet fabrication are referred to the reviews by Stride et al. [82] and Lea-Banks et al. [47].

2.2. Agent size constraints

The vascular environment sets a distinct upper size limit for agents, approximately 10 μm [83], to avoid the occurrence of blood flow obstructions. Conversely, there is no theoretical lower limit for the size of agents. As a consequence, nanobubbles have gathered interest as an imaging and drug delivery agent [84], as their smaller sizes would allow for vascular extravasation. However, some controversy currently exists relating to the contrast enhancement capabilities of nanobubbles, as they are theoretically too small to resonate at clinical frequencies [46,85]. Additionally, since therapeutic efficacy relies on the mechanical action generated by the agents, the non-resonant size of the nanobubbles raises questions on their use for therapy as well. Hence, further investigation is needed to take advantage of the nanometric size for clinical applications.

The size of microbubbles also plays a crucial role in determining how they respond to incoming acoustic waves, as discussed in Sec. 4.1. Each bubble size corresponds to a specific resonant frequency at which it exhibits its peak response. As a result, monodisperse resonant-sized bubbles have demonstrated superior delivery potential compared to polydisperse bubbles in pre-clinical studies [86]. Nonetheless, in the majority of clinical trials, polydisperse bubble populations are commonly employed. Additional studies involving monodisperse bubble populations would be valuable for assessing the effectiveness of employing resonant-sized bubbles within the clinical context.

Size also represents an important parameter for droplet vaporization. Following the phase change from liquid to gas, the resulting bubble diameter is five to ten times greater than the initial droplet diameter

[87,88] due to the lower density of the vapor phase and the diffusion of non-condensable gas in the newly formed bubble [89]. While large post-vaporization bubbles may prove beneficial for embolization studies, in drug delivery applications, they could result in life-threatening restrictions of the blood flow [46]. Furthermore, as the acoustic vaporization of droplets is highly sensitive to the acoustic frequency and droplet size, with smaller droplets requiring higher frequencies for successful vaporization, selecting the appropriate droplet size is crucial [90], as discussed in Sec. 4.7.

2.3. Agent functionalization

In addition to inducing mechanical stress on cells to enhance permeabilization, ultrasound-responsive agents can also serve as drug carriers, leveraging various drug conjugation strategies, as depicted in Fig. 2. Some drugs can be linked directly to the lipid shell by taking advantage of the functionalized PEG entities [91]. For other drugs, this direct attachment may not be feasible. However, if these drugs are hydrophilic, they can be encapsulated within liposomes, which can then be functionalized to bind with the outer lipid shell [92]. Hydrophobic drugs, on the other hand, can be adsorbed into the hydrophobic tail of the lipids forming the shell [93] or dissolved within an oil layer in the microbubble [94]. In the case of droplets, hydrophobic drugs can be dissolved directly in the hydrophobic liquid core [95]. Additionally, charged payloads (e.g., DNA), can be electrostatically attached to the shell by using charged lipids [96].

The agents can also be functionalized to target specific receptor molecules in diseased tissues. This can be achieved by adorning the surface of the agent with specific ligand molecules using PEG functionalization [91,97]. For this purpose, various bio-conjugation schemes, such as avidin-biotin [98], maleimide-thiol [99], click-chemistry [100], among others, can be leveraged. A more detailed review of such conjugation schemes is provided by Mulvana et al. [91].

3. Agent delivery

The emulsion containing ultrasound-responsive agents is typically injected intravenously and is distributed throughout the body by the circulatory system. The change in ambient temperature, as the agents are moved from storage (typically around 4 °C) to the human body (around 37 °C), does not affect microbubbles significantly [102]. However, as nanodroplets are thermodynamically metastable, an increased ambient temperature could induce spontaneous vaporization of droplets.

Within the human vasculature, the agents are constantly threatened by the immune system, which tries to attack what is perceived as a foreign substance and initiate its phagocytic clearance. Larger agents are more prone to undergo phagocytosis through the mononuclear phagocyte system, primarily within the liver and kidney, due to their complement-dependent activation uptake, which significantly decreases their circulation lifetime [103–107]. Therefore, PEGylated molecules are used to increase the steric hindrance of the agents to prevent complement activation and increase their circulation lifetime *in vivo* [108,109]. With repeated administration, these agents also prompt phagocytic cells to recognize PEG-stabilized foreign entities due to anti-PEG antibody production [106]. Consequently, the following doses are cleared more quickly, leading to a reduction in their therapeutic effectiveness. This is called Accelerated Blood Clearance (ABC). Factors affecting ABC and methods to prevent it are further discussed in the review by Abu Lila et al. [109].

Gaseous agents are also removed by dissolution and consequent expulsion through the lungs. During storage, microbubbles are maintained in a solution saturated with the heavy gases that constitute their core to ensure minimal dissolution. However, the main dissolved mixture within circulation is air [101]. When a coated microbubble with a core of slow-diffusing gas, such as PFC or SF₆, is rapidly introduced into

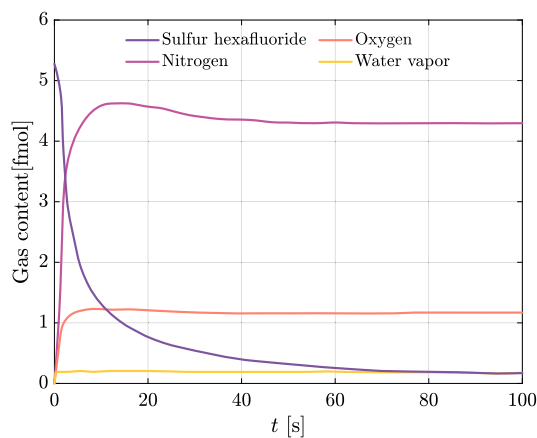


Fig. 3. Predicted time-evolution of the gas composition for a lipid-coated microbubble with an SF₆ gas core, immersed in an air-saturated aqueous medium. Figure reproduced with permission from the work by Kwan and Borden [101].

a surrounding medium of fast-diffusing gases such as nitrogen or oxygen, it undergoes immediate expansion driven by the rapid influx of gases from its surroundings. As a consequence, the increased gas-liquid interface cannot be entirely covered by the lipid shell anymore, and the surface tension starts to rise, causing the bubble dissolution due to the development of Laplace overpressure. The gas originally present within the bubble is expelled and eventually completely substituted by the gases dissolved in the surrounding liquid. Dissolution ceases when the bubble reaches a size that ensures a full lipid coverage of the surface, thus reducing surface tension to zero and eliminating the Laplace pressure. Kwan and Borden [101] developed a gas dynamics model based on a modified Epstein-Plesset relation to infer the evolution of the bubble gas composition from experimental radius-time curves. The model revealed that the complete replacement of the heavy gas initially contained in the bubble occurs within a few tens of seconds when the bubble is immersed in an air-saturated medium, as shown in Fig. 3 [101]. In light of these predictions, further studies dedicated to the *in vivo* gas exchange behavior are needed to justify the use of microbubbles as therapeutic gas carriers.

For similar concentrations injected ($\approx 10^8$ mL⁻¹), PFB nanodroplets have shown much higher stability, presenting half-lives of around 11 min as compared to a half-life of 3.5 min for microbubbles. It is also to be noted that droplets made of a lighter fluorocarbon, such as OFP, present lower persistence time, comparable to microbubbles [110]. Nonetheless, the dissolution of the agents is an essential process for removing any non-physiological gases present in the vasculature after the treatment is completed. It has been shown *in vivo* that more than half of the injected PFB concentration is removed within 20 min after injection, with only 1.9% of PFB remaining within the animal body after 24 h [111].

3.1. Agent dose in vivo

The dosage of microbubbles should be high enough to enable sufficient bubble-cell interactions [19], and low enough to prevent the formation of large bubble clusters, which distorts the acoustic field, reduces the bubble-cell interactions, and could cause large blockages in vessels [112]. In addition, high dosages may possibly increase off-target bioeffects [113]. Although the safety of the ultrasound contrast agents approved for clinical use has been studied extensively in both retrospective and prospective trials [114], there is currently no clinically approved regulation regarding drug delivery applications. Therefore, in their clinical trial, Dimcevski et al. [19] followed the ethical requirements set by ultrasound contrast agent imaging standards [113]. This translated to injecting 0.5 mL of microbubble emulsion (SonoVue®) followed by 5 mL of saline injection every 3.5 min after

the intravenous injection of the chemotherapeutic drug, with the vial lasting for 31.5 min. The formulation characteristics of additional commercial, FDA-approved contrast agents can be found in Borden et al. [114], as well as their concentration. In the case of nanodroplets, post-vaporization microbubbles could distort the acoustic field and shield other droplets [115], meaning that increasing droplet concentration does not necessarily increase the drug delivery potential. Acoustic radiation forces could also influence the post-ADV microbubbles, possibly leading to their coalescence [116,117]. This further increases the chances of unplanned embolization and blockages in blood vessels, causing oxygen deprivation in the surrounding tissue [46]. While useful for tumor embolization [37,118], this scenario is unsuitable for drug delivery. As of now, there are no clinical standards for optimum nanodroplet dosage, and more dedicated studies are necessary to find this dose.

3.2. Enhanced Permeability and Retention (EPR) effect

Nanocarriers offer distinct advantages in drug delivery approaches, such as the possibility to leverage the enhanced permeability and retention effect (EPR) at the tumor site [48]. They can infiltrate and passively accumulate in tumors, owing to their leaky vasculature, and be retained due to poor lymphatic drainage, as demonstrated by Helfield et al. [119], who showed that sub-micron droplets can extravasate to a much higher degree in mice fibrosarcoma models as compared to healthy kidneys. However, the EPR effect exhibits significant variability both within tumors and among different tumor types, typically resulting in the accumulation of merely 0.7% of administered nanoparticles at the intended target site [120]. However, clinical studies have not yet been able to replicate the promising results demonstrated in preclinical studies.

4. Acoustic response

Following the administration of the agents, ultrasound is applied to the treatment area, which causes microbubbles to undergo a periodic succession of radial expansion and contraction phases owing to their large compressibility and the droplets to be vaporized and turn into bubbles. These events being extremely quick, their comprehension and characterization have required the development of a specialized microscopy system with exceptional temporal resolution [121,122]. In this section, we review the accumulated knowledge gathered in the past decades regarding the acoustic response of ultrasound-responsive agents and we highlight the areas requiring further clarifications.

4.1. Microbubble response to ultrasound

The radial motion of a spherical bubble of radius $R(t)$, immersed in an incompressible, homogeneous, unbounded medium, is governed by the equation commonly referred to as the Rayleigh–Plesset equation [123–127]:

$$\rho_l \left(R\ddot{R} + \frac{3}{2}\dot{R}^2 \right) = P_B - P_F, \quad (1)$$

which is derived from the incompressible Navier-Stokes equations leveraging spherical symmetry. The left part of the equation represents the fluid inertia surrounding the bubble with the over-dots denoting time derivatives, and ρ_l the liquid density. The right part represents the difference between the work per unit volume done due to the presence of a cavity in the fluid, P_B , and the work per unit volume done due to the presence of the fluid, P_F . P_B can be expressed as:

$$P_B = p_g + p_v + \Sigma(R, \dot{R}) + H(R, \dot{R}) \quad (2)$$

where p_g is the gas pressure inside the bubble, p_v is the vapor pressure inside the bubble, $\Sigma(R, \dot{R})$ is the pressure contribution from the

interface, and $H(R, \dot{R})$ is the viscous contribution from the fluid. Owing to its small value compared to other terms, the vapor pressure is commonly neglected. The damping of the bubble dynamics by the radiated sound can become an important factor when $|\dot{R}|/c_1$, where c_1 is the speed of sound of the medium, approaches unity. A widely adopted approach to account for it, in the context of coated bubbles, is to add a corrective factor to Eq. (2):

$$\frac{R}{c_1} \frac{dp_g}{dt}. \quad (3)$$

The derivation of this term and alternative methods to account for acoustic reradiation can be found in the review article by Brenner, Hilgenfeldt, and Lohse [128]. The gas pressure, p_g , is often modeled through the approximation of a polytropic process as:

$$p_g = p_{g,0} \left(\frac{R_0}{R} \right)^{3n}, \quad p_{g,0} = p_\infty + \frac{2\sigma_0}{R_0} - p_v, \quad (4)$$

with $p_{g,0}$ being the bubble internal pressure at rest, R_0 the equilibrium bubble radius, and n the polytropic index. The bubble's internal pressure at rest is given by the ambient pressure, p_∞ , and the Laplace pressure caused by the interfacial surface tension at equilibrium, σ_0 . It should be noted that the validity of the polytropic process approximation is violated when heat transfer through advection and conduction are roughly equal, i.e., when the Péclet number is close to one. Moreover, this approximation results in no energy loss associated with the gas heat exchange. The interested reader may refer to the work by Prosperetti, Crum, and Commander [129] for further insights and consult the study by Cattaneo and Supponen [122] for a practical example of an alternative model's application. Chatterjee and Sarkar [130] were the first to suggest modeling the bubble phospholipid coating as a two-dimensional continuum, appropriate to describe interfaces only a few molecules thick. Moreover, they proposed to describe the coating as viscoelastic, expressing its pressure contribution $\Sigma(R, \dot{R})$ as:

$$\Sigma_{CS}(R, \dot{R}) = -2 \frac{\sigma_0 + E_s(J-1)}{R} - 4\kappa_s \frac{\dot{R}}{R^2}, \quad (5)$$

where E_s is the interfacial dilatational modulus, κ_s is the interfacial dilatational viscosity, and $J = R^2/R_0^2$, is the relative area deformation. For a deeper understanding of the origins behind the various terms, we recommend referring to the comprehensive review article authored by Jaansson, Anderson, and Vermant [131]. To account for the pronounced nonlinear effects observed in the dynamics of phospholipid-coated microbubbles, Marmottant et al. [132] introduced a phenomenological extension drawing inspiration from the surface pressure area isotherms of phospholipid monolayers [133], yielding

$$\Sigma_M(R, \dot{R}) = -2 \frac{\sigma(R)}{R} - 4\kappa_s \frac{\dot{R}}{R^2},$$

$$\text{with } \sigma(R) = \begin{cases} 0, & \text{for } R \leq R_{\text{buckling}} \\ \sigma_0 + E_s(J-1), & \text{for } R_{\text{buckling}} < R < R_{\text{rupture}} \\ \sigma_{\text{water}}, & \text{for } R \geq R_{\text{rupture}} \end{cases} \quad (6)$$

which encompass: (i) the coating's buckling, occurring when the bubble is compressed to a radius below R_{buckling} , leading to a tension-free interface; (ii) the coating's rupture, occurring as the bubble expands beyond R_{rupture} , causing the complete exposure of the gas core to the surrounding fluid, i.e., a surface tension equivalent to that of a pure gas-water interface ($\sigma_{\text{water}} = 72.8 \text{ mN m}^{-1}$); and (iii) the elastic regime in between. The viscous contribution of the fluid $H(R, \dot{R})$ for an incompressible, Newtonian fluid reads:

$$H(R, \dot{R}) = -4\mu_1 \frac{\dot{R}}{R}, \quad (7)$$

where μ_1 is the dynamic viscosity of the medium. We encourage readers with an interest in modeling bubble response in more rheologically complex fluids to refer to the review article authored by Dollet, Marmottant, and Garbin [134]. When employing the polytropic approximation

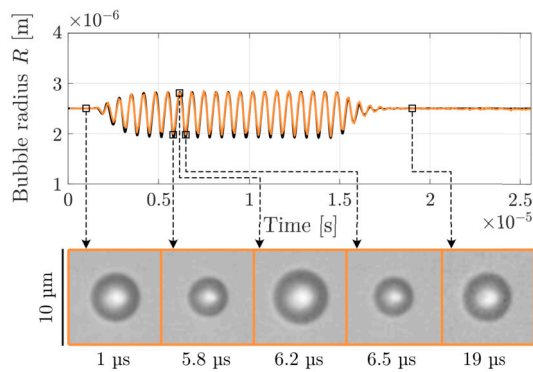


Fig. 4. Comparison between the experimental radial time evolution, in orange, and the theoretical one, in black, of a coated bubble with an equilibrium radius R_0 of $2.5 \mu\text{m}$ driven by a 20-cycle ultrasound pulse with a frequency of 1.5 MHz and a pressure amplitude of 40 kPa . The bubble is positioned away from boundaries by using optical tweezers in order to avoid wall effects on the bubble response. Selected snapshots of the bubble dynamics are shown in the orange boxes. The shell parameters used for the simulation are: $\kappa_s = 10 \times 10^{-9} \text{ kg s}^{-1}$, $E_s = 1 \text{ N m}^{-1}$, $\sigma_0 = 0 \text{ mN m}^{-1}$. Figure reproduced from the work by Cattaneo and Supponen [122] with permission from the Royal Society of Chemistry.

for the gas, it is customary to double the dynamic viscosity value to incorporate thermal damping (when the ambient fluid is water) [135]. The last term in Eq. (1), P_F , consists of the ambient pressure p_∞ and the time-dependent acoustic driving $p_d(t)$:

$$P_F = p_\infty + p_d(t). \quad (8)$$

One can treat the acoustic stimulation as spatially uniform due to the significantly smaller size of the microbubbles compared to the typical wavelength of clinical acoustic driving. For an extended review of the physics of coated microbubbles, one can consult the article by Versluis et al. [135].

The response of a bubble to an acoustic field is commonly classified as either “stable cavitation” or “inertial cavitation” [136]. Stable cavitation occurs at low acoustic pressures and is characterized by the stable, mild oscillation of the bubble around its equilibrium size over multiple cycles. Conversely, inertial cavitation occurs for intense acoustic driving and results in large bubble expansions followed by abrupt and forceful collapses, ultimately causing the bubble to fragment within a few cycles. Nevertheless, it is important to clarify that using the term “cavitation” in this context is inaccurate, as it actually pertains to the formation of vapor bubbles due to a decrease in pressure within a liquid medium. An example of stable cavitation is illustrated in Fig. 4 which showcases the radial response of a coated bubble with an equilibrium radius R_0 of $2.5 \mu\text{m}$ driven by an acoustic forcing, $p_d(t) = p_a \sin(2\pi f t)$, having a frequency f of 1.5 MHz and a pressure amplitude p_a of 40 kPa . The experimental radius-time curve is compared with the theoretical radial evolution calculated with the same theoretical foundation outlined in this section.

Fig. 5, compares the frequency response of a coated and an uncoated bubble, both having an equilibrium radius R_0 of $2.5 \mu\text{m}$. The frequency response relates the normalized response energy, $|x/p_a|^2$, where x is the normalized maximum amplitude, $x = R_{\text{max}}/R_0 - 1$, with the forcing frequency, f . The most important difference lies in the remarkably lower response amplitude of coated bubbles compared to uncoated ones owing to viscous dissipation mechanisms between lipid molecules. Secondly, coated bubbles exhibit a higher resonance frequency due to the added elasticity from the coating. Nevertheless, this trait fades rapidly as the driving pressure increases, as can be clearly seen comparing the response for an acoustic driving pressure $p_a = 50 \text{ kPa}$, a typical value employed in echography with microbubbles, and the one for an infinitely small driving pressure ($p_a = 0^+ \text{ kPa}$), computed by lineariz-

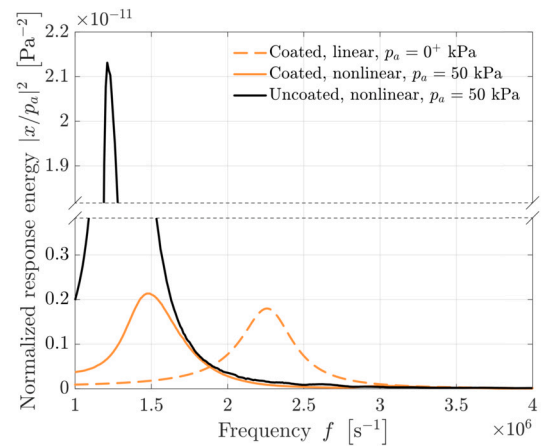


Fig. 5. Comparison of the theoretical frequency response of a coated microbubble (orange lines) and an uncoated microbubble (black line) with an equilibrium radius R_0 of $2.5 \mu\text{m}$. The normalized response energy $|x/p_a|^2$, where x is the normalized maximum amplitude $x = R_{\text{max}}/R_0 - 1$, is shown as a function of the forcing frequency f . The solid lines correspond to an acoustic driving $p_a = 50 \text{ kPa}$ and are obtained by solving the nonlinear Rayleigh–Plesset equation [Eq. (1)], while the dotted line is computed by linearizing Eq. (1) and thus corresponds to an acoustic driving $p_a = 0^+ \text{ kPa}$. The shell parameters used for the coated bubble are: $\kappa_s = 5 \times 10^{-9} \text{ kg s}^{-1}$, $E_s = 0.6 \text{ N m}^{-1}$, $\sigma_0 = 0 \text{ mN m}^{-1}$. The surface tension of the uncoated bubbles is $\sigma = 72.8 \text{ mN m}^{-1}$. The remaining physical parameters used are: $p_0 = 100 \text{ kPa}$, $c_1 = 1500 \text{ m s}^{-1}$, $\mu_1 = 0.002 \text{ Pa s}$, $\rho_1 = 1000 \text{ kg m}^{-3}$, $n = 1.07$.

ing Eq. (1). This behavior results from the elastic regime of the shell only being a brief transitional period between the prevailing buckling and rupture states of the shell at larger bubble oscillation excursions. Therefore, we would like to emphasize that using linearized models to simulate the bubble dynamics under the typical driving pressures found in clinical settings can lead to inaccurate results. Particularly, when determining the resonance frequency in clinical applications, if nonlinear models cannot be relied upon, it is recommended to disregard elasticity considerations and instead utilize the classical Minnaert formula for the natural frequency of uncoated bubbles:

$$f_{\text{res}} \approx \frac{1}{2\pi} \sqrt{\frac{3np_\infty}{\rho_1 R_0^2}}. \quad (9)$$

Considering the material properties of water under ambient conditions, this yields the widely recognized rule of thumb:

$$f_{\text{res}} R_0 \approx 3 \text{ MHz } \mu\text{m}. \quad (10)$$

4.2. Shell variability effects on microbubble response

Coated bubbles of identical size, in contrast to uncoated ones, exhibit a noticeable variability in the magnitude of their radial response to an ultrasound driving, as evidenced in Fig. 6 [122]. This variability gets accentuated for bubbles driven at their resonance frequency by the resonance amplification mechanism. The unpredictability observed in bubble dynamics can be attributed to variations in coating properties — the dilatational modulus and the dilatational viscosity — between individual bubbles, as illustrated with the shaded area in Fig. 6. The solid lines highlight, however, that the most significant factor influencing the bubble response at clinical-relevant acoustic driving is the shell dilatational viscosity. The range of values in the shell parameters found can be physically explained by the high degree of variation in the shell microstructure observed by Borden et al. [137] by leveraging fluorescence microscopy and scanning electron microscopy, as illustrated in Fig. 7.

Accurately assessing the dilatational modulus of a bubble shell, E_s , necessitates investigating the bubble’s behavior within its linear range, thereby preventing the occurrence of the buckling and rupture phases,

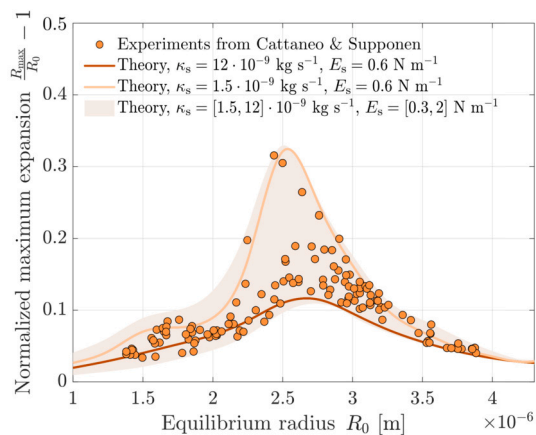


Fig. 6. Bubble-to-bubble variability in radial expansion due to shell properties. The normalized maximum radial expansion upon ultrasound driving (1.5 MHz, 40 kPa, 20 cycles) is shown as a function of the equilibrium bubble radius R_0 . The shaded area represents the envelope of maximum radial expansion simulated numerically with the model detailed in [122] using the range of shell modulus and viscosity values given in the legend. The solid lines depict the numerically computed maximum radial expansion for a low and high shell viscosity, respectively, and a fixed shell modulus (values given in the legend). Figure reproduced from the work by Cattaneo and Supponen [122] with permission from the Royal Society of Chemistry.

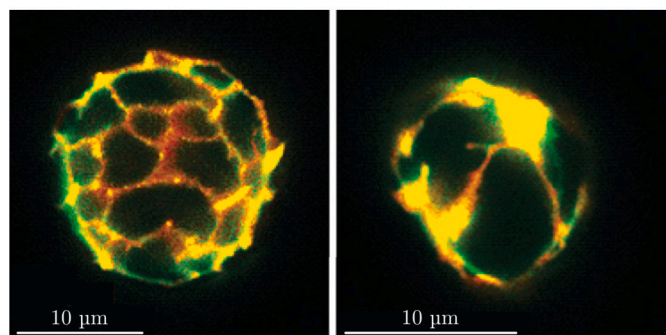


Fig. 7. Epifluorescent images of isolated microbubbles showing the heterogeneous lipid distribution on their surface. DSPC in black, DSPE-PEG in green, DilC₁₈ in red. Figure reproduced with permission from the work by Borden et al. [137]. © 2006 American Chemical Society.

which can artificially reduce the modulus magnitude. To achieve this objective, Daeichin et al. [138] employed a broadband photoacoustic wave generated by a nanosecond-pulsed laser illuminating an optical absorber to induce nanometric oscillations in individual microbubbles, which are then detected by light scattering of a continuous laser. The values of dilatational modulus, E_s , they measured, range from 0.4 N m^{-1} to 1.8 N m^{-1} . Such pronounced variations in the modulus can profoundly alter the resonance frequency of bubbles when operating within the linear regime, as depicted in Fig. 8 using the dashed lines. However, at the acoustic pressures normally used in clinical practice ($\geq 50 \text{ kPa}$), the same range of modulus values results in only small variations in the resonance frequencies and radial excursion of bubbles as illustrated by the solid lines in Fig. 8. In light of these results, it can be concluded that in clinical practice the linear shell regime, and reflexively, elasticity, play a secondary role and can be reasonably disregarded as a first approximation.

In order to accurately infer the shell dilatational viscosity from individual microbubble response upon ultrasound driving, Cattaneo and Supponen [122] employed ultra-high-speed microscopy imaging, optical trapping and wide-field fluorescence. The resulting shell viscosity, κ_s , values reveal an average of around $5 \times 10^{-9} \text{ kg s}^{-1}$ and a promi-

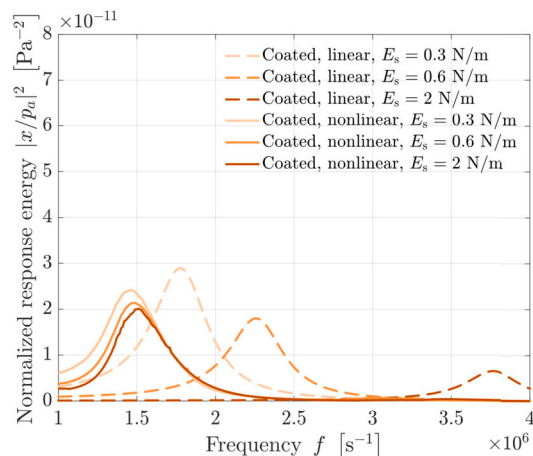


Fig. 8. Comparison of the frequency response of a coated microbubble with an equilibrium radius R_0 of $2.5 \mu\text{m}$ for different values of shell dilatational modulus E_s (values in the legend). The normalized response energy $|x/p_a|^2$, where x is the normalized maximum amplitude $x = R_{\text{max}}/R_0 - 1$, is shown as a function of the forcing frequency f . The solid lines correspond to an acoustic driving $p_a = 50 \text{ kPa}$ and are obtained by solving the nonlinear Rayleigh–Plesset equation (Eq. (1)), while the dotted line is computed by linearizing Eq. (1), and thus corresponds to an acoustic driving of $p_a = 0^+ \text{ kPa}$. The other shell parameters used are: $\kappa_s = 5 \times 10^{-9} \text{ kg s}^{-1}$, $\sigma_0 = 0 \text{ mN m}^{-1}$. The remaining physical parameters used are: $p_0 = 100 \text{ kPa}$, $c_1 = 1500 \text{ m s}^{-1}$, $\mu_1 = 0.002 \text{ Pa s}$, $\rho_1 = 1000 \text{ kg m}^{-3}$, $n = 1.07$.

nent variability of about an order of magnitude, ranging from around $1 \times 10^{-9} \text{ kg s}^{-1}$ to around $1 \times 10^{-8} \text{ kg s}^{-1}$. Moreover, they interestingly observed no correlation between shell viscosity and the bubble’s equilibrium radius, in contrast to most prior reports showing a significant increase in shell viscosity with the bubble’s equilibrium radius. This latter pattern has been deemed implausible, owing to the independence of a material property such as shell viscosity from the material quantity. This large range of shell viscosity values can severely alter the radial excursion of bubbles operated in the linear regime and even more pronouncedly for bubbles driven at clinically relevant acoustic pressures because of the nonlinear nature of the Rayleigh–Plesset equation, as shown in Fig. 9. The significant range of bubble excursions can lead to very diverse biophysical outcomes. Hence, it is crucial to advance techniques for producing microbubbles with greater shell homogeneity and consequently, better acoustic similarity.

It is important to note that the two above-mentioned studies measured the modulus and viscosity of the shell at room temperature. The modulus and viscosity of phospholipid monolayers have been shown to diminish as temperature increases [139]. Therefore, it is expected that they have smaller values at body temperature than the ones reported. In accordance with this notion, lipid-shelled microbubbles tested at body temperature have shown an increased radial expansion and an enhanced occurrence of phenomena such as jetting, shell fragmentation, and gas expulsion, with respect to the tests performed at room temperature [140].

Duncan and Needham [141] found that coated microbubbles remain stable in a saturated solution for multiple hours, which demonstrates that a lipid shell can eliminate the Laplace pressure and result in a neutralized surface tension, σ_0 , at the gas/water interface. Cattaneo and Supponen [122] came to the same conclusion by finding, through parametrical fitting, that only a null value of initial surface tension can encompass all data points reported in Fig. 6. However, low surface tension typically destabilizes lipid monolayers. Instead, the stability observed could suggest the presence of compression surface stresses of a rheological nature, which counteracts the small finite surface tension of a thermodynamic nature, resulting in an effective zero surface stress.

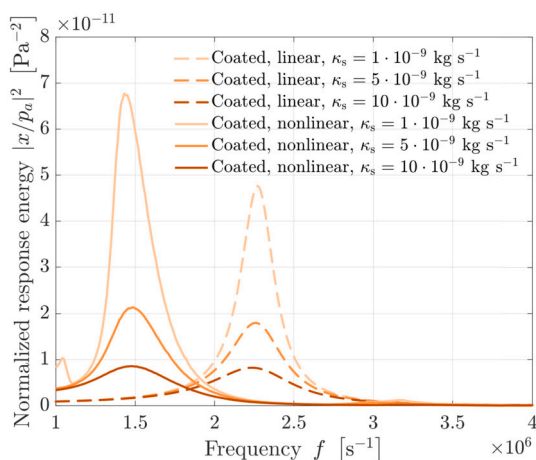


Fig. 9. Comparison of the frequency response of a coated microbubble with an equilibrium radius R_0 of $2.5 \mu\text{m}$ for different values of shell dilatational viscosity, κ_s (values in the legend). The normalized response energy, $|x/p_a|^2$, where x is the normalized maximum amplitude, $x = R_{\text{max}}/R_0 - 1$, is shown as a function of the forcing frequency, f . The solid lines correspond to an acoustic driving $p_a = 50 \text{ kPa}$ and are obtained by solving the nonlinear Rayleigh–Plesset equation [Eq. (1)], while the dotted line is computed by linearizing Eq. (1) and thus it corresponds to an acoustic driving $p_a = 0^+ \text{ kPa}$. The other shell parameters used are: $E_s = 0.6 \text{ N m}^{-1}$, $\sigma_0 = 0 \text{ m N m}^{-1}$. The remaining physical parameters used are: $p_0 = 100 \text{ kPa}$, $c_1 = 1500 \text{ m s}^{-1}$, $\mu_1 = 0.002 \text{ Pa s}$, $\rho_1 = 1000 \text{ kg m}^{-3}$, $n = 1.07$.

4.3. Confinement effects on microbubble response

In the context of drug delivery, it is essential to characterize the influence of blood vessel confinement on the response of microbubbles to ultrasound and, conversely, the biological effects of oscillating bubbles on the surrounding tissue. Oğuz and Prosperetti [142] computed the natural frequency of gas bubbles contained in a rigid-walled tube having a diameter comparable to the bubble's diameter using the boundary integral method. Their findings reveal that the bubble resonance frequency decreases up to one-third of the value for an unconstrained bubble. Qin and Ferrara [143,144] studied the interaction of an ultrasound-driven coated microbubble and a compliant microvessel by solving the axisymmetric, incompressible, viscid Navier–Stokes equations, coupled with a lumped-parameter model for describing the perivascular reactive radial stress, and the inertial effect of microvessels and surrounding tissue. Their numerical computations demonstrate that the natural frequency of a bubble significantly diminishes as the vessel diameter decreases, consistent with the observations made by Oğuz and Prosperetti [142], and increases as the vessel rigidity decreases. As the vessel or the adjacent tissue stiffens, both the oscillation of the microbubble and the expansion of the vessel diminish, while the circumferential stress is anticipated to rise. A peak negative pressure (PNP) of 0.5 MPa , when applied at a center frequency of 1 MHz , is expected to cause the circumferential stress surpassing the threshold required to cause the rupture of small compliant vascular vessels with a diameter less than $15 \mu\text{m}$. Caskey et al. [145] compared the observed radial expansion of microbubbles constrained within small vessels in a rat cecum with the predictions made by Qin and Ferrara's model finding a good agreement. Nonetheless, due to the significant diversity in the mechanical characteristics of living tissues and their substantial impact on microbubble behavior, achieving results consistent with experimental findings often relies on selecting model parameters in an ad-hoc manner.

4.4. Drug release from microbubble shell

Microbubbles can be loaded with drug molecules or drug-carrying vesicles, either by incorporating them within the lipid shell or by attaching them to it (see Sec. 2.3). Upon ultrasound driving, the bubble

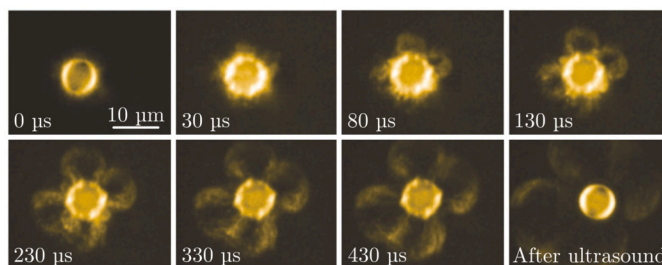


Fig. 10. Ultrasound-induced release of liposomes attached to the lipid shell of a microbubble, and their transport as a result of acoustic streaming. Figure reproduced with permission from the work by Versluis [147].

oscillation can cause the shell to rupture, releasing the drug payload into the surrounding tissue. For targeted delivery applications, precise regulation of the drug release from the microbubble surface into the designated target area is essential. In order to elucidate the dynamics of lipid shedding during ultrasound exposure, Luan et al. [146] employed high-speed fluorescence imaging and a lipophilic dye incorporated in the shell. Their findings revealed that shell shedding could initiate within just a few ultrasound pulses, and the existence of a critical threshold in the normalized radial excursion, equal to 0.3 , beyond which the shedding of lipids occurs. Finally, their observations showed that the transport of detached material is governed by the acoustic streaming flow induced by the bubble oscillation, which depends on the radial excursion of the microbubble and the length of the ultrasound pulse. A series of images showing the representative release of liposomes attached to the bubble shell is shown in Fig. 10

4.5. Microbubble stability under ultrasound

Coated microbubbles are delicate constructs that can withstand only a few microseconds of ultrasound exposure at the acoustic intensities normally employed in the clinical setting. Borden et al. [148] reported fast bubble dissolution at $p_a = 400 \text{ kPa}$ and bubble fragmentation from $p_a = 800 \text{ kPa}$. Fig. 11, reproduced from their study, shows a measurement of the change in radius of an initially over-resonant bubble as the number of acoustic cycles increases for $p_a = 400 \text{ kPa}$. The rate of dissolution increases as the bubble nears its resonance size, and drops for radii that are considerably distant from it. O'Brien et al. [149] showed that the cause for such a rapid bubble dissolution is in the shedding of the phospholipid shell, which decreases the concentration of surfactants at the interface and hence intensifies the gas diffusion, which would be negligible under short acoustic exposures and an intact shell. The model they developed accurately replicates the observed experimental behavior of bubble dissolution and hence, can be leveraged to predict the dissolution rate of microbubble agents at different acoustic pressures. Fig. 12 showcases the simulated evolution of a microbubble distribution after six repeated eight-cycle acoustic pulses at an incident frequency of 2.25 MHz . In conclusion, employing prolonged ultrasound bursts at elevated acoustic pressures in a clinical environment proves futile, as the bubbles can only endure a limited number of cycles under such conditions.

4.6. Mechanical Index (MI) as a parameter to predict microbubble-induced effects

In Sec. 4.1, we showed that bubble dynamics is predominantly governed by both frequency and driving pressure. Nonetheless, in diagnostics and therapy, having a single index to express the intensity of the bubbles response proves convenient. This led to the introduction of the mechanical index (MI), which serves as a measure to assess the probability of causing adverse biological effects through non-thermal mechanisms when pre-existing gas nuclei are exposed to diagnostic ultrasound. The MI is defined as the peak negative pressure, p_a (in MPa),

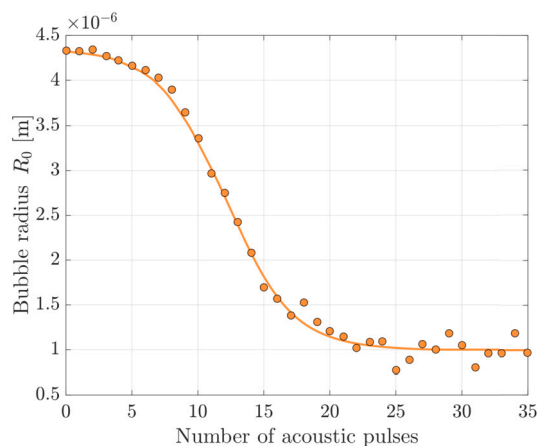


Fig. 11. Effect of repeated acoustic pulses on the stability of a microbubble. The evolution of the radius of a lipid-coated microbubble (DSPC:DSPE-PEG2000) undergoing repeated acoustic pulses (1-cycle, 2.25 MHz, 400 kPa) is shown as a function of the number of pulses. Experimental measurements in dots, sigmoid fit in solid line. Data kindly provided by Mark Borden.

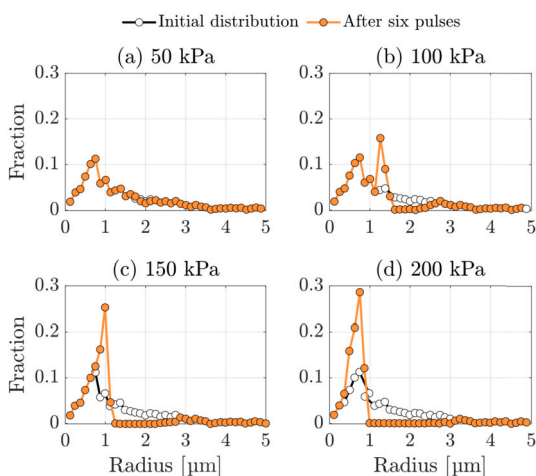


Fig. 12. Changes in the size distribution of lipid-coated microbubbles (SonoVue[®]) after six repeated eight-cycle acoustic pulses at an incident frequency of 2.25 MHz for different pressure amplitudes. Figure reproduced with permission from the work by O'Brien et al. [149].

divided by the square root of the frequency, f (in MHz), of the acoustic driving:

$$MI = \frac{p_a}{\sqrt{f}}. \quad (11)$$

Its form draws from an analytical solution presented by Apfel and Holland [150] to determine the minimum acoustic pressure amplitude needed to induce inertial cavitation in an uncoated air bubble. By setting the onset of inertial cavitation to occur when the temperature inside the bubble reaches 5000 K, they found that this threshold increases as frequency to the power 0.48 in water, and to the power 0.60 in blood. This leads to the formulation of Eq. (11). However, several aspects of the MI formulation, including the scaling exponent of the frequency variable, the pertinent physical variables, and the threshold criteria for inertial cavitation are still subject of ongoing debate. Church [151] conducted numerical simulations and demonstrated that, when dealing with blood as the medium, the frequency scaling factor is actually approximately one when employing the same threshold criterion as Apfel and Holland. Additionally, he highlighted that as the acoustic pulse duration increases, the threshold for inertial cavitation diminishes, thus raising questions about the inclusion of the number of

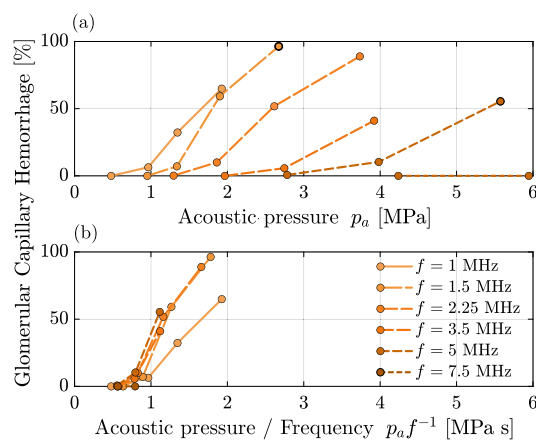


Fig. 13. (a) The percentage of glomerular capillary hemorrhage from histology as a function of the peak negative pressure amplitude for different ultrasound frequencies. (b) The percentage of glomerular capillary hemorrhage from histology as shown in (a), but replotted as a function of the ratio of peak negative pressure and frequency. Figure reproduced with permission from the work by Miller et al. [154].

acoustic cycles in the MI definition. Concerning the threshold criteria for inertial cavitation, Flynn [152] employed a dynamic comparison between the inertial and pressure components of the radial acceleration, demonstrating that this often approximates to $R_{\max} = 2R_0$. According to the study by Church [151], inertial cavitation occurs at around 0.2 MPa at 1 MHz frequency for a single-cycle pulse. This threshold can decrease to as low as 0.12 MPa when the pulse length is extended. Nevertheless, this value is significantly below the FDA's established maximum output limit of $MI = 1.9$, a somewhat arbitrary threshold determined based on the acoustic output of devices introduced to the market before 1976 and not supported by a scientific basis linked to potential adverse effects on patients [151]. On the other hand, it is important to consider that the pressure thresholds required to initiate inertial cavitation are higher than those estimated by Church. This is primarily due to real-world clinical scenarios where tissues absorb acoustic signals, bubbles are confined within narrow capillaries, and the bubbles themselves are actually coated, all of which collectively reduce the radial excursion of bubbles. It is therefore evident that there is a pressing need to create an index specifically tailored to gauge the biological impact of coated microbubbles within a clinically pertinent environment. In response to this demand, several studies recommend using a linear ratio between pressure and frequency as a suitable index. Stieger et al. [153] identified this relationship while investigating the extravasation of a fluorescent dye within a chorioallantoic membrane model, pinpointing an apparent threshold at around 0.6. Similarly, Miller et al. [154] observed this same index in the context of glomerular capillary hemorrhage, with a threshold of 0.5, as reported in Fig. 13. These findings find theoretical support in the simulations of Qin and Ferrara [143], who suggested that the frequency-dependent circumferential stress on a small compliant vessel correlates more closely with the linear ratio of PNP and frequency rather than with MI. Recognizing the limitations of the classical formulation of MI, researchers have introduced various alternative metrics to quantify cavitation activity, often referred to as “cavitation dose”, by leveraging real-time acoustic measurements [155–160]. One of the most recognized indicators is the emission of a broadband noise continuum, attributed to the extremely erratic oscillations of bubbles under high-pressure acoustic driving [136]. However, as of now, there is no universal metric for calculating the cavitation dose from acoustic data. Developing a detector-independent methodology for this purpose would enable cross-setup comparisons and streamline safety and efficacy studies.

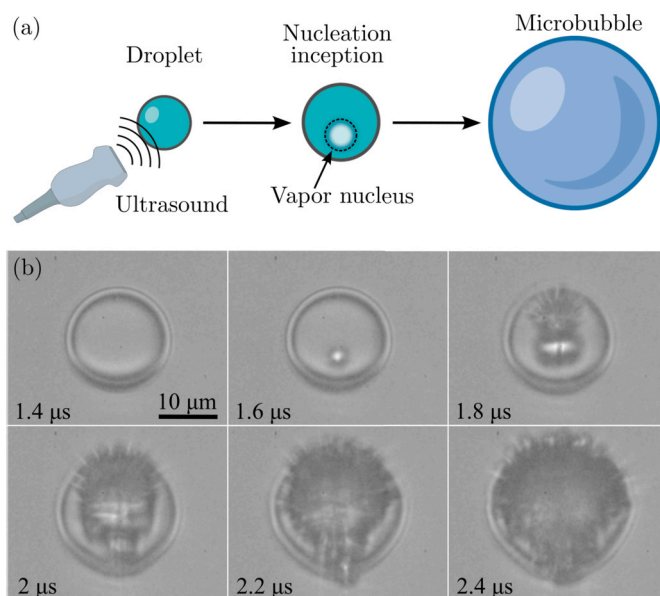


Fig. 14. (a) Schematic illustrating the acoustic droplet vaporization process - Upon exposure to ultrasound, a vapor nucleus is generated within the droplet, which then expands into a microbubble. (b) Snapshots of single-droplet vaporization captured at a frame rate of 10 MHz [169]. The ultrasound reaches the droplet at $t = 0$. The droplet here has an initial radius of $R_0 \approx 9 \mu\text{m}$ and is maintained at $T_\infty = 40 \text{ }^\circ\text{C}$ (superheated by $11 \text{ }^\circ\text{C}$). The applied peak negative pressure is $p_a \approx 4.5 \text{ MPa}$ at a frequency of $f = 5 \text{ MHz}$.

4.7. Acoustic vaporization of phase-change agents

Acoustic vaporization of a droplet arises due to its interaction with an incoming sound wave of suitable acoustic properties. The acoustic wave, transmitted in the droplet bulk, can create low-pressure regions that favor vapor bubble nucleation. Most of the PFCs typically used as phase-change agents are superheated at body temperature, meaning that their boiling temperature is lower than $37 \text{ }^\circ\text{C}$. In this case, once nucleation occurs and the first vapor nuclei reach their critical size, they will continue to grow until vaporization is complete, as shown in Fig. 14. Stable vaporization has also been reported for heavier PFCs such as PFH, perfluorooctane (PFO), and perfluorooctyl bromide (PFOB), which have higher boiling temperatures than the human body temperature, with the possibility to induce recondensation in subsequent sonication cycles [161,162]. It should be noted that, despite the optimal size for phase-change drug delivery agents lying within the sub-micrometric range, the larger part of the studies involving optical visualization of the initial vaporization dynamics employs micrometer-sized droplets. This choice comes directly from the spatial resolution limitation of visible light microscopes, which is in the order of hundreds of nanometers.

Most of the theoretical models attempting to explain vapor nucleation inception in droplets make use of Classical Nucleation Theory (CNT), either in its classical form or modified in order to include the effects of Laplace pressure and reaching of the Spinodal Stability Limit [163,164]. These models can be used to obtain a threshold negative acoustic pressure below which vaporization is expected. A typical assumption, which is supported by studies employing ultra-high-speed microscopy observing single droplet vaporization, is that the first vapor nucleus is formed in the droplet bulk due to homogeneous nucleation [165–168]. For more complex agents, in which multiple phases are present [162], heterogeneous nucleation could also occur, possibly at lower negative acoustic pressures.

Vaporization of a droplet has been reported to happen abruptly when a certain PNP of the acoustic wave is reached. This pressure value is usually referred to as the vaporization threshold (or ADV threshold),

and is an important performance parameter for phase-change emulsions, as it is directly related to the safety and specificity of the agent. A few selected studies of the measured threshold values and the increasing trend of the threshold concerning relevant experimental parameters are summarized in Table 1. It can be noticed from Table 1 that even in the small sample of experiments reported here, the parameters that are maintained or varied are quite different, which makes it difficult to quantify the dependence of the required threshold on the relevant parameters. More comprehensive comparisons can be found in Wu et al. [170], Lea-Banks et al. [47], and Aliabouzar et al. [171].

The ADV threshold has been shown to decrease by increasing the droplet size [167,172], pulse length [88,173], droplet concentration [170], and ambient temperature (thereby modifying the degree of superheat for the droplet core) [70]. It has been shown by Wu et al. [170] that an increase in the pulse duration slightly reduces the vaporization threshold of superheated PFB nanodroplets, while for PFP nanodroplets this is the case only if they are kept below their boiling temperature [76,170]. Using a lighter PFC for the liquid core also decreases the required threshold [161,173], but at the cost of decreased thermodynamic stability. The dependence of the ADV threshold on the applied frequency is an interesting discussion. For droplets below a certain size (usually $< 3 \mu\text{m}$), it has been shown that the threshold could both increase [171,172] or decrease [76] with increasing frequency, while for larger droplets, the threshold decreases with increasing frequency [167]. Therefore, understanding the physics of the interaction between the acoustic wave and the droplet is required to explain all the behaviors mentioned above, with the final goal being to reduce the required acoustic threshold to clinically relevant values.

It has been hypothesized that the acoustic wave interacts with the droplet through two different mechanisms:

- Superharmonic focusing:** Shpak et al. [167] assumed that the propagation of the ultrasound wave inside the droplet bulk follows the linear wave equation, but a distortion of the fundamental wave can arise during the travel from the ultrasound source to the target droplet. This distortion process, due to nonlinear propagation, manifests itself with the creation of superharmonics that are integer multiples of the fundamental frequency. The droplet then acts as an acoustic lens, focusing all the superharmonics in its bulk, and creating a localized and amplified negative pressure region in which nucleation is most likely to occur. Their results show an incoming PNP amplification of up to 9 times in the droplet bulk, reported for $10\text{-}\mu\text{m}$ -radius droplets sonicated with an ultrasound wave having a fundamental frequency of 6.5 MHz (see Fig. 15). The intricate interplay between droplet size and sonicating harmonic content creates a non-trivial trend for the pressure amplification factor that generally increases with applied fundamental frequency and the droplet radius, as depicted in Fig. 15. Shpak et al. [167] also show that for an ultrasound wave with a central frequency of 5 MHz , the focusing effect is absent for sub-micron droplets. The need for high-frequency excitation in order to trigger superharmonic focusing poses some limitations for the *in-vivo* exploitation of this phenomenon due to the higher absorption of acoustic waves in living tissue and the lower amount of distortion that takes place in it [174].
- Acoustic resonance:** Lajoinie et al. [90] proposed resonance as an alternative mechanism for droplet vaporization, yielding a three-fold amplification of the incoming acoustic wave in the center of the droplet bulk, provided the correct fundamental acoustic frequency is used. The typical resonance frequency for a $2.7\text{-}\mu\text{m}$ -radius droplet is reported to be around 45 MHz . Using surface acoustic wave (SAW) devices, they generated a purely sinusoidal excitation with minimal superharmonic content to vaporize droplets roughly $2\text{-}6 \mu\text{m}$ in radius. The experimental results obtained through ultra-high-speed microscopy matched well with their theoretical models and numerical predictions.

Table 1
ADV threshold values and their variation concerning relevant experimental parameters reported in selected studies.

Reference	Core	Temperature (°C)	Size (μm)	Frequency (MHz)	Threshold (MPa)	Threshold increases with ...
Aliabouzar et al. [161]	PFP	37	10-25	2.3-15	0.4-1.1	Increasing frequency
	PFH	37	10-28	2.3-15	2.3-1.1	Decreasing frequency
Williams et al. [76]	PFP	37	0.22	5-15	5.9-3.7	Decreasing frequency
Fabiilli et al. [172]	PFP	37	1.2-4.8	3.5	4.2-2.3	Decreasing size
	PFP	25-65	2.1	3.5	4.1-2.6	Decreasing degree of superheat
	PFH	44-65	2.2	3.5	4.6-2.8	Decreasing degree of superheat

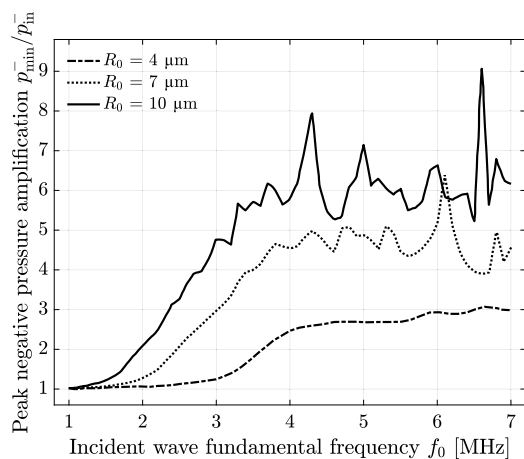


Fig. 15. The pressure amplification factor predicted by superharmonic focusing as a function of the applied fundamental frequency for three different droplet radii. Figure reproduced with permission from the work by Shpak et al. [167].

However, the two theories presented above apply to very different regimes, with superharmonic focusing relying on relatively low fundamental frequencies and on a large number of harmonics interacting with the droplet, while the resonance theory relies on monochromatic, high-frequency sound waves. The differences and common grounds of these two models are yet to be clarified, and the transition regime in between remains to be explored. A recent review by Aliabouzar et al. [69] summarizes the different theories, models, and experiments on ADV more comprehensively.

It should be noted that the recently proposed updated version of the CNT for ADV demonstrates that thermodynamic metastability is lost if the spinodal pressure is reached during sonication [164]. For PFP droplets at physiological temperature, this negative pressure value is around 5 MPa, much lower (in absolute value) than the PNP inside the droplet bulk predicted in other works [167,175]. Therefore, from the above predicted pressures, one would expect nucleation to occur throughout the bulk of the droplet as expected from the threshold predictions from Qin et al. [164]. In contrast, the experimental nucleation maps in Shpak et al. [167] show a very localized nucleation area in some cases. This mismatch suggests that either the pressure values predicted are not accurate, or the modified nucleation theory needs to be further improved.

The ADV thresholds *in vivo* can significantly differ from *in-vitro* conditions. The higher absorption of acoustic waves passing through tissues implies that the sonication pressures required *in vivo* are much higher [90,176], and typical waveforms used *in vitro* need to be severely modified to prevent excess heating of tissues [177]. Changed flow conditions *in-vivo* also affect the ADV threshold. While the flow velocity and the hydrostatic pressure have been shown to have no effect on the ADV threshold [176,178], the required threshold increases with the viscosity of the liquid [172,176,178]. Furthermore, it has been shown that the required PNP also increases with the degree of drop confinement, either due to acoustic scattering effects [179], or the additional damp-

ening, from the boundaries, that reduces the vapor embryo nucleation rate within the droplets [176].

Currently, the PNP required to achieve ADV *in vivo* are dangerously high [49,180], and therefore, several techniques have been proposed to reduce this threshold. A valid alternative to classic formulations is producing phase-change Pickering emulsions [73], or more sophisticated dispersed phases, including structures such as hydrocarbon endoskeletons [181], to produce droplets that promote vapor bubble nucleation on the droplet-water interface or in the bulk. Generating and vaporizing droplet aggregates has also been highlighted as a potential technique for reducing the required acoustic pressure [182,183]. Optimization of the incoming acoustic waves could be a viable way to reduce the pressure amplitude needed. For example, employing dual-frequency transducers has effectively reduced the acoustic power needed for droplet vaporization [184,185]. Designing the sonicating wave shape in order to maximize the focusing or the resonance effect presented by Shpak et al. [167] or Lajoinie et al. [90] is another way to initiate ADV at lower acoustic pressures. Acoustic cluster therapy (ACT), where microdroplets are tagged together with microbubbles, has also been explored to initiate the droplet phase conversion at lower MI values [186]. However, increasing the pulse length, total sonication time, or droplet size, are not really viable ways to reduce the required acoustic pressure because of the increased amount of thermal absorption and size constraints *in vivo*.

4.8. Dynamics of vaporized droplets

Once the first vapor nucleus is formed, the physical system consists of a bubble confined in the liquid bulk of the droplet, immersed in a continuous liquid phase (see Fig. 14(a) and snapshot at 1.6 μs in Fig. 14(b)). The acoustic excitation that has initiated the first nucleation event can either still be active, thus actively driving the newly born bubble, or already worn out. In the latter case, the bubble evolves without external driving, following the most energetically favorable path. If the droplet is in a superheated state, the gain in free energy due to the phase change is enough to supplement the bubble growth until the liquid phase available is fully converted. This behavior has been observed by Shpak et al. [89] for superheated PFP microdroplets. On the other hand, another work by Reznik et al. reported the collapse and disappearance of newly vaporized superheated PFP nanodroplet [70]. The difference in the behavior could be attributed to the different initial sizes of the observed droplet. If the ultrasound excitation is still on after bubble nucleation, an enhancement in the bubble radius growth rate has been observed with respect to the free expansion for a superheated PFP microdroplet [166]. This is believed to be caused by rectified diffusion, which improves the net heat transfer towards the bubble-liquid interface supplying the needed latent energy for phase change [166]. It has been shown that in this case, non-condensable gases diffuse in the vapor bubble and prevent recondensation during the collapse induced by ultrasound driving.

In the case of an initially subcooled droplet liquid core, as is the case for fluorocarbons heavier than PFP at body temperature, a reversion to the liquid phase would be expected due to the thermodynamic instability of the vapor phase. Recondensation of PFH nanodroplet [187] as well as PFO microdroplet [162] after acoustic vaporization has been

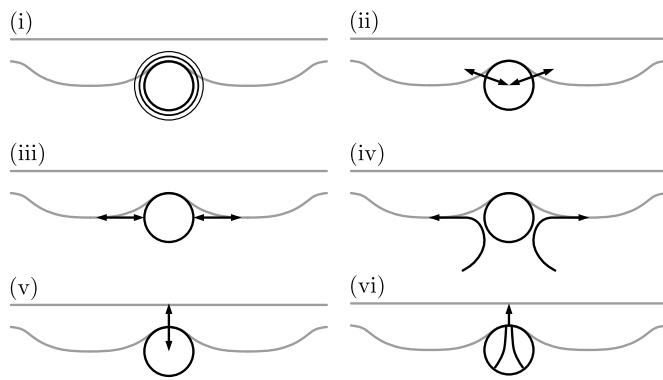


Fig. 16. Various forms of mechanical action exerted by a microbubble on a substrate: (i) pulsating pressure field; (ii) impact and suction pressure; (iii) alternate shear stress; (iv) streaming shear stress; (v) radiation pressure; (vi) jet impact pressure. The ultrasound travels from the bottom to the top.

reported and confirm this hypothesis. On the other hand, Aliabouzar et al. [162] report the formation of metastable microbubbles following PFH microdroplet vaporization. The causes of the different behavior of PFH droplets are not clear, but it is hypothesized that diffusion of non-condensable gas in the vapor core could play a role in stabilizing the gaseous phase, preventing the full disappearance of the nucleated bubble. Further investigations are needed to clarify these important aspects.

Several authors have proposed models to describe ADV dynamics by taking into account different parameters, such as driving pressure, applied fundamental frequency, and shell mechanical properties [188–190], with assumptions including spherical symmetry, initial conditions of the vapor nucleus, and selected properties of the droplet-encapsulating shell. Numerical simulation can be a powerful tool to study droplet vaporization dynamics due to the inherent difficulty in the experimental observation of this phenomenon. However, experimental validation is still required to confirm the feasibility of the base hypothesis.

5. Agent-cell interaction

Upon ultrasound exposure, microbubbles and droplets exert a mechanical action on the surrounding cell/tissues which eventually enhance their permeability to drugs. Despite the significant progress made in recent studies, achieving a comprehensive mechanistic understanding of the entire process remains a formidable challenge owing to the wide range of spatial and temporal scales involved (ranging from nanosecond- and nanometer-resolution for the dynamics of agents to minute- and centimeter-resolution for the drug transport), the intricacy of biological responses and the challenges associated with directly observing this phenomenon. In this section, we summarize the progress made in understanding the sources of stresses induced by the agents, the consequent biological response, and the resulting enhancement in drug permeability. In addition, the current *in-vitro* models used to investigate the agent-cell interaction are reviewed and their mechanical properties are compared to those found for actual living tissues.

5.1. Mechanical action of bubbles near a substrate

Microbubbles driven by ultrasound exert mechanical action on adjacent tissue in different ways as depicted in Fig. 16: (i) the bubble oscillation creates a pulsating pressure field; (ii) the bubble interface motion generates an impact force; (iii) the bubble oscillation produces pulsating shear stresses; (iv) the acoustic streaming induced by bubble oscillation generates continuous shear stresses; (v) the ultrasound driving imparts a translational force on bubbles; and (vi) the asymmetric bubble oscillation can produce liquid microjets.

The magnitude of each stress mechanism is estimated as follows.

Oscillation pressure The acoustic pressure radiated by a bubble that is oscillating spherically, evaluated at the bubble interface, can be expressed as:

$$p_{\text{oscillation}}(t) = p(R) - P_F = \rho_1 \left(R\ddot{R} + \frac{3}{2}\dot{R}^2 \right), \quad (12)$$

which is derived from Eq. (1) and Eq. (2) with the viscosity contribution disregarded due to its minimal influence. The radiated pressure should not be mistaken for the pressure resulting from the fluid flow impacting against a wall. In fact, when the bubble expands, the radiated pressure is negative, in contrast to the positive pressure generated by the fluid flow arresting against a wall.

Impact pressure The impact or suction pressure on a wall resulting from the expansion or contraction of a bubble respectively, can be estimated by examining the momentum balance of a liquid stream, considered stationary for simplicity, as it impinges or moves away from the wall with a speed \dot{R} :

$$p_{\text{impact}}(t) \approx \rho_1 |\dot{R}| \dot{R}, \quad (13)$$

Oscillation shear stress The tangential wall stress resulting from the oscillatory flow of the bubble can be approximated under the assumption of laminar flow, as governed by the quotient of the bubble wall velocity and the boundary layer thickness, δ , as follows [191]:

$$\tau_{\text{oscillation}}(t) \approx \mu_1 \dot{R} / \delta, \quad (14)$$

where δ can be determined as $\delta = (2\mu_1/\rho_1\omega)^{1/2}$, with $\omega = 2\pi f$ being the angular forcing frequency.

Acoustic streaming shear stress Acoustic streaming is a second-order steady flow that emerges from an oscillatory primary flow. It is driven by the dissipation of the acoustic energy flux, which allows for the creation of gradients in the momentum flux. The classical treatment of acoustic streaming, pioneered by Rayleigh [192], Nyborg [193], and Westervelt [194], and therefore called NWR streaming, ignored the effect of the fluid's inertia on the streaming motion. The NWR streaming wall stress induced by a bubble oscillating near the wall can be approximated as:

$$\tau_{\text{streaming}} \approx \mu_1 x^2 R_0 \omega / \delta, \quad (15)$$

where x is the normalized maximum amplitude, $x = R_{\text{max}}/R_0 - 1$. However, this result is accurate only for very slow flows (creeping motion regime) for which the Reynolds number of the streaming motion, $\text{Re} = \rho_1 U_s R_0 / \mu_1$, is much smaller than 1, where U_s is the characteristic speed of the streaming flow. Therefore, the use of the NWR acoustic streaming theory, and consequently Eq. (15), is appropriate only for low acoustic driving pressures (up to around 10 kPa). For fast flows (Stuart streaming [195]), the streaming velocity should be calculated from the full steady Navier-Stokes equation. Utilizing the NWR streaming theory for such scenarios can lead to a significant overestimation, sometimes by orders of magnitude.

Acoustic radiation pressure Acoustic radiation force is the force exerted on objects when subjected to an acoustic driving pressure $p_d(t)$. In the context of bubbles, this phenomenon is referred to as the primary Bjerknes force [196]. The average pressure acting on the bubble reads:

$$p_{\text{radiation}} = 4R\dot{p}_d/3c_1, \quad (16)$$

Jet impact pressure The non-spherical oscillation of a bubble near a substrate can induce liquid microjets. The pressure generated at the point of impact on living tissue can be estimated using the water hammer pressure formula for flow with speed U_{jet} impinging on a substrate with properties similar to water [197,198]:

$$p_{\text{jet}} = \rho_1 c_1 U_{\text{jet}} / 2. \quad (17)$$

It has been a common belief that jetting exclusively takes place within the inertial cavitation regime, under very intense ultrasound pressures, in the order of the MPa [199]. Nevertheless, Cattaneo et al. [200] have revealed that jetting can manifest itself at substantially lower pressures, in the order of hundred kilopascals, and, even more interestingly, it occurs repeatedly and stably for multiple acoustic cycles. The frequency of occurrence can either be harmonic or half-harmonic, contingent upon the driving mechanism of the jet.

Comparison of mechanical stresses In order to gain a clearer understanding of the relative significance of the above-listed mechanisms, the evolution of their respective magnitudes over time is computed. Fig. 17 visually represents this evolution for an acoustic frequency of 1.5 MHz and two pressures, 5 kPa and 150 kPa, driving a bubble with a radius, R_0 of 3 μm . To maintain simplicity, the influence of the substrate on the bubble dynamics is disregarded. It is evident that the stress levels proportionally intensify as the driving pressure increases. Additionally, at 150 kPa for a driving frequency of 1.5 MHz, Cattaneo et al. [200] reported the occurrence of repeated jets with a speed, U_{jet} , of approximately 50 m s^{-1} . At this level of acoustic excitation, the NWR streaming theory (Eq. (15)) tends to overestimate the acoustic streaming stress. This leads to stresses that are roughly equivalent in magnitude to the oscillation stresses, despite the latter being expected to be of much higher order. The qualitative comparison in Fig. 17 suggests that the most significant mechanical stresses result from jetting, albeit for a brief duration. The stresses arising from the primary oscillatory motion of the fluid rank second in magnitude, while those induced by secondary acoustic effects are the least significant. Nonetheless, this does not necessarily imply that they lack the potential to exert a relevant effect on biological tissue, as shown in the next section. Additionally, depending on the unique characteristics of the substrate's morphology, the magnitude of these stresses can exhibit significant variations.

5.2. Cellular mechanical permeabilization via microbubbles

The effects of the microbubble-induced stresses on cellular barriers have been explored in numerous *in-vitro* cell monolayer studies, encompassing a diverse range of cell lines, including both cancer and primary endothelial cells. The endothelial layer stands as the primary biological barrier for microbubbles, preventing their escape from the bloodstream and making it the immediate cellular target they affect. van Wamel et al. [201] were the first to unveil, through ultra-high-speed microscopy, that the mechanical stresses generated by the oscillation of microbubbles in contact with endothelial cells result in the perforation of the cell membrane, a phenomenon known as sonoporation. Once these pores are formed, they provide an unobstructed pathway for the drug to reach the cellular cytoplasm directly. However, cell monolayers provide only a limited glimpse into the intricate dynamics of microbubbles interacting with the vasculature wall. The first direct optical observations of microbubbles interacting with a capillary bed were provided by Caskey et al. [145], who revealed that microbubbles confined within small vessels in an *ex-vivo* rat recum have the capability to stretch capillary walls by a few micrometers during their expansion and contraction phases. This significantly impacts the vascular integrity, causing the mechanical opening of interendothelial junctions, including the notoriously tight ones present in the blood-brain barrier [202]. The consequent formation of interendothelial gaps creates an efficient pathway for the delivery of therapeutic agents into extravascular tissues. Recently, Bezer et al. [203] investigated the microbubble behavior in microvessels under therapeutic ultrasound pulses using acute brain slices acquired from juvenile rats. They found that, in addition to vessel wall oscillations at microsecond timescales, significant tissue displacements occurred over millisecond timescales. Interestingly, microbubbles were also observed to extravasate by passing through microvessel walls, penetrating large

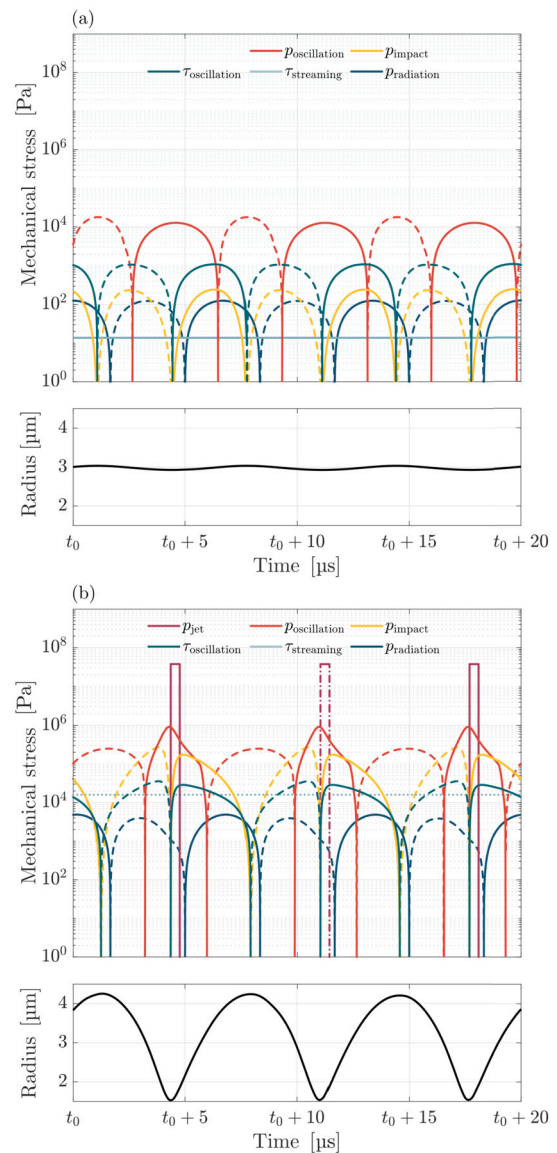


Fig. 17. Time evolution of the magnitude of different mechanical stresses exerted on a substrate by a microbubble with a radius of 3 μm driven with a frequency of 1.5 MHz and a pressure of 5 kPa in (a) and 150 kPa in (b). The solid lines depict stresses directed outward from the bubble, whereas the dashed lines represent stresses directed inward. The stresses are computed using Eqs. (12), (13), (14), (15), (16), (17). In (b), the jet pressure shown in the dash-dotted line occurs only when the jetting is harmonic rather than half-harmonic (see Cattaneo et al. [200] for further information). In (b), the acoustic streaming stress is depicted with a dotted line to emphasize that the NWR streaming theory [Eq. (15)] overestimates the stress at this acoustic intensity. The bubble's radial dynamics, presented in the bottom plots, is calculated by solving the nonlinear Rayleigh–Plesset equation [Eq. (1)], with the influence of the substrate on the bubble dynamics being disregarded. The shell parameters used for the simulations are: $\kappa_s = 5 \times 10^{-9} \text{ kg s}^{-1}$, $E_s = 0.6 \text{ N m}^{-1}$, $\sigma_0 = 0 \text{ mN m}^{-1}$. The remaining physical parameters used are: $p_0 = 100 \text{ kPa}$, $c_1 = 1500 \text{ m s}^{-1}$, $\mu_1 = 0.001 \text{ Pa s}$ (the value is doubled in bubble dynamics simulations to incorporate thermal damping effects), $\rho_1 = 1000 \text{ kg m}^{-3}$, $n = 1.07$.

distances into brain tissue after leaving the vessel. The likelihood of bubble extravasation increased with higher mechanical indices. At MI values considered safe (0.2–0.4), bubble extravasation was rare, but it became dominant at higher MIs (from 0.8). Microbubble extravasation may be a potential mechanism of tissue damage, including localized red blood cell extravasation, which has been observed in animals exposed to BBB opening treatments at high MI.

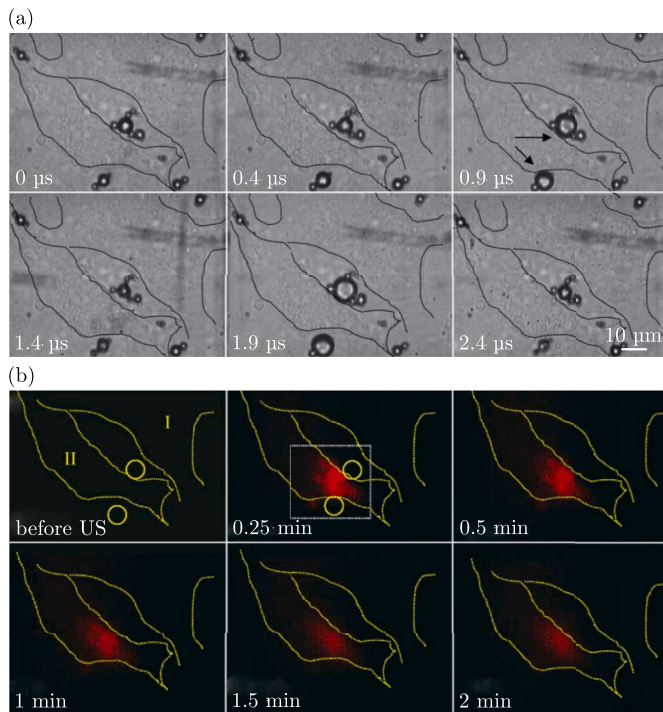


Fig. 18. (a) Response of ultrasound-driven microbubbles sitting in the intracellular space between two endothelial cells. The PNP is 0.4 MPa and the driving frequency is 1 MHz. (b) Fluorescent images of propidium iodide uptake of the cells shown in (a). Figure reproduced with permission from the work by van Wamel et al. [201].

Mechanisms of cellular permeabilization Various mechanisms have been proposed as potential promoters of cellular permeabilization. In the study of van Wamel et al. [201], the formation of pores through the cellular membrane was linked to the bubble interface repeatedly striking the cells. However, the specific placement of the bubbles, sitting adjacent to the cells instead of on top of the cell layer, particularly promoted this mechanism, as shown in Fig. 18. Helfield et al. [204] instead found the oscillatory shear stress induced by the bubble oscillations to be the key mechanism of sonoporation. Marmottant and Hilgenfeldt [205] have also suggested microstreaming, generated by the oscillation of bubbles driven at acoustic pressures in the order of a few tens of kilopascals, as a mechanism capable of rupturing lipid vesicles. However, we contend that this rupturing mechanism can be more accurately attributed to the impact pressure of the bubble, as the vesicle only ruptures upon contact with the bubble. Zhou et al. [206] illustrated the capability of the acoustic radiation force in pressing the bubble against the cell membrane, resulting in a progressive indentation of the membrane, which yields its eventual disruption. Furthermore, Prentice et al. [199] found an unsurprisingly significant disruption of the cell membrane when exposed to inertial jetting of microbubbles driven at acoustic pressures in the order of MPa. Finally, the stable repeated jetting observed by Cattaneo et al. [200] for pressure amplitudes in the range of a few hundred kPa, raises the intriguing prospect of localized cellular permeabilization through microjets within the stable cavitation regime. In conclusion, a clear consensus on the primary mechanism underlying sonoporation has yet to be established.

On the contrary, the mechanism behind the mechanical opening of interendothelial junctions is relatively simpler to understand. Chen et al. [207–209] showed for an *ex-vivo* rat mesenteric microvessel that the impact and suction pressure exerted by oscillating microbubbles driven at acoustic pressure in the order of several megapascals leads to the distension and invagination of the capillary wall, respectively, as shown in Fig. 19. The markedly larger invagination of the vessels, compared

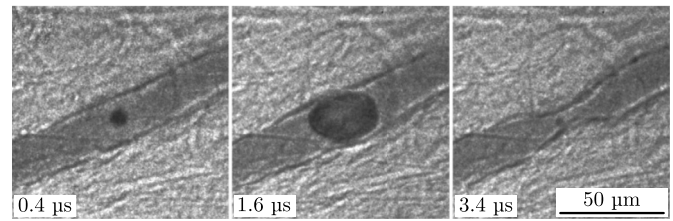


Fig. 19. Interaction between a microbubble and a capillary wall. The bubble distends and contracts the vessel. The invagination appears markedly larger than the distension. The PNP is 1.5 MPa and the driving frequency is 1 MHz. The vessel diameter is 22 μm . Figure reproduced with permission from the work by Chen et al. [207].

to distention, is likely due to the higher suction pressure as opposed to the impact pressure, as indicated in Fig. 17.

Acoustic parameters for cellular permeabilization The frequency, amplitude, and duration of the acoustic driving are the fundamental parameters governing the occurrence of sonoporation. In terms of the driving frequency, it is advisable to align with the resonance frequency of the microbubbles being used, as this minimizes the acoustic pressure needed to produce equivalent biological effects. Regarding the driving pressure, Kooiman et al. [210] and De Cock et al. [211] have revealed that for a driving frequency of 1 MHz, the perforation of the cell membrane occurs starting from an acoustic pressure of around 100 kPa. Furthermore, Kooiman et al. [210] found that regardless of the acoustic pressure applied, the uptake of propidium iodide (PI), a cell impermeable dye commonly used for evaluating cell membrane damage, occurred when the relative oscillation amplitude of microbubbles exceeded 0.5. Fan et al. [212] found a similar threshold pressure for sonoporation (around 170 kPa) for a driving frequency of 1.25 MHz. Helfield et al. [204], in contrast, identified the magnitude of oscillatory shear stress as an indicator for sonoporation. They noted that the shear stress threshold for inducing sonoporation is on the order of kilopascals, and it interestingly exhibits an inverse square-root relationship with the number of oscillation cycles, and an approximately linear dependence on ultrasound frequency from 0.5 to 2 MHz. About the driving duration, Fan et al. [212], as well as Helfield et al. [204], successfully achieved sonoporation with acoustic signals lasting less than 10 μs . Kooiman et al. [210] applied six pulses, each lasting 10 μs . De Cock et al. [211], on the other hand, utilized multiple pulses lasting 2 ms. We can deduce from these single-cell experiments that membrane perforation predominantly takes place within tens of microseconds. This conclusion is supported by another study by Fan et al. [213], which explicitly demonstrated that short ultrasound pulses lasting only a few tens of microseconds, with high pressure levels in the range of a few hundred kilopascals, yield the most favorable results in terms of intracellular delivery efficiency and cell viability. In contrast to the kinetics of membrane perforation, there is a lack of understanding of the relationship between acoustic parameters and the kinetics of the mechanical opening of interendothelial junctions because of the absence of adequate technology to correlate the microbubble dynamics with the biological response within a real vascular system.

Effect of bubble-cell distance on cellular permeabilization Ward et al. [214] were the first to recognize that the effectiveness of sonoporation is dependent on the distance between bubbles and target cells, revealing that the effectiveness diminishes rapidly with increasing spacing. Zhou et al. [206] demonstrated that membrane poration is maximized when the bubbles make direct contact with the membrane, and diminish rapidly as the distance between the bubbles and the cells increases, halving at a distance equal to the size of the bubbles and completely disappearing at a distance of three times the size of the bubbles, as there was no contact with the cell membrane even during the expansion

phase of the bubble. Qin et al. [215] also reported similar findings, although noting the absence of sonoporation for a bubble-to-cell distance exceeding the size of the bubbles, likely due to the acoustic driving pressure being lower than that reported in prior studies. We can conclude that the creation of pores in the cell membrane takes place upon physical impact by the bubble, and the highest efficacy in this process is attained when the bubble is continuously in direct contact with the membrane. One effective approach for positioning bubbles near cells involves the use of acoustic radiation force. In their study, Shortencarier et al. [216] employed a prolonged low-pressure acoustic pulse to guide gas-filled lipospheres toward the vessel wall, and subsequently used a brief, high-pressure pulse lasting only a few microseconds to fragment the agents. Another method is to employ functionalized microbubbles to target specific receptor molecules in the endothelium, ensuring direct contact with it [210] (see Sec. 2.3).

Effect of acoustic pressure on permeabilization extent The size of pores on the cellular membrane dictates the dimensions of therapeutics that can be passively internalized into the cell cytoplasm. Transmission electron microscopy (TEM) and atomic force microscopy (AFM) have been extensively employed to measure the dimensions of pores. In their study, Yang et al. [217] observed that pore sizes are closely related to the applied driving pressure. They estimated the pore size on breast cancer cells following long acoustic exposures at various pressures, yielding estimates of approximately 1 nm to 90 nm at 0.19 MPa, 10 nm to 500 nm at 0.25 MPa, 0.8 μm to 1.1 μm at 0.38 MPa and 2.0 μm to 4.3 μm at 0.48 MPa. Qiu et al. [218] observed a comparable trend in pore sizes for cells of the same type, although the absolute sizes were smaller and remained below 1 μm at 3 MPa. For a brief, 3 μs -long acoustic exposure at 1.1 MPa of peak negative pressure, Kudo et al. [219] identified pores of around 1 μm on endothelial cells. Conversely, Prentice et al. [199] for the same frequency but for 1.4 MPa of pressure and 20 μs of exposure observed pores of 16 μm of diameter. TEM and AFM are powerful techniques but are limited to post-exposure assessment of samples. As a consequence, tiny pores may have already closed by the time sample preparation concludes. Zhou et al. [220] estimated the size of the pores by measuring the maximal transmembrane current (TMC) change via the patch-clamp technique. They observed a size diameter of approximately 110 nm in response to a prolonged acoustic pulse with an intensity of 0.3 MPa. Fan et al. [212] used the same TMC technique and identified pores of around 15 nm in diameter for a microsecond-long exposure at 0.12 MPa. Hu et al. [221], on the other hand, leveraged real-time confocal microscopy to directly visualize the cell membrane damage. They observed that microbubbles driven at 0.85 MPa for 10 μs can create pores of 5 μm in diameter, as reported in Fig. 20. The precise connection between acoustic pressure and the extent of interendothelial junction opening remains a subject of uncertainty.

Effect of permeabilization extent on cellular resealing Hu et al. [221] also reported the time course of membrane perforation and its recovery, revealing that pores with an area smaller than 30 μm^2 were able to successfully reseal, whereas pores larger than 100 μm^2 did not exhibit resealing capabilities. Additionally, they showed that in cases of successful membrane resealing, the process typically reaches completion within 1 min following the initiation of sonoporation, as shown in Fig. 20. This finding aligns well with pore resealing observed using the patch-clamp technique, indicating that the perforated membrane typically restores its integrity within 100 s [206,212,222]. Furthermore, the variations over time in the fluorescence of PI internalized within the cytoplasm following sonoporation can also be correlated with the resealing duration of the pores, demonstrating a coherent alignment with previous methods [212,215,223]. Surprisingly, Beekers et al. [223] discovered no discernible link between pore size and the time it takes for resealing. The authors proposed that the inherent variability among cells exerts a greater influence on membrane resealing than the size of the pores. Regarding the gaps between endothelial cells, Helfield et

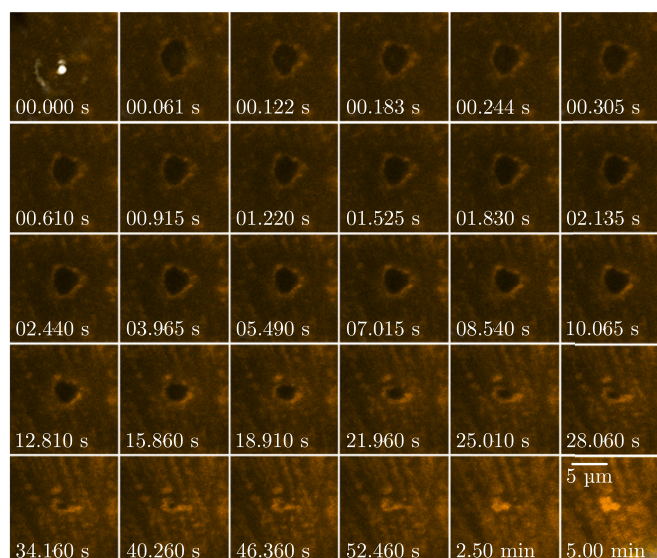


Fig. 20. Time-series confocal fluorescence images revealing localized membrane perforation and recovery induced by the ultrasound-triggered collapse of a single microbubble. The microbubble adhering to the cellular membrane is depicted in white and its diameter is 1.8 μm . The pore diameter is 5.3 μm . Figure reproduced with permission from the work by Hu et al. [221].

al. [204] discovered that these gaps remained open for several tens of minutes.

5.3. Mechanical action and cellular mechanical permeabilization via phase-change droplets

The acoustic droplet vaporization is a highly energetic event, resulting in droplet interfacial accelerations of up to 10^6 m s^{-2} . This extremely fast expansion can generate significant impact forces on the neighboring tissues [166]. Furthermore, when vaporized, these agents exhibit analogous mechanical stress mechanisms to that of microbubbles [35,39,41]. It has also been shown by Fiorini et al. [169] that the interaction between the nucleated bubble and the acoustic wave inside the droplet can induce jets that are capable of piercing the encapsulating shell and impacting the surroundings. The resulting water hammer pressure from these jets can reach approximately 10 MPa.

In-vitro studies have shown that phase-change droplets have the ability to enhance tissue permeabilization more effectively than microbubbles [32–34,117,224]. Several studies have hypothesized that the vaporization event is capable of damaging not only the endothelium but also the extracellular matrix (ECM) beyond it [95,97,225]. However, this elevated potential for disruption raises concerns regarding the reversibility of the resulting effects. Fan et al. [33] showed that reversible cellular permeabilization from ADV occurs when the initial droplet-to-cell distance is higher than the stable radius of the post-ADV microbubble. If this distance is too low, the ADV process causes irreversible cell death. Nevertheless, if the initial droplet-to-cell distance exceeds the maximum radius reached by the vaporized droplet, no enhancement in cell permeability occurs. It follows that a high degree of spatial precision is required to achieve reversible cell permeabilization from ADV. Qin et al. [34] confirmed these findings and further reported a decrease in cell viability as droplet concentration, ultrasound amplitude, and pulse duration increased. The studies mentioned above highlight the difficulty in controlling and monitoring reversible sonoporation induced by acoustic droplet vaporization. Therefore, contemporary research on ADV-based therapy has shifted its emphasis toward drug delivery meant to treat tumors and cancers where cell death caused by mechanical effects is complementary to the pharmaceutical therapy [35,97].

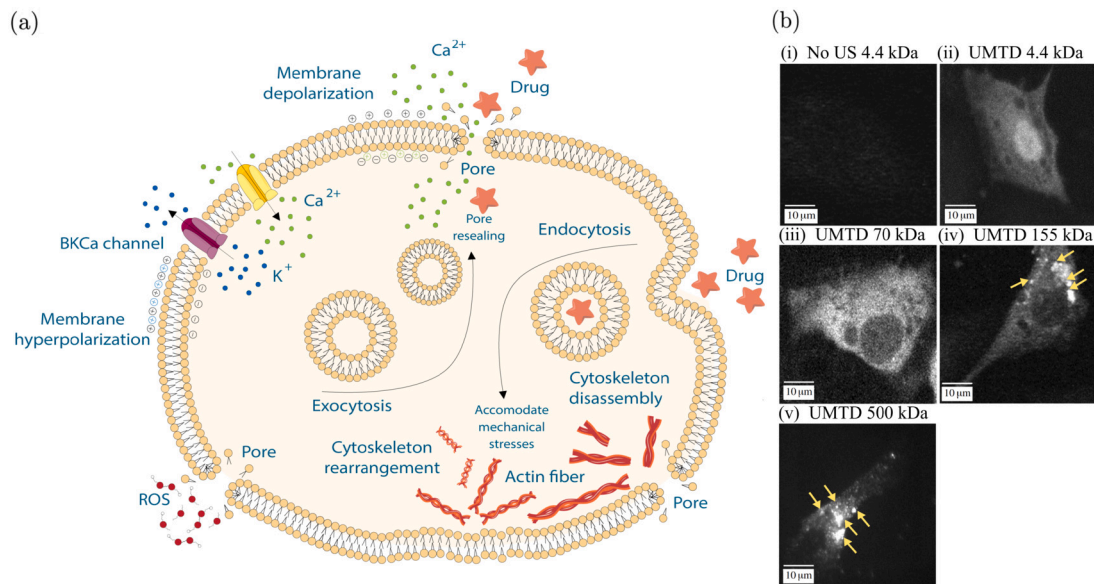


Fig. 21. (a) The illustration depicts the different bioeffects arising from sonoporation contributing to endocytosis-mediated drug delivery. (b) Cellular distribution of different molecular weight fluorescent dextrans after ultrasound and microbubble target delivery (UMTD). The images show homogeneous distribution in the cytosol and in the nucleus of 4.4 kDa dextran after UMTD (ii) compared to treatment in the absence of ultrasound (i), homogeneous distribution of 70 kDa dextran only in the cytosol (iii), heterogeneous distribution of 155 kDa, mainly localized in vesicle-like structures (see arrows in (iv)), and prominent vesicular-like localization of 500 dextran kDa (see arrows in (v)). Scale bar represents 10 μm . Figure reproduced with permission from the work by Meijering et al. [240].

5.4. Biophysical response of cells

Enhanced permeability is not solely a result of physical cell membrane disruption. The agent's mechanical action can trigger cellular signaling pathways and elicit various biological responses, including the facilitation of drug delivery through the promotion of endocytosis, as illustrated in Fig. 21 (a).

Intracellular calcium ion fluctuations After the formation of pores in the cell membrane, ions are driven into the cell concurrently with the influx of extracellular molecules. Calcium ions (Ca^{2+}) hold significant importance due to their central role in regulating cellular functions through a steep concentration gradient between the extracellular ($[\text{Ca}^{2+}] \approx 1 \text{ mmol L}^{-1}$) and intracellular ($[\text{Ca}^{2+}] < 1 \mu\text{mol L}^{-1}$) space. When the cytosolic Ca^{2+} concentration rises, it triggers a cellular response through calcium-mediated signaling to restore cellular homeostasis. Several efforts have been made to explore the connection between intracellular Ca^{2+} transients and sonoporation and their relationship with the onset of bioeffects [226]. Deng et al. [222] were the first to report a reversible increase of trans-membrane current resulting from ions flux through pores generated by ultrasound and microbubble treatment on *Xenopus* oocyte at pressure amplitudes lower than 1 MPa. A related study showed immediate and concurrent intracellular diffusion of PI and increase of intracellular Ca^{2+} following sonoporation [227,228]. However, intracellular Ca^{2+} fluctuations were observed even in the absence of PI uptake, suggesting that ultrasound-driven microbubbles could alter Ca^{2+} concentration within the cell without necessitating membrane poration [229]. A possible interpretation might involve the activation of mechanosensitive ion channels due to the mechanical stress induced by the ultrasound-microbubble interaction [230]. In support of this, Tran et al. [231] found that ultrasound-driven microbubble oscillations near the cell membrane induce a mechanical stretch activating BK_{Ca} channels, resulting in slow and progressive intracellular Ca^{2+} increase. It is worth noting that Ca^{2+} influx itself could potentially activate BK_{Ca} . In both cases, the activation of BK_{Ca} channels also results in cell membrane hyperpolarization by an overcompensating efflux of potassium ions (K^{+}) [232]. Finally, delayed Ca^{2+} fluctuations might also be attributed to Ca^{2+} release from intracellular stores triggered by mechanical stresses on the cell membrane,

or to Ca^{2+} waves propagating beyond the initial site of sonoporation into surrounding cells [233]. The latter highlights the potential impact of Ca^{2+} waves in enhancing vascular permeability through the modulation of Ca^{2+} -mediated disassembly of intercellular junctions [234]. Elevated intracellular Ca^{2+} levels trigger biological responses aiming to either restore normal homeostatic concentrations and cellular functions or induce cell death when the presence of Ca^{2+} is excessive and prolonged. Several studies have established the critical role of intracellular Ca^{2+} fluctuations in the membrane resealing process by showing that in a calcium-deficient environment, there is no decline in trans-membrane ion current after sonoporation, which ultimately leads to cell death. [222,235]. Qin et al. [236] observed that sonoporated cells exhibited diverse responses in terms of plasma membrane potential, with reversible sonoporation causing transient depolarization and irreversible sonoporation resulting in permanent depolarization. Beekers et al. [228] demonstrated a strong correlation between Ca^{2+} fluctuations and the amplitude of microbubble oscillation. Specifically, they observed that only oscillation amplitudes $< 1 \mu\text{m}$ resulted in membrane resealing within 120 second and the complete restoration of homeostasis. Interestingly, they also found that irreversible Ca^{2+} fluctuations, and therefore lasting cellular damage, can occur even in cases where membrane resealing seems to be fully achieved. Furthermore, Jia et al. [237] discovered that the sonoporation-induced mechanical damage results in a corresponding increase in the production of reactive oxygen species (ROS), which exhibits a temporal correlation with the influx of Ca^{2+} . It is important to note that high ROS levels can result in cell death. Nevertheless, an increase of 50% and 110% in both intracellular hydrogen peroxide (H_2O_2) and intracellular Ca^{2+} fluctuations, following an ultrasound-microbubble treatment at a MI of 0.1 and 0.5, respectively, did not cause significant alteration in cell viability [238]. Remarkably, H_2O_2 has been established as a contributing factor to the permeability of Ca^{2+} . In fact, the presence of catalase, an extracellular H_2O_2 scavenger, reduces the Ca^{2+} influx induced by ultrasound-driven microbubbles [238,239].

Cytoskeleton disassembly and rearrangement Sonoporation-induced disruption of cellular integrity extends beyond the plasma membrane and encompasses the intricate network of protein fibers constituting the cytoskeleton, as observed by Chen et al. [241] and Helfield et al. [234],

who documented the simultaneous rupture of both the plasma membrane and the actin fibers due to shear stress generated by ultrasound-driven microbubbles. The disintegration of the actin network within sonoporated cells plays an important role in cell fluidization, which facilitates the migration of intracellular vesicles towards the injured site, and therefore, the resealing of pores [242]. However, an extended disassembly of the actin network can affect cellular processes, and potentially trigger cell death. Jia et al. [243] characterized the disruption of the actin cytoskeleton in human umbilical vein endothelial cells (HUVECs) exposed to ultrasound and microbubbles as a dynamic process consisting of three distinct phases: (i) rapid expansion, temporally and spatially correlated to plasma membrane rupture, (ii) contraction and delayed re-sealing correlated to plasma membrane closure, and (iii) gradual recovery. Sonoporated cells that did not successfully complete the contraction phase underwent cell death. The actin recruitment and accumulation along the edge of transendothelial perforations were identified as crucial factors in the resealing of the cell membrane. This process starts when the perforation reaches its maximum size and continues until the membrane is fully restored [234]. Additionally, Juffermans et al. [239] observed an increase of intercellular gaps following the reorganization of actin fibers within HUVECs exposed to ultrasound and microbubbles, hinting at the potential role of the cytoskeleton in influencing cell-cell signaling and regulating endothelial barrier permeability.

Endocytosis Endocytosis is a vital cellular mechanism that enables the internalization of extracellular molecules by enveloping them with the cell membrane by forming vesicles. Ultrasound-responsive agents not only facilitate drug delivery through passive diffusion of drugs into the cytosol via pores or into the extracellular space through opened junctions but also activate endocytic pathways through sonoporation bioeffects, enhancing the overall drug delivery process [244]. Various studies have suggested that Ca^{2+} signaling is implicated in different aspects of ultrasound-microbubble-mediated endocytosis, including the regulation of the turnover of pits in clathrin-mediated endocytosis [245], the activation of proteins associated with fluid phase endocytosis [246], and the vesiculation of membrane domains rich in cholesterol [247]. Moreover, Ca^{2+} influx through the pores triggers endocytosis or exocytosis for the resealing of the injured plasma membrane. Fekri et al. [248] discovered that increased lysosomal exocytosis following sonoporation is essential for clathrin-mediated endocytosis, whereas no reliance was observed for fluid-phase endocytosis. These findings imply that enhanced endocytosis induced by ultrasound and microbubbles can occur through distinct mechanisms. Caveolae may undergo disassembly and reassembly in response to mechanical stresses experienced at the plasma membrane. Indeed, an increased number of uncoated pits, associated with caveolae-endocytosis pathways, was observed at the plasma membrane after ultrasound and microbubble treatment [249]. Moreover, the activation of BK_{Ca} channels by sonoporation-mediated Ca^{2+} influx and the consequent hyperpolarization of the cell membrane, might facilitate the uptake of macromolecules through endocytosis [232]. Meijering et al. [240] examined the role of endocytosis in the process of drug internalization following treatment with microbubbles in combination with 1 MHz-pulsed-ultrasound with 0.22 MPa of PNP. Their findings indicated that when endocytic pathways were inhibited, the uptake of large dextrans decreased, while the uptake of small dextrans remained unchanged. Consequently, they postulated that larger molecules (> 155 kDa) likely undergo internalization through endocytosis, whereas smaller molecules are presumed to enter the cell via diffusion through the transient pores (Fig. 21 (b)). Likewise, Delalande et al. [250] suggested clathrin-mediated endocytosis to be the primary pathway for the delivery of high-molecular-weight plasmid DNA. Nevertheless, clathrin-mediated endocytosis' involvement in the uptake of small molecules (\approx 600 Da) has also been reported [251]. It is worth emphasizing that the mechanism of drug delivery depends heavily on ultrasound parameters, and therefore on the size of the membrane

openings [211]. In fact, Geers et al. [252] observed that microbubbles experiencing inertial cavitation promote direct cytoplasmic entry of adeno-associated viruses attached on the surface of the microbubble without involving endocytosis.

5.5. Experimental models to study enhanced permeabilization

Due to the challenging spatial and temporal scales involved in the dynamics of ultrasound-responsive agents and the difficulties associated with having physical optical access, the majority of studies investigating the mechanisms of enhanced permeabilization prefer to utilize *in-vitro* or *ex-vivo* systems, as they offer a more controlled experimental environment. Initially, investigations on microbubble-mediated sonoporation were carried out using a freely suspended cell medium [205,253]. Despite the substantial insights gained in these studies, the physiological relevance of this experimental setup is questionable. In fact, in physiological conditions, microbubbles, which are confined to the vasculature due to their large size, rarely come into contact with freely suspended target cells. Instead, their primary target is the endothelial cell layer that lines the interior of the blood vessels. To address this concern, researchers started adopting flat platforms where single-cell layers can be cultivated for studying both the dynamics of the bubble and the uptake of cells. A variety of cells, spanning from endothelial to various tumor cells, have been employed [98,201,204,223,228,240,250,254–258]. Nevertheless, when considering the factors previously mentioned, only endothelial cells can be considered the correct choice. The cells were typically cultivated on a thin, rigid, and porous polymer substrate (such as Opticell™ or CLINicell) mainly because of their optical and acoustic transparency. However, even these configurations remain structurally and mechanically different from the living vasculature. Indeed, microbubbles primarily act within capillaries. Therefore, investigating their dynamics using flat substrates disregards confinement effects (see Sec. 4.3). Moreover, the membranes used in Opticell™ and CLINicell, exhibit significantly higher stiffness compared to the majority of human tissues (see Fig. 22) and, owing to the limited thickness of the cell layer, their influence must be considered when assessing the properties of the substrate [259]. Brujan et al. [260] have shown that the behavior of a cavitation bubble close to a substrate depends strongly on the elastic modulus of the substrate as well as the distance from the substrate. These factors influence the bubble jetting direction, jet velocity, bubble translation, bubble oscillation times, and cavitation erosion, all of which hold significant relevance in the context of sonoporation-induced drug delivery. Although this study focused on larger laser-induced bubbles, similar variations in microbubble behavior have been observed, particularly concerning the jetting direction for different substrates [199,200,207]. However, the precise effect of the substrate and the backing membrane stiffness on the microbubble behavior and sonoporation efficiency still needs to be systematically studied. Some studies have employed *ex-vivo* models of real animal tissues [145,207,208], which better replicate physiological conditions. Nonetheless, establishing controlled experimental conditions using these models proves to be considerably more challenging than *in-vitro* setups. As of now, a proper *in-vitro* testing model for the characterization of agent-induced sonoporation is still lacking. The ideal experimental model should be tailored to the target tissue of interest and should accurately replicate the mechanical and structural characteristics found *in vivo*.

5.6. Mechanical properties of cells and tissues

Characterizing the mechanical properties, such as stiffness and deformability (or viscoelasticity) of cells and tissues *in vivo* is essential for designing the ideal *in-vitro* test models for experiments. In fact, these mechanical properties not only impact agent dynamics but also have a direct correlation to cell mechanotransduction, influencing how mechanical stimuli are translated into biological effects.

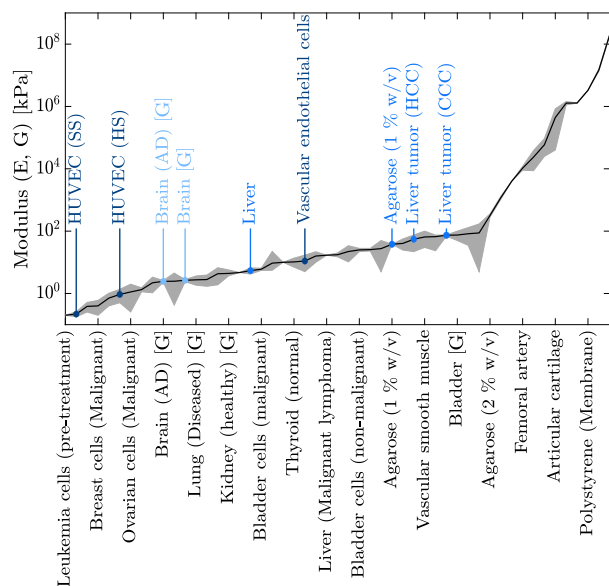


Fig. 22. The stiffness of cells, tissues, and tissue-mimicking materials: If the shear modulus is plotted for a tissue, then it is labeled with [G]. The stiffness values span from a few Pa to a few GPa [264]. The dark gray region indicates the degree of variability in the reported values wherever multiple studies were available. A few interesting highlights are pointed out directly on the graph. Culturing HUVEC's on soft (SS) or harder (HS) substrates changes their stiffness by two or three-fold [267]. Diseased tissues generally have a different stiffness compared to healthy tissues as highlighted by comparing the brain stiffness of patients with and without Alzheimer's disease (AD) [268]. Tumors generally increase the stiffness of tissues, with a degree of variability dependent on the type of tumor, as indicated here for the liver with hepatocellular carcinoma (HCC) and cholangiocellular carcinoma (CCC) [269]. Polystyrene membranes that are used widely as substrates for culturing cells have a much higher elastic modulus than tissues [270], whereas agarose substrates mimic the mechanical stiffness of tumors very well [39,271].

Measurements of cell stiffness are typically performed at the micro- and nanoscale using micropipette aspiration [261], cytometry [262], or Atomic Force Microscopy (AFM) indentation [263]. On the other hand, tensile/compressive deformation techniques and cyclic loading tests *in vitro* [264], or elastography techniques *in vivo* [265] are used to measure the tissue stiffness in macroscale. The modulus of different cells, tissues, and typical substrates is depicted in Fig. 22. Although the variations among different cell types are slight, there is a significant difference in tissue moduli. The interaction of the cell with the ECM, and the characteristics of the ECM components, such as the concentration, structure, and organization of the stress fibers within the cytoskeleton, the amount of actin-binding proteins, and more, dictate the stiffness of tissues, thereby providing significant variations in the modulus values. The cell-ECM interactions and their implications on stiffness are discussed in the recent reviews by Kwon et al. [266] and Guimarães et al. [264].

Additionally, marked changes in the microcirculation environment around cells can lead to changes in cell and tissue stiffness, as illustrated in Fig. 22. This phenomenon may serve as a potential biomarker to detect fibrosis, cancers, and chronic diseases [268,272–274]. Most studies have shown that cancer cells are less stiff than healthier cells [274–277]. Nevertheless, others have reported either minimal changes [273], or the opposite trend in the stiffness of malignant and non-malignant cells respectively [278]. Regardless of these disparities, the proliferation and abnormal growth of cancer cells, along with the ECM deposition and stiffening in tumor microenvironments, imply that cancer increases the surrounding tissue stiffness [269,272,279]. It has also been shown that cells subjected to chemotherapy experience an increase in their stiffness values, with the type of drug used influencing the rate of change of stiff-

ness [280,281]. With respect to chronic diseases, Murphy et al. [268] noticed that the global brain stiffness decreases in patients with dementia and Alzheimer's disease, with the stiffness further decreasing with increasing severity of impairment. Interestingly, HUVECs, which are endothelial cells commonly used for sonoporation studies, have a lower stiffness than most vascular endothelial cells, and further show varying stiffness values depending on substrate hardness [267]. These heterogeneities in cellular and tissue mechanical properties further highlight the importance of measuring the mechanical properties of cells and tissues and of accurately reproducing these properties when setting up experiments.

6. Drug delivery

The mechanical stress generated by ultrasound-responsive agents under acoustic exposure and the following bioeffects, presented in Sec. 5, have been shown to provide a way to overcome biological barriers in drug delivery to the brain and other targets. This section offers a comprehensive overview of therapy based on ultrasound-responsive agents, highlighting the results obtained *in vivo*, and the limiting factors that hinder an effective clinical translation.

6.1. Brain drug delivery

In the treatment of neurological disorders, the delivery of drugs to the brain parenchyma is hindered by the blood-brain barrier (BBB), i.e., a selectively permeable layer of highly interconnected endothelial cells aimed at the regulation of homeostasis and protection of the central nervous system (CNS). The BBB acts as a physicochemical exclusion filter, enabling the diffusion of hydrophobic and low molecular weight molecules (< 400 Da) only. The paracellular space is physically sealed by tight junctions consisting of transmembrane proteins (mainly occludins and claudins), anchored to the cytoskeletons of adjacent endothelial cells through zonula occludens (ZO) proteins. From a functional perspective, a high expression of active efflux transporters and almost inactive endocytosis in endothelial cells hinder transcellular trafficking. Only nutrients, hormones, and plasma proteins can cross the BBB via either vesicle-mediated transcytosis or carrier-mediated transport while exogenous, or harmful compounds, are pumped out by active efflux transporters, such as P-glycoproteins (P-gp). Even though the brain tumor microenvironment presents vascular wall fenestration and compromised tight junctions causing BBB disruption, this enhanced vascular permeability is extremely heterogeneous, and infiltrating tumor cells might be found in brain areas characterized by intact BBB. In addition, P-gp are highly expressed in tumors, and contribute to multidrug resistance since many chemotherapeutics are recognized as substrates by active efflux transporters, which pump them out of the cell and prevent them from crossing the BBB [282].

Ultrasound and microbubble-mediated BBB opening The mechanical effects generated by the interactions between ultrasound, agents, and tissues, alter the physical and functional properties of the BBB. Hynynen et al. [283,284] were the first to demonstrate that ultrasound treatment combined with microbubbles enhances BBB permeability, via both transendothelial and paraendothelial routes. Related pre-clinical studies showed a transient inhibition of occludin, claudin-5, and ZO-1 protein expression in both healthy and glioma-bearing rats, suggesting that the tracer was able to leak from the vessels to the brain through paracellular routes [285,286]. Additionally, Jalali et al. [287] found a reduction of the interaction between occludins and ZO-1 in sonicated brain regions that might be attributed to ultrasound and microbubble-induced activation of signaling pathways in neuronal cells. Further studies have since demonstrated that ultrasound and microbubbles cause BBB dysfunction by up-regulating endocytosis pathways, including caveolae-mediated [288] and clathrin-mediated endocytosis [289], improving transcellular

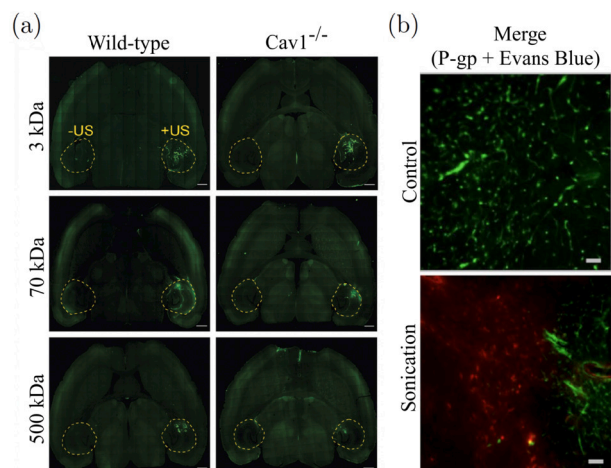


Fig. 23. (a) Effect of ultrasound-microbubble treatment on caveolae-mediated endocytosis. The images show the leakage of different molecular weight dextrans in the hippocampus, comparing control (-US) and sonicated (+US) hemispheres in wild-type and Cav1^{-/-} mice. (b) Partial down-regulation of P-gp expression led to an increase in permeability to Evans Blue dye after ultrasound-microbubble treatment. Fluorescence images of rat brain tissue comparing control and sonicated regions show P-gp expression intensity (green) and Evans Blue dye intensity (red). Scale bar represents 50 μm . Figures reproduced with permission from the work by Pandit et al. [290] (a) and Cho et al. [293] (b).

transport of cargo through the BBB. Out of the two pathways, caveolae-mediated endocytosis has been proposed as the main mechanism for the transport of large molecules, as shown in Fig. 23 (a), which reports the reduced leakage of dextran, with a molecular weight of 500 kDa, in mice lacking vesicle-forming protein, caveolin-1 (Cav1^{-/-}) [290]. Moreover, caveolin phosphorylation [291] and increased expression of K_{Ca} channels [292] have been proposed as possible mechanisms involved in ultrasound and microbubble-mediated endocytosis in both healthy and glioma models. Regarding the contribution of active efflux transporters to the BBB function, several studies reported transient modulation of P-gp expression using focused ultrasound (FUS) combined with microbubbles in rat models, as shown in Fig. 23 (b) [293,294]. Choi et al. [295] found that the down-regulation of P-gp levels is associated with the activation of the kinase pJNK pathway by ultrasound-induced stress. Moreover, Zhang et al. [296] showed that down-regulation of P-gp and multidrug resistance proteins observed following low-intensity ultrasound treatment (142 mW cm⁻²) increases the sensitivity of glioma to doxorubicin. Nevertheless, Goutal et al. [297,298] recently suggested that the down-regulation of P-gp induced by FUS might be insufficient for paracellular trafficking of compounds with a high-affinity to P-gp. Further investigations are needed to assess the ultrasound and microbubble-mediated BBB disruption on the delivery of compounds whose distribution into the brain relies predominantly on P-gp-mediated efflux activity rather than the physical barrier.

Ultrasound and microbubble-mediated interstitial modulation After extravasation, drugs enter the extracellular space, which is formed by an electrically charged nanoporous matrix that hampers drug penetration. Brain tumors and metastases are generally characterized by a high interstitial fluid pressure which further hinders drug transport. In addition to transient BBB opening, new studies have accredited microbubble activity for interstitial modulation as well. FUS treatment combined with microbubbles has been shown to increase the interstitial fluid flow velocities [299] as well as shifting the drug transport in the interstitial space from being diffusion-driven to being convection-driven [300], resulting in an increase in drug delivery and penetration distance in the brain microenvironment. However, the effects of interstitial modulation on drug delivery remain to be elucidated.

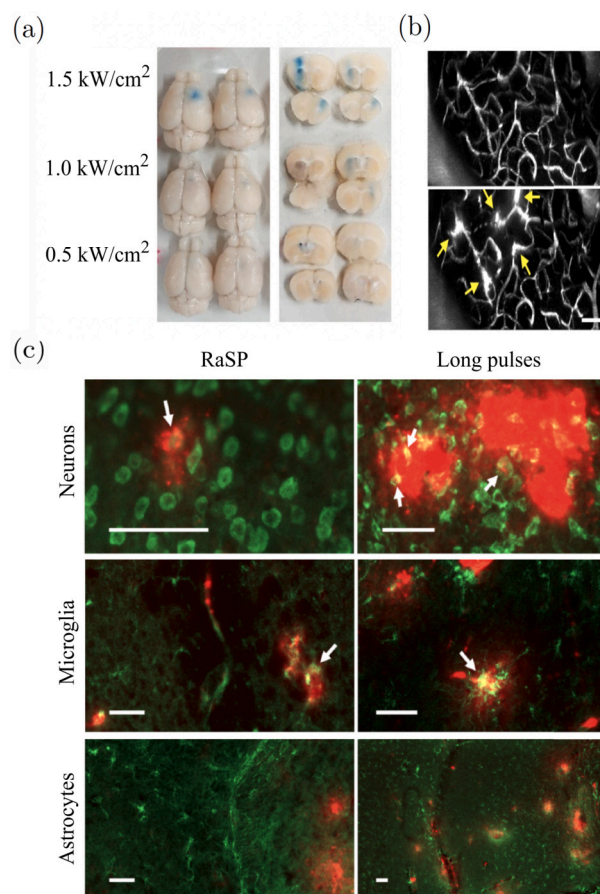


Fig. 24. (a) Evans blue dye extravasation induced by microbubbles injection followed by FUS irradiation to mice brains at various acoustic intensities. (b) Intravital multiphoton microscopy images of mice brain vasculature before (top) and after (bottom) ultrasound-microbubble treatment confirm increased BBB permeability by fluorescent dextran extravasation (scale bar: 50 μm). (c) Effect of ultrasound and microbubble treatment on liposome delivery. Fluorescence images show cellular uptake of liposomes (red) in neurons (top row, green) and microglia (middle row, green) but not in astrocytes (bottom row, green) in rapid short pulse sequence (RaSP) and long pulse sequence treated mice brains. The scale bars indicate 50 μm . Figures reproduced with permission from the work by Ogawa et al. [315] (a), Poon et al. [302] (b), and Morse et al. [92] (c).

Ultrasound and microbubble-mediated drug delivery: preclinical studies BBB enhanced permeability after ultrasound and microbubbles treatments has been confirmed by Evans blue dye extravasation in sonicated areas, as shown in Fig. 24 (a). Using magnetic resonance imaging (MRI), Baseri et al. [301] leveraged the enhanced permeability of gadolinium tracer in the brain to find that the BBB opening starts occurring at a rarefactional pressure amplitude of 0.3 MPa, when employing a frequency of 1.5 MHz, and lasts as long as 24 h [202]. The process is considered completely safe at this pressure owing to the absence of extravasation of red blood cells, at pressures below 0.6 MPa and the absence of neuronal damage below 0.9 MPa. Successful BBB opening *in vivo* has also been demonstrated in real-time using intravital multiphoton microscopy in rat models (see Fig. 24 (b)) [302].

In small animal models, BBB enhanced permeability induced by different combination of ultrasound parameters and microbubbles (either commercially-approved or home-made) resulted in higher concentrations of administered chemotherapeutics [303–309], antibodies [310,311], genes [299], and nanomedicines [312] in the brain. Moreover, Brighi et al. [313] found an increased antibody uptake in the target regions of a tumor presenting intact BBB in high-grade glioma models, further confirming the beneficial effect of ultrasound and microbubbles in enhancing BBB permeability and drug delivery in chal-

lenging tumor areas. FUS and microbubble-assisted gene-nanovectors delivery has been found to result in efficient transfection through particle uptake by different cells, including neurons and astrocytes using 1 MHz single FUS transducer (0.6 MPa, 120 s, 10 ms bursts, 0.5 Hz burst rate) in rat models [314], and microglia and endothelial cells using 3 MHz FUS transducer (0.5–1.5 kW cm⁻², 60 s, 10% duty cycle) in mouse models [315]. At similar ultrasound parameters, Morse et al. [92] found an increase in cellular uptake of liposomes within neurons and microglia using long-pulse FUS sequences (10,000 cycles, PRF: 0.5 Hz). However, shorter pulse sequences (5 cycles, PRF: 1.25 kHz, 10 ms bursts, 0.5 Hz burst rate) required higher acoustic pressures to achieve liposome delivery (see Fig. 24 (c)). Furthermore, Huang et al. [316] found heterogeneous punctuate regions of high concentration of plasmid DNA in the cytoplasm of neurons, confirming the involvement of vesicle-mediated endocytosis with ultrasound and microbubble treatment.

These findings support the promising application of ultrasound-microbubble-mediated drug delivery in the treatment of CNS diseases [317,318]. In glioma models, the enhanced delivery of carboplatin [319,320] and liposomal doxorubicin [321,322] to the brain provoked significant slowing of tumor growth and prolonged survival. A significant reduction in mean tumor volume and an improvement in survival have been also observed in breast cancer brain metastases in rat models after enhanced monoclonal antibody delivery by BBB opening [323]. Moreover, biodistribution studies have shown glioma specificity and reduced drug levels in non-cancer locations, highlighting the potential of microbubble-mediated targeted drug delivery [324]. Regarding neurodegenerative diseases, Jardim et al. [325] reported, for the first time, a reduction in Alzheimer's disease pathology in mouse models after treating them with FUS with microbubbles and anti-A β antibody administration. In Parkinson's disease models, BBB opening has been shown to result in enhanced protein expression in transfected neurons, improving the neuroprotective effect and recovering a normal dopamine secretion [326,327].

Ultrasound and microbubble-mediated drug delivery: clinical studies Clinical trials exploring the feasibility of ultrasound and microbubble-assisted drug delivery to the brain have been recently initiated. The first one, which started in 2014, used an implantable ultrasound system (SonoCloud[®], 1.05 MHz) in combination with SonoVue[®] microbubbles to improve the delivery of carboplatin in patients with recurrent glioblastoma (ClinicalTrials.gov, NCT02253212) [13]. The results demonstrated that a higher acoustic pressure (0.8 MPa) is needed for transient BBB disruption compared to the one required in small animal models (0.5 MPa) [328]. This difference could be attributed to the size of the human skull, which limits standing wave effects compared to smaller animals [329]. No tumor progression was detected in sonicated areas in most of the patients and patients with clear BBB disruption presented longer survival [14]. Recently, an ultrasound and microbubble treatment was performed using a novel device composed of nine SonoCloud[®] ultrasound transducers (SonoCloud-9) to increase the size of sonication field in recurrent glioblastoma patients for the delivery of albumin-bound paclitaxel (NCT04528680) [330]. Other trials have been registered concerning glioblastoma treatments using different therapeutic ultrasound devices. Among non-implantable ultrasound devices, NaviFUS[®], a novel neuronavigation-guided device composed of a 256-element phased array (500 kHz), has recently been employed in combination with FUS-microbubble treatment, showing safe and reversible BBB opening in recurrent glioblastoma patients at doses lower than 0.68 MI (NCT03626896) [331]. Similarly, the ExAblate[®] transcranial device, consisting of a stereotactically positioned helmet of 1024 individually driven transducer elements (220 kHz), providing non-invasive radiation under real-time MRI guidance, has demonstrated safe BBB opening even after repetitive sonications at the same targets, proving the potential feasibility of chemotherapy protocols for brain tumor treatment (NCT02343991 [15], NCT03712293 [332], NCT03322813

[333]). To limit the risk of microhemorrhages, a real-time acoustic emission feedback system has been implemented to record cavitation signals and calculate the optimal power for BBB disruption. This has been set to 50% of the power level at which the activity of microbubbles generates significant inertial cavitation, as first proposed by Huang et al. in their preclinical studies [316]. Furthermore, the ExAblate[®] system has been tested for microbubble-assisted BBB opening and drug delivery in the treatment of different CNS-related diseases, including Her2-positive brain metastases (NCT03714243) [334], Alzheimer's disease (NCT03671889 [335,336], NCT04526262 [337]), Parkinson's disease (NCT03608553 [338]), and amyotrophic lateral sclerosis (NCT03321487) [16].

Although the phase I and II of the clinical trials have demonstrated safe, feasible, and reversible BBB opening, they only represent preliminary findings because of the rather restricted group of tested patients [339]. The lack of a standardized protocol for ultrasound-microbubble assisted drug delivery, and therefore, the insufficient safety data, slows the clinical translation. Another limiting factor is the absence of correlation between preclinical and clinical results, due to anatomical and physiological differences between the models, as described by Carpentier et al. [13].

Ultrasound and droplet-mediated drug delivery: preclinical studies The spatiotemporally controlled vaporization of droplets, induced by ultrasound at the target site, can result in cell apoptosis, enhanced systemic immune response, and improved drug delivery via BBB disruption or enhanced membrane cell permeability. Hence, nanodroplets are also being explored for the treatment of brain tumors [340] or other brain-related diseases, BBB opening [41,341], and neuromodulation [36].

In the field of agent-assisted drug delivery, the interaction between nanodroplets and BBB is a topic of hot debate. Chen et al. [41] showed that the required acoustic pressure threshold for BBB opening is higher with nanodroplets than with microbubbles, while the stable cavitation dose remained lower and no inertial cavitation is detected. Furthermore, more homogeneous dextran delivery is observed within the mouse hippocampus using nanodroplets, compared to microbubbles. Similarly, Wu et al. [342] showed that OFP droplets required lower sonication pressures (~ 300 to 450 kPa) to facilitate drug delivery once the opening of the BBB is achieved, compared to PFB droplets (~ 900 kPa), which has a higher molecular weight. Histology further showed that PFB nanodroplets led to damage of the tissues, due to inertial cavitation of the subsequent microbubbles. Song et al. [341] also noticed sustained inertial cavitation activity generated by a high concentration of PFP droplets, resulting in an enhanced amount, and penetration depth, of extravasated tracers, compared to microbubbles in rat brains. Nevertheless, further investigations are needed to prove the safety of BBB opening induced by ultrasound and nanodroplets.

6.2. Solid tumors drug delivery

Solid tumors are masses of abnormal cells that occur in the bones, tissues (such as muscles or tendons), or organs (such as the liver or kidneys). Tumor cells stimulate pathophysiological alterations in the tumor microenvironment in order to support tumor growth and progression, including mechanisms of drug resistance. Highly proliferating tumor cells initiate uncontrolled angiogenesis in the tumor microenvironment through overexpression of pro-angiogenic factors, resulting in the development of an irregular tumor vascular system, characterized by tortuous and hyperpermeable vessels. This aggressive tumor growth results in lymphatic vessels becoming permeable, compressed, or even obstructed. The combination of fluid leakage from highly permeable blood vessels and impaired lymphatic drainage causes interstitial hypertension and possible intravasation of drugs back to the vessels, whenever the interstitial fluid pressure exceeds the microvasculature pressure. Moreover, the vessel's tortuosity reduces the blood perfusion rate, generating hostile areas of hypoxia that may contribute to drug

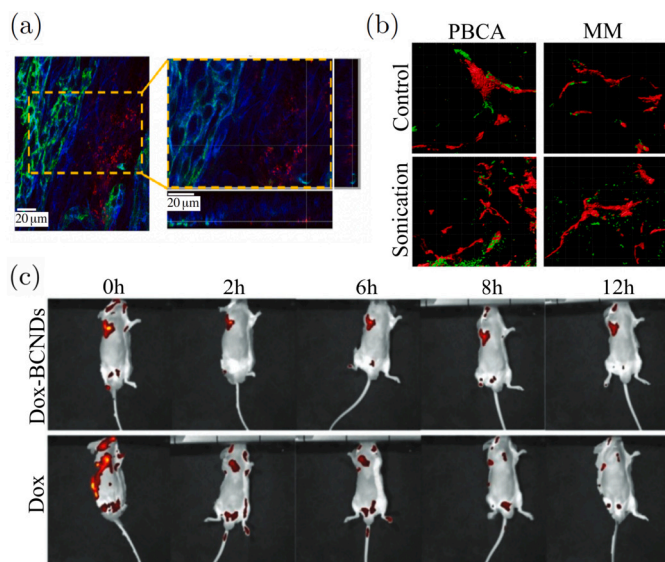


Fig. 25. (a) Effect of ultrasound and microbubble treatment on nanoparticles penetration depth in human colon cancer xenografts in mice. The immunofluorescence image (left) reconstructed from 3D confocal microscopy data sets and the orthogonal slices (right) show extravasated nanoparticles (red) in tumor parenchyma (blue) and away from the vessel lumen (green). (b) Effect of sonoporation on the penetration depth of liposomes (green) from blood vessels (red) in human pancreatic adenocarcinoma xenograft, comparing control and sonoporated tumors using two different MBs (poly butyl cyanoacrylate and MicroMarker™ (VisualSonics) microbubbles). (c) *In-vivo* biodistribution imaging of doxorubicin-loaded nanodroplets compared to doxorubicin alone at different time points in liver cancer-bearing mice after ultrasound treatment. Reproduced with permission from the work by Wang et al. [349] (a), Theek et al. [351] (b), and Zhou et al. [35] (c).

resistance in tumors. Finally, the high proportion of stromal cells in the tumor microenvironment, and the fibrotic nature of the collagen-rich extracellular matrix, further limit drug penetration in the tumor mass. In the last decades, there has been extensive research on applying nanotechnology to improve chemotherapy [343]. Passive accumulation of nanomedicines in tumors, thanks to the EPR effect (see Sec. 3.2), provides advantages concerning reduced toxicity and improved drug bioavailability. Nevertheless, therapeutic outcomes remain limited, in particular, in clinical settings [344].

Ultrasound and microbubble-assisted chemotherapy Ultrasound and microbubbles have been proposed as a promising treatment to overcome biological barriers and enhance chemotherapeutics or nanomedicines accumulation and uptake in the tumor tissue [345,346]. Using a pressure of 0.5 MPa ($MI = 0.5$) and microbubbles stabilized by cabazitaxel-loaded polymeric nanoparticles, Snipstad et al. [347] found increased delivery of cabazitaxel in breast cancer xenografts. No tissue damage was detected and the treatment resulted in complete remission of the tumor. Similarly, Yan et al. [348] demonstrated an improved biodistribution of paclitaxel, resulting in tumor growth inhibition, by using ultrasound (2.25 MHz, 1.9 MPa) and liposome-microbubble complexes. Wang et al. [349] observed a 9-fold increase in the penetration depth of nanoparticles using 3D confocal microscopy after sonoporation in colon cancer xenografts in mice (Fig. 25 (a)). A significant enhancement of liposomal doxorubicin accumulation in colorectal adenocarcinoma xenografts is also found by Lin et al. [350]. Moreover, ultrasound-microbubble treatment resulted in improved extravasation and delivery of liposomes in tumors characterized by low levels of EPR effect (including pancreatic adenocarcinoma, as reported in Fig. 25 (b)) using different ultrasound parameters (1 MHz, $MI = 0.8$ and 16 MHz, $MI = 0.9$) [351,352].

In 2012, these encouraging results paved the way for the first clinical trial, which utilized ultrasound and microbubbles, to administer gemcitabine as a treatment for pancreatic cancer. The trial demonstrated no additional toxicity, compared to chemotherapy alone, and a significant increase in survival, compared to a historical cohort of patients (NCT01674556) [19,353]. However, phase II trials involving a higher number of patients are required to validate the chemotherapy efficacy of ultrasound and microbubble-mediated therapies. It is worth noting that the reported findings may not fully reflect the maximum therapeutic benefits achievable, due to limitations on ultrasound parameters and microbubble dosage imposed by diagnostic scanners and protocols. Recently, multiple clinical trials have been launched to investigate the safety and efficacy of ultrasound and microbubble-enhanced chemotherapy for various cancer treatments, including those targeting malignant digestive system tumors (NCT02233205 [20]).

Droplet-assisted chemotherapy Acoustic vaporization of extravasated nanodroplets can have a direct influence on cancer cells [32]. Several *in-vivo* studies have shown the benefit of ultrasound-induced nanodroplet vaporization in targeted drug delivery to solid tumors (Fig. 25 (c)) [35,71,97,354]. The destructive effect induced by the violent vaporization process appears to be a primary factor for the enhanced drug delivery to cells observed in these studies.

Recently, Spatarelu et al. [355] showed an enhanced delivery of two chemotherapeutics, doxorubicin, and paclitaxel, in a triple-negative breast cancer mouse model using ultrasound and PFP nanodroplets, resulting in reduced tumor growth rate. Owing to the limited number of studies proving the safety of the treatment, droplet-assisted drug delivery has not been investigated in human trials yet. Concurrently, given their more destructive nature, nanodroplets have also been vastly utilized for enhanced therapy in ablation techniques. *In-vivo* preclinical studies of thermal ablation have shown improved heating for tumor treatment using nanodroplets [356]. Moreover, when utilizing nanodroplets as cavitation nuclei, studies have demonstrated their ability to lower the applied pressures required for ablation [39,357].

7. Future outlooks and conclusion

Ultrasound-responsive microbubbles and nanodroplets are rapidly evolving as a dominant drug delivery technique thanks to their ability to enhance membrane permeabilization. The spatiotemporal specificity and reversible poration capability provided by microbubbles are especially advantageous for drug delivery to the brain, making them the only known safe and non-invasive method to transiently disrupt the blood-brain barrier. Despite the increased use of these agents in both pre-clinical and clinical studies, there remain numerous major obstacles that prevent a swift clinical translation, some of which are listed in Table 2.

Among the identified challenges, the most concerning is our lack of understanding of the exact mechanism responsible for cellular permeabilization. It is necessary to identify the responsible mechanism(s) to optimize both the acoustic input parameters as well as the safety of the therapeutic protocol. We believe tackling this requires a combined effort from various fronts, such as (i) understanding the cause of heterogeneity currently observed in microbubble responses in order to improve the reproducibility of the therapy; (ii) designing an ideal *in-vitro* environment that mimics accurately the biological and mechanical properties of cells and tissues in order to predict the true microbubble behavior *in vivo*; and (iii) improving our ability to explore microbubble behavior *in vivo* in order to confirm the validity of the *in-vitro* predictions.

The major drawback limiting the clinical translation of nanodroplets is the current inability to safely vaporize them. There is therefore a need to expand our knowledge of the exact vaporization mechanism to help optimize the input acoustic parameters as well as to develop phase-

Table 2
Obstacles identified for further improvement in agent-induced sonoporation.

Obstacle	Solution
Heterogeneity in microbubble response	Explore fabrication techniques to generate microbubbles with acoustically similar properties.
Accelerated blood clearance of agents	More research is needed to gauge its effects on agents <i>in vivo</i> . Explore alternatives of PEG that minimizes accelerated clearance.
Rapid gas exchange	Explore different (stiffer) shells to improve gas retention inside microbubbles, especially for therapeutic gas delivery.
Unidentified agent dosage	It is essential to move past the imaging concentration limit and investigate the optimum dosage of agents needed for drug delivery without hampering the safety.
Mechanical Index is not ideal to estimate safety	Explore alternatives such as a linear index or develop an universal metric for measuring the cavitation activity from real-time acoustic measurements.
High pressure thresholds for ADV	Understand the actual mechanism of ADV to improve on their performance. Design agents that are able to vaporize at physiologically safe pressure amplitudes. Explore ultrasound parameters that enhance droplet vaporization.
Unknown fate of bubbles post-ADV	More research is needed to study the microbubble stability after ADV. Comprehensive investigation needed to confirm re-condensation of nanodroplets.
Efficacy of attached vs co-administered drugs	Further research dedicated to comparing the different drug delivery techniques is needed to elucidate their efficacy.
Potency of targeted vs non-targeted microbubbles	Comprehensive pre-clinical as well as clinical comparison is needed to ascertain which is better for membrane permeabilization.
Heterogeneity of acoustic protocols used	Make studies comparable by using similar or comparable acoustic parameters.
Effect of various sonoporation mechanisms	Comprehensive pre-clinical comparison of the responses to varying acoustic parameters is needed to ascertain the best mechanism for maximal drug delivery efficiency.
Lack of an ideal <i>in-vitro</i> test setup	Advancements in the current fabrication techniques is needed to mimic the physiological surrounding and mechanical properties.
Unknown effects of currently used substrates on agent response	Quantify the differences in agent behavior for different substrates. Verify if this is comparable with <i>in-vivo</i> agent response.
<i>In-vivo</i> visualization of microbubble response	To ascertain the physiological behavior of microbubbles, <i>in-vivo</i> characterization techniques (such as intravital microscopy) needs to be advanced to incorporate higher temporal and spatial resolutions.
Uncertainty in dominant cellular permeabilization mechanism	Finding solutions to the obstacles listed above should give us a clear idea on the dominant mechanism.

change agents that are both thermodynamically stable and easier to vaporize at clinical acoustic parameters.

Deciphering the intricate interplay between the mechanical response of the acoustically-activated agents and the resulting biochemical response of the cells will further establish their critical role in the future of drug delivery.

Declaration of competing interest

The authors declare that they have no known competing financial interests or personal relationships that could have appeared to influence the work reported in this paper.

Data availability

No data was used for the research described in the article.

Acknowledgements

The authors gratefully acknowledge the financial support from the Swiss National Science Foundation (SNF_200567) and ETH Zurich (Research Grant 1-010206-000). The authors would also like to acknowledge Ms. Gaia Codoni for preparing the illustration presented in Fig. 1.

References

- [1] M. Mitchell, M. Billingsley, R. Haley, M. Wechsler, N. Peppas, R. Langer, Engineering precision nanoparticles for drug delivery, 20 (2) (2021) 101–124, <https://doi.org/10.1038/s41573-020-0090-8>.
- [2] Y. You, L. He, B. Ma, T. Chen, High-drug-loading mesoporous silica nanorods with reduced toxicity for precise cancer therapy against nasopharyngeal carcinoma, 27 (42) (2017) 1703313, <https://doi.org/10.1002/adfm.201703313>.
- [3] K. Baba, H.E. Pudavar, I. Roy, T.Y. Ohulchansky, Y. Chen, R.K. Pandey, P.N. Prasad, New method for delivering a hydrophobic drug for photodynamic therapy using pure nanocrystal form of the drug, 4 (2) (2007) 289–297, <https://doi.org/10.1021/mp060117f>.
- [4] M. Ménard, F. Meyer, K. Parkhomenko, C. Leuvre, G. Francius, S. Bégin-Colin, D. Mertz, Mesoporous silica templated-albumin nanoparticles with high doxorubicin payload for drug delivery assessed with a 3-d tumor cell model, 1863 (2) (2019) 332–341, <https://doi.org/10.1016/j.bbagen.2018.10.020>.
- [5] L. Yang, Y. Yang, Y. Chen, Y. Xu, J. Peng, Cell-based drug delivery systems and their *in vivo* fate, 187 (2022) 114394, <https://doi.org/10.1016/j.addr.2022.114394>.
- [6] N. Nishiyama, K. Kataoka, Current state, achievements, and future prospects of polymeric micelles as nanocarriers for drug and gene delivery, 112 (3) (2006) 630–648, <https://doi.org/10.1016/j.pharmthera.2006.05.006>.
- [7] L. Sercombe, T. Veerati, F. Moheimani, S.Y. Wu, A.K. Sood, S. Hua, Advances and challenges of liposome assisted drug delivery, 6 (2015), <https://doi.org/10.3389/fphar.2015.00286>.
- [8] A.C. Anselmo, S. Mitragotri, Nanoparticles in the clinic: an update, 4 (3) (2019) e10143, <https://doi.org/10.1002/btm2.10143>.
- [9] C. Sierra, C. Acosta, C. Chen, S.-Y. Wu, M. Karakatsani, M. Bernal, E. Konofagou, Lipid microbubbles as a vehicle for targeted drug delivery using focused ultrasound-induced blood-brain barrier opening, 37 (4) (2017) 1236–1250, <https://doi.org/10.1177/0271678X16652630>.
- [10] B. Baseri, J. Choi, T. Deffieux, G. Samiotaki, Y.-S. Tung, O. Olumolade, S. Small, B. Morrison, E. Konofagou, Activation of signaling pathways following localized

- delivery of systemically administered neurotrophic factors across the bloodbrain barrier using focused ultrasound and microbubbles, 57 (7) (2012), <https://doi.org/10.1088/0031-9155/57/7/N65>.
- [11] G. Samiotaki, C. Acosta, S. Wang, E. Konofagou, Enhanced delivery and bioactivity of the neurotrophin neurotrophic factor through focused ultrasound - mediated blood-brain barrier opening in vivo, 35 (2015) 611–622, <https://doi.org/10.1038/jcbfm.2014.236>.
- [12] S. Wang, O. Olumolade, T. Sun, G. Samiotaki, E. Konofagou, Noninvasive, neuron-specific gene therapy can be facilitated by focused ultrasound and recombinant adeno-associated virus, 22 (1) (2015) 104–110, <https://doi.org/10.1038/gt.2014.91>.
- [13] A. Carpentier, M. Canney, A. Vignot, V. Reina, K. Beccaria, C. Horodyckid, C. Karachi, D. Leclercq, C. Lafon, J.-Y. Chapelon, L. Capelle, P. Cornu, M. Sanson, K. Hoang-Xuan, J.-Y. Delattre, A. Idbaih, Clinical trial of blood-brain barrier disruption by pulsed ultrasound, 8 (343) (2016), <https://doi.org/10.1126/scitranslmed.aaf6086>.
- [14] A. Idbaih, M. Canney, L. Belin, C. Desseaux, A. Vignot, G. Bouchoux, N. Asquier, B. Law-Ye, D. Leclercq, A. Bissery, Y. De Rycke, T. Clementine, L. Capelle, M. Sanson, K. Hoang-Xuan, C. Dehais, C. Houillier, F. Laigle-Donadey, B. Mathon, A. André, C. Lafon, J.-Y. Chapelon, J.-Y. Delattre, A. Carpentier, Safety and feasibility of repeated and transient blood-brain barrier disruption by pulsed ultrasound in patients with recurrent glioblastoma, 25 (13) (2019) 3793–3801, <https://doi.org/10.1158/1078-0432.CCR-18-3643>.
- [15] T. Mainprize, N. Lipsman, Y. Huang, Y. Meng, A. Bethune, S. Ironside, C. Heyn, R. Alkins, M. Trudeau, A. Sahgal, J. Perry, K. Hynynen, Blood-brain barrier opening in primary brain tumors with noninvasive MR-guided focused ultrasound: a clinical safety and feasibility study, 9 (1) (2019) 321, <https://doi.org/10.1038/s41598-018-36340-0>.
- [16] A. Abraham, Y. Meng, M. Llinas, Y. Huang, C. Hamani, T. Mainprize, I. Aubert, C. Heyn, S.E. Black, K. Hynynen, N. Lipsman, L. Zinman, First-in-human trial of blood-brain barrier opening in amyotrophic lateral sclerosis using MR-guided focused ultrasound, 10 (4373) (2019), <https://doi.org/10.1038/s41467-019-12426-9>.
- [17] L. Qian, B. Thapa, J. Hong, Y. Zhang, M. Zhu, M. Chu, J. Yao, D. Xu, The present and future role of ultrasound targeted microbubble destruction in preclinical studies of cardiac gene therapy, 10 (2) (2018) 1099–1111, <https://doi.org/10.21037/jtd.2018.01.101>.
- [18] H. Yuan, H. Hu, J. Sun, M. Shi, H. Yu, C. Li, Y. Sun, Z. Yang, R. Hoffman, Ultrasound microbubble delivery targeting intraplaque neovascularization inhibits atherosclerotic plaque in an APOE-deficient mouse model, 32 (5) (2018) 1025–1032, <https://doi.org/10.21873/invivo.11342>.
- [19] G. Dimcevski, S. Kotopoulos, T. Bjanec, D. Hoem, J. Schjøtt, B.T. Gjertsen, M. Biermann, A. Molven, H. Sorbye, E. McCormack, M. Postema, O.H. Gilja, A human clinical trial using ultrasound and microbubbles to enhance gemcitabine treatment of inoperable pancreatic cancer, 243 (2016) 172–181, <https://doi.org/10.1016/j.jconrel.2016.10.007>.
- [20] Y. Wang, Y. Li, K. Yan, L. Shen, W. Wang, J. Gong, K. Ding, Clinical study of ultrasound and microbubbles for enhancing chemotherapeutic sensitivity of malignant tumors in digestive system, 30 (5) (2018) 553–563, <https://doi.org/10.21147/j.issn.1000-9604.2018.05.09>.
- [21] B. Sreedhar, S. Albert, A. Pandit, Cavitation damage: theory and measurements – a review, 372–373 (2017) 177–196, <https://doi.org/10.1016/j.wear.2016.12.009>.
- [22] K. Wei, A. Jayaweera, S. Firoozan, A. Linka, D. Skyba, S. Kaul, Quantification of myocardial blood flow with ultrasound-induced destruction of microbubbles administered as a constant venous infusion, 97 (5) (1998) 473–483, <https://doi.org/10.1161/01.CIR.97.5.473>.
- [23] R. Vogel, A. Indermühle, J. Reinhardt, P. Meier, P. Siegrist, M. Namdar, P. Kaufmann, C. Seiler, The quantification of absolute myocardial perfusion in humans by contrast echocardiography: algorithm and validation, 45 (5) (2005) 754–762, <https://doi.org/10.1016/j.jacc.2004.11.044>.
- [24] S. Wilson, P. Burns, D. Muradali, J. Wilson, X. Lai, Harmonic hepatic US with microbubble contrast agent: initial experience showing improved experience showing improved characterization of hemangioma, hepatocellular carcinoma, and metastasis, 215 (1) (2000) 153–161, <https://doi.org/10.1148/radiology.215.1.r00ap08153>.
- [25] S.-J. Rim, H. Leong-Poi, J. Lindner, D. Couture, D. Ellegala, H. Mason, M. Durieux, N. Kassel, S. Kaul, Quantification of cerebral perfusion with “real-time” contrast-enhanced ultrasound, 104 (21) (2001) 2582–2587, <https://doi.org/10.1161/hc4601.099400>.
- [26] K. Wei, E. Le, J.-P. Bin, M. Coggins, J. Thorpe, S. Kaul, Quantification of renal blood flow with contrast-enhanced ultrasound, 37 (4) (2001) 1135–1140, [https://doi.org/10.1016/S0735-1097\(00\)01210-9](https://doi.org/10.1016/S0735-1097(00)01210-9).
- [27] S. El Kadi, T.R. Porter, N.J. Verouden, A.C. Van Rossum, O. Kamp, Contrast ultrasound, sonothrombolysis and sonoperfusion in cardiovascular disease, 15 (2) (2022) 345–360, <https://doi.org/10.1016/j.jcmg.2021.07.028>.
- [28] K.J.B. Bautista, J. Kim, Z. Xu, X. Jiang, P.A. Dayton, Current status of sub-micron cavitation-enhancing agents for sonothrombolysis, 49 (5) (2023) 1049–1057, <https://doi.org/10.1016/j.ultrasmedbio.2023.01.018>.
- [29] C.M. Sehgal, P.H. Arger, C.R. Pugh, Sonographic enhancement of renal cortex by contrast media, 14 (10) (1995) 741–748, <https://doi.org/10.7863/jum.1995.14.10.741>.
- [30] F. Forsberg, J.B. Liu, D.A. Merton, N.M. Rawool, B.B. Goldberg, Parenchymal enhancement and tumor visualization using a new sonographic contrast agent, 14 (12) (1995) 949–957, <https://doi.org/10.7863/jum.1995.14.12.949>.
- [31] T. Albrecht, D.O. Cosgrove, J.-M. Correia, L. Rallidis, P. Nihyanopoulos, N. Patel, Renal, hepatic, and cardiac enhancement on Doppler and gray-scale sonograms obtained with EchoGen, 3 (1996) S198–S200, [https://doi.org/10.1016/S1076-6332\(96\)80533-2](https://doi.org/10.1016/S1076-6332(96)80533-2).
- [32] S.M. Fix, A. Novell, Y. Yun, P.A. Dayton, C.B. Arena, An evaluation of the sonoporation potential of low-boiling point phase-change ultrasound contrast agents in vitro, 5 (1) (2017) 7, <https://doi.org/10.1186/s40349-017-0085-z>.
- [33] C.-H. Fan, Y.-T. Lin, Y.-J. Ho, C.-K. Yeh, Spatial-temporal cellular bioeffects from acoustic droplet vaporization, 8 (20) (2018) 5731–5743, <https://doi.org/10.7150/thno.28782>.
- [34] D. Qin, L. Zhang, N. Chang, P. Ni, Y. Zong, A. Bouakaz, M. Wan, Y. Feng, In situ observation of single cell response to acoustic droplet vaporization: membrane deformation, permeabilization, and blebbing, 47 (2018) 141–150, <https://doi.org/10.1016/j.ulsonch.2018.02.004>.
- [35] X. Zhou, L. Guo, D. Shi, D. Meng, X. Sun, M. Shang, X. Liu, Y. Zhao, J. Li, Ultrasound-responsive highly biocompatible nanodroplets loaded with doxorubicin for tumor imaging and treatment in vivo, 27 (1) (2020) 469–481, <https://doi.org/10.1080/10717544.2020.1739170>.
- [36] H. Lea-Banks, Y. Meng, S.-K. Wu, R. Belhadjhamida, C. Hamani, K. Hynynen, Ultrasound-sensitive nanodroplets achieve targeted neuromodulation, 332 (2021) 30–39, <https://doi.org/10.1016/j.jconrel.2021.02.010>.
- [37] J.N. Harmon, F. Kabinejadian, R. Seda, M.L. Fabiilli, S. Kuruvilla, C.C. Kuo, J.M. Greve, J.B. Fowlkes, J.L. Bull, Minimally invasive gas embolization using acoustic droplet vaporization in a rodent model of hepatocellular carcinoma, 9 (1) (2019) 11040, <https://doi.org/10.1038/s41598-019-47309-y>.
- [38] D.L. Miller, J. Song, Lithotripter shock waves with cavitation nucleation agents produce tumor growth reduction and gene transfer, in vivo, 28 (10) (2002) 1343–1348, [https://doi.org/10.1016/S0301-5629\(02\)00572-0](https://doi.org/10.1016/S0301-5629(02)00572-0).
- [39] E. Vlaisavljevich, O. Aydin, Y. Yuksel Durmaz, K.-W. Lin, B. Fowlkes, M. ElSayed, Z. Xu, Effects of ultrasound frequency on nanodroplet-mediated histotripsy, 41 (8) (2015) 2135–2147, <https://doi.org/10.1016/j.ultrasmedbio.2015.04.007>.
- [40] M. Zhang, M.L. Fabiilli, K.J. Haworth, F. Padilla, S.D. Swanson, O.D. Kripfgans, P.L. Carson, J.B. Fowlkes, Acoustic droplet vaporization for enhancement of thermal ablation by high intensity focused ultrasound, 18 (9) (2011) 1123–1132, <https://doi.org/10.1016/j.acra.2011.04.012>.
- [41] C.C. Chen, P.S. Sheeran, S.-Y. Wu, O.O. Olumolade, P.A. Dayton, E.E. Konofagou, Targeted drug delivery with focused ultrasound-induced blood-brain barrier opening using acoustically-activated nanodroplets, 172 (3) (2013) 795–804, <https://doi.org/10.1016/j.jconrel.2013.09.025>.
- [42] G. Lajoinie, E. Gelderblom, C. Chlon, M. Böhmer, W. Steenbergen, N. De Jong, S. Manohar, M. Versluis, Ultrafast vapourization dynamics of laser-activated polymeric microcapsules, 5 (1) (2014) 3671, <https://doi.org/10.1038/ncomms4671>.
- [43] Y. Zhou, R. Wang, Z. Teng, Z. Wang, B. Hu, M. Kolios, H. Chen, N. Zhang, Y. Wang, P. Li, X. Wu, G. Lu, Y. Chen, Y. Zheng, Magnetic nanoparticle-promoted droplet vaporization for in vivo stimuli-responsive cancer theranostics, 8 (9) (2016) e313, <https://doi.org/10.1038/am.2016.146>.
- [44] J. Xu, Y. Chen, L. Deng, J. Liu, Y. Cao, P. Li, H. Ran, Y. Zheng, Z. Wang, Microwave-activated nanodroplet vaporization for highly efficient tumor ablation with real-time monitoring performance, 106 (2016) 264–275, <https://doi.org/10.1016/j.biomaterials.2016.08.034>.
- [45] W.-W. Liu, S.-H. Huang, P.-C. Li, Synchronized optical and acoustic droplet vaporization for effective sonoporation, 11 (6) (2019) 279, <https://doi.org/10.3390/pharmaceutics11060279>.
- [46] M.A. Borden, G. Shakya, A. Upadhyay, K.-H. Song, Acoustic nanodrops for biomedical applications, 50 (2020) 101383, <https://doi.org/10.1016/j.cocis.2020.08.008>.
- [47] H. Lea-Banks, M. O’Reilly, K. Hynynen, Ultrasound-responsive droplets for therapy: a review, 293 (2019) 144–154, <https://doi.org/10.1016/j.jconrel.2018.11.028>.
- [48] H. Maeda, H. Nakamura, J. Fang, The EPR effect for macromolecular drug delivery to solid tumors: improvement of tumor uptake, lowering of systemic toxicity, and distinct tumor imaging in vivo, 65 (1) (2013) 71–79, <https://doi.org/10.1016/j.addr.2012.10.002>.
- [49] M.T. Burgess, T.M. Porter, On-demand cavitation from bursting droplets, 11 (4) (2015).
- [50] J.J. Kwan, R. Myers, C.M. Coviello, S.M. Graham, A.R. Shah, E. Stride, R.C. Carlisle, C.C. Coussios, Ultrasound-propelled nanocapsules for drug delivery, 11 (39) (2015) 5305–5314, <https://doi.org/10.1002/sml.201501322>.
- [51] C. Mannaris, B.M. Teo, A. Seth, L. Bau, C. Coussios, E. Stride, Gas-stabilizing gold nanocones for acoustically mediated drug delivery, 7 (12) (2018) 1800184, <https://doi.org/10.1002/adhm.201800184>.
- [52] A. Yildirim, R. Chattaraj, N.T. Blum, G.M. Goldscheiter, A.P. Goodwin, Stable encapsulation of air in mesoporous silica nanoparticles: fluorocarbon-free nanoscale contrast agents, 5 (11) (2016) 1290–1298, <https://doi.org/10.1002/adhm.201600030>.
- [53] P. Frinking, T. Segers, Y. Luan, F. Tranquart, Three decades of ultrasound contrast agents: a review of the past, present and future improvements, 46 (4) (2020) 892–908, <https://doi.org/10.1016/j.ultrasmedbio.2019.12.008>.
- [54] Z. Liang, H. Chen, X. Gong, B. Shi, L. Lin, F. Tao, Q. Wu, M. Fang, H. Li, C. Lu, H. Xu, Y. Zhao, B. Chen, Ultrasound-induced destruction of nitric oxide-loaded

- microbubbles in the treatment of thrombus and ischemia-reperfusion injury, 12 (2022) 745693, <https://doi.org/10.3389/fphar.2021.745693>.
- [55] J. Sutton, J. Raymond, M. Verleye, G. Pyne-Geithman, C. Holland, Pulsed ultrasound enhances the delivery of nitric oxide from bubble liposomes to ex vivo porcine carotid tissue, 9 (2014) 4671–4683, <https://doi.org/10.2147/IJN.S63850>.
- [56] A. Drzał, A. Delalande, G. Dziurman, M. Fournié, C. Pichon, M. Elas, Increasing oxygen tension in tumor tissue using ultrasound sensitive o₂ microbubbles, 193 (2022) 567–578, <https://doi.org/10.1016/j.freeradbiomed.2022.11.005>.
- [57] C. McEwan, J. Owen, E. Stride, C. Fowley, H. Nesbitt, D. Cochrane, C. Coussios, M. Borden, N. Nomikou, A.P. McHale, J.F. Callan, Oxygen carrying microbubbles for enhanced sonodynamic therapy of hypoxic tumours, 203 (2015) 51–56, <https://doi.org/10.1016/j.jconrel.2015.02.004>.
- [58] Y. He, B. Zhang, Y. Chen, Q. Jin, J. Wu, F. Yan, H. Zheng, Image-guided hydrogen gas delivery for protection from myocardial ischemia-reperfusion injury via microbubbles, 9 (25) (2017) 21190–21199, <https://doi.org/10.1021/acsami.7b05346>.
- [59] S. Eggen, S.-M. Fagerland, Y. Morch, R. Hansen, K. Sovik, S. Berg, H. Furu, A.D. Bohn, M.B. Lilledahl, A. Angelsen, B. Angelsen, C. De Lange Davies, Ultrasound-enhanced drug delivery in prostate cancer xenografts by nanoparticles stabilizing microbubbles, 187 (2014) 39–49, <https://doi.org/10.1016/j.jconrel.2014.05.020>.
- [60] A.J. Dixon, J. Li, J.-M.R. Rickel, A.L. Klibanov, Z. Zuo, J.A. Hossack, Efficacy of sonothrombolysis using microbubbles produced by a catheter-based microfluidic device in a rat model of ischemic stroke, 47 (4) (2019) 1012–1022, <https://doi.org/10.1007/s10439-019-02209-0>.
- [61] P.G. Rudakovskaya, R.A. Barmin, P.S. Kuzmin, E.P. Fedotkina, A.N. Sencha, D.A. Gorin, Microbubbles stabilized by protein shell: from pioneering ultrasound contrast agents to advanced theranostic systems, 14 (6) (2022) 1236, <https://doi.org/10.3390/pharmaceutics14061236>.
- [62] J.A. Feshitan, C.C. Chen, J.J. Kwan, M.A. Borden, Microbubble size isolation by differential centrifugation, 329 (2) (2009) 316–324, <https://doi.org/10.1016/j.jcis.2008.09.066>.
- [63] K. Wei, S.L. Mulvagh, L. Carson, R. Davidoff, R. Gabriel, R.A. Grimm, S. Wilson, L. Fane, C.A. Herzog, W.A. Zoghbi, R. Taylor, M. Farrar, F.A. Chaudhry, T.R. Porter, W. Irani, R.M. Lang, The safety of definity and optison for ultrasound image enhancement: a retrospective analysis of 78,383 administered contrast doses, 21 (11) (2008) 1202–1206, <https://doi.org/10.1016/j.echo.2008.07.019>.
- [64] K. Wei, S. Shah, W.A. Jaber, A. DeMaria, An observational study of the occurrence of serious adverse reactions among patients who receive optison in routine medical practice, 27 (9) (2014) 1006–1010, <https://doi.org/10.1016/j.echo.2014.04.020>.
- [65] Y.-H. Chou, J.-D. Liang, S.-Y. Wang, S.-J. Hsu, J.-T. Hu, S.-S. Yang, H.-K. Wang, T.-Y. Lee, C.-M. Tiu, Safety of perfluorobutane (sonazoid) in characterizing focal liver lesions, 27 (2) (2019) 81.
- [66] N. C. for Biotechnology Information, Compound summary for CID 17358, sulfur hexafluoride.
- [67] M.P. Krafft, J.G. Riess, *Perfluorochemical-based oxygen therapeutics, contrast agents, and beyond*, in: *Fluorine and Health*, Elsevier, 2008, pp. 447–486.
- [68] J. Jägers, A. Wrobeln, K.B. Ferenz, Perfluorocarbon-based oxygen carriers: from physics to physiology, 473 (2) (2021) 139–150, <https://doi.org/10.1007/s00424-020-02482-2>.
- [69] M. Aliabouzar, O.D. Kripfgans, J. Brian Fowlkes, M.L. Fabiilli, Bubble nucleation and dynamics in acoustic droplet vaporization: a review of concepts, applications, and new directions, <https://doi.org/10.1016/j.zemedi.2023.01.004>, 2023, S0939388923000041.
- [70] N. Reznik, M. Seo, R. Williams, E. Bolewska-Pedyczak, M. Lee, N. Matsuura, J. Garipey, F.S. Foster, P.N. Burns, Optical studies of vaporization and stability of fluorescently labelled perfluorocarbon droplets, 57 (21) (2012) 7205–7217, <https://doi.org/10.1088/0031-9155/57/21/7205>.
- [71] N.Y. Rapoport, A.M. Kennedy, J.E. Shea, C.L. Scaife, K.-H. Nam, Controlled and targeted tumor chemotherapy by ultrasound-activated nanoemulsions/microbubbles, 138 (3) (2009) 268–276, <https://doi.org/10.1016/j.jconrel.2009.05.026>.
- [72] P.E. Alcaraz, S.J. Davidson, E. Shreeve, R. Meuschke, M. Romanowski, R.S. Witte, T.R. Porter, T.O. Matsunaga, Thermal and acoustic stabilization of volatile phase-change contrast agents via layer-by-layer assembly, 49 (5) (2023) 1058–1069, <https://doi.org/10.1016/j.ultrasmedbio.2022.12.002>.
- [73] M. Ghorbani, K. Olofsson, J.-W. Benjamins, K. Loskutova, T. Paulraj, M. Wiklund, D. Grishenkov, A.J. Svagan, Unravelling the acoustic and thermal responses of perfluorocarbon liquid droplets stabilized with cellulose nanofibers, 35 (40) (2019) 13090–13099, <https://doi.org/10.1021/acs.langmuir.9b02132>.
- [74] R. Melich, P. Bussat, L. Morici, A. Vivien, E. Gaud, T. Bettinger, S. Cherkaoui, Microfluidic preparation of various perfluorocarbon nanodroplets: characterization and determination of acoustic droplet vaporization (ADV) threshold, 587 (2020) 119651, <https://doi.org/10.1016/j.ijpharm.2020.119651>.
- [75] O.D. Kripfgans, J. Fowlkes, D.L. Miller, O. Eldevik, P.L. Carson, Acoustic droplet vaporization for therapeutic and diagnostic applications, 26 (7) (2000) 1177–1189, [https://doi.org/10.1016/S0301-5629\(00\)00262-3](https://doi.org/10.1016/S0301-5629(00)00262-3).
- [76] R. Williams, C. Wright, E. Cherin, N. Reznik, M. Lee, I. Gorelikov, F.S. Foster, N. Matsuura, P.N. Burns, Characterization of submicron phase-change perfluorocarbon droplets for extravascular ultrasound imaging of cancer, 39 (3) (2013) 475–489, <https://doi.org/10.1016/j.ultrasmedbio.2012.10.004>.
- [77] S. Cleve, A. Lassus, C. Diddens, B. Van Elburg, E. Gaud, S. Cherkaoui, M. Versluis, T. Segers, G. Lajoinie, Microbubble formation by flow focusing: role of gas and liquid properties, and channel geometry, 972 (2023) A27, <https://doi.org/10.1017/jfm.2023.704>.
- [78] T.D. Martz, P.S. Sheeran, D. Bardin, A.P. Lee, P.A. Dayton, Precision manufacture of phase-change perfluorocarbon droplets using microfluidics, 37 (11) (2011) 1952–1957, <https://doi.org/10.1016/j.ultrasmedbio.2011.08.012>.
- [79] R. Melich, J.-P. Valour, S. Urbaniak, F. Padilla, C. Charcosset, Preparation and characterization of perfluorocarbon microbubbles using shirasu porous glass (SPG) membranes, 560 (2019) 233–243, <https://doi.org/10.1016/j.colsurfa.2018.09.058>.
- [80] R. Melich, A. Zorgani, F. Padilla, C. Charcosset, Preparation of perfluorocarbon emulsions by premix membrane emulsification for acoustic droplet vaporization (ADV) in biomedical applications, 22 (3) (2020) 62, <https://doi.org/10.1007/s10544-020-00504-5>.
- [81] P.S. Sheeran, S. Luois, P.A. Dayton, T.O. Matsunaga, Formulation and acoustic studies of a new phase-shift agent for diagnostic and therapeutic ultrasound, 27 (17) (2011) 10412–10420, <https://doi.org/10.1021/la2013705>.
- [82] E. Stride, T. Segers, G. Lajoinie, S. Cherkaoui, T. Bettinger, M. Versluis, M. Borden, Microbubble agents: new directions, 46 (6) (2020) 1326–1343, <https://doi.org/10.1016/j.ultrasmedbio.2020.01.027>.
- [83] M. Späth, M. Hohmann, M. Rohde, B. Lengenfelder, F. Stelze, F. Klämpfl, Determination of the diameter of simulated human capillaries using shifted position-diffuse reflectance imaging, 14 (4) (2021) e202000465, <https://doi.org/10.1002/jbio.202000465>.
- [84] A.A. Exner, M.C. Kolios, Bursting microbubbles: how nanobubble contrast agents can enable the future of medical ultrasound molecular imaging and image-guided therapy, 54 (2021) 101463, <https://doi.org/10.1016/j.cocis.2021.101463>.
- [85] J.Z. Myers, J.A. Navarro-Becerra, M.A. Borden, Nanobubbles are non-echogenic for fundamental-mode contrast-enhanced ultrasound imaging, 33 (6) (2022) 1106–1113, <https://doi.org/10.1021/acs.bioconjchem.2c00155>.
- [86] J.J. Choi, J.A. Feshitan, B. Baseri, S. Wang, Y.-S. Tung, M.A. Borden, E.E. Konofagou, Microbubble-size dependence of focused ultrasound-induced blood-brain barrier opening in mice in vivo, 57 (1) (2010) 145–154, <https://doi.org/10.1109/TBME.2009.2034533>.
- [87] D.R. Evans, D.F. Parsons, V.S.J. Craig, Physical properties of phase-change emulsions, 22 (23) (2006) 9538–9545, <https://doi.org/10.1021/la062097u>.
- [88] P.S. Sheeran, T.O. Matsunaga, P.A. Dayton, Phase-transition thresholds and vaporization phenomena for ultrasound phase-change nanoemulsions assessed via high-speed optical microscopy, 58 (13) (2013) 4513–4534, <https://doi.org/10.1088/0031-9155/58/13/4513>.
- [89] O. Shpak, L. Stricker, M. Versluis, D. Lohse, The role of gas in ultrasonically driven vapor bubble growth, 58 (8) (2013) 2523–2535, <https://doi.org/10.1088/0031-9155/58/8/2523>.
- [90] G. Lajoinie, T. Segers, M. Versluis, High-frequency acoustic droplet vaporization is initiated by resonance, 126 (3) (2021) 034501, <https://doi.org/10.1103/PhysRevLett.126.034501>.
- [91] H. Mulvana, R.J. Browning, Y. Luan, N. de Jong, M.-X. Tang, R.J. Eckersley, E. Stride, Characterization of contrast agent microbubbles for ultrasound imaging and therapy research, in: *IEEE Transactions on Ultrasonics, Ferroelectrics, and Frequency Control* 64 (1) (2017) 232–251, <https://doi.org/10.1109/TUFFC.2016.2613991>.
- [92] S.V. Morse, A. Mishra, T.G. Chan, R.T.M. de Rosales, J.J. Choi, Liposome delivery to the brain with rapid short-pulses of focused ultrasound and microbubbles, 341 (2022) 605–615, <https://doi.org/10.1016/j.jconrel.2021.12.005>.
- [93] S.R. Sirsi, C. Fung, S. Garg, M.Y. Tianning, P.A. Mountford, M.A. Borden, Lung surfactant microbubbles increase lipophilic drug payload for ultrasound-targeted delivery, 3 (6) (2013) 409–419, <https://doi.org/10.7150/thno.5616>.
- [94] M. Bezagu, J. Clarhaut, B. Renoux, F. Monti, M. Tanter, P. Tabeling, J. Cossy, O. Couture, S. Papot, S. Arseniyadis, In situ targeted activation of an anticancer agent using ultrasound-triggered release of composite droplets, 142 (2017) 2–7, <https://doi.org/10.1016/j.ejmech.2017.03.057>.
- [95] Y. Zhou, Application of acoustic droplet vaporization in ultrasound therapy, 3 (1) (2015) 20, <https://doi.org/10.1186/s40349-015-0041-8>.
- [96] Q. Jin, Z. Wang, F. Yan, Z. Deng, F. Ni, J. Wu, R. Shandas, X. Liu, H. Zheng, A novel cationic microbubble coated with stearic acid-modified polyethylenimine to enhance DNA loading and gene delivery by ultrasound, 8 (9) (2013) e76544, <https://doi.org/10.1371/journal.pone.0076544>.
- [97] L. Zhu, H. Zhao, Z. Zhou, Y. Xia, Z. Wang, H. Ran, P. Li, J. Ren, Peptide-functionalized phase-transformation nanoparticles for low intensity focused ultrasound-assisted tumor imaging and therapy, 18 (3) (2018) 1831–1841, <https://doi.org/10.1021/acs.nanolett.7b05087>.
- [98] I. Beekers, S.A. Langeveld, B. Meijlink, A.F. Van Der Steen, N. De Jong, M.D. Verweij, K. Kooiman, Internalization of targeted microbubbles by endothelial cells and drug delivery by pores and tunnels, 347 (2022) 460–475, <https://doi.org/10.1016/j.jconrel.2022.05.008>.
- [99] J.S.-M. Yeh, C.A. Sennoga, E. McConnell, R. Eckersley, M.-X. Tang, S. Nourshargh, J.M. Seddon, D.O. Haskard, P. Nihoyannopoulos, A targeting microbubble for ultrasound molecular imaging, 10 (7) (2015) e0129681, <https://doi.org/10.1371/journal.pone.0129681>.
- [100] C.J. Slagle, D.H. Thamm, E.K. Randall, M.A. Borden, Click conjugation of cloaked peptide ligands to microbubbles, 29 (5) (2018) 1534–1543, <https://doi.org/10.1021/acs.bioconjchem.8b00084>.

- [101] J.J. Kwan, M.A. Borden, Lipid monolayer dilatational mechanics during microbubble gas exchange, 8 (17) (2012) 4756, <https://doi.org/10.1039/c2sm07437k>.
- [102] T.A. Rovers, G. Sala, E. Van Der Linden, M.B. Meinders, Effect of temperature and pressure on the stability of protein microbubbles, 8 (1) (2016) 333–340, <https://doi.org/10.1021/acsami.5b08527>.
- [103] J.R. Lindner, M.P. Coggins, S. Kaul, A.L. Klibanov, G.H. Brandenburger, K. Ley, Microbubble persistence in the microcirculation during ischemia/reperfusion and inflammation is caused by integrin- and complement-mediated adherence to activated leukocytes, 101 (6) (2000) 668–675, <https://doi.org/10.1161/01.CIR.101.6.668>.
- [104] K. Yanagisawa, F. Moriyasu, T. Miyahara, M. Yuki, H. Iijima, Phagocytosis of ultrasound contrast agent microbubbles by kupffer cells, 33 (2) (2007) 318–325, <https://doi.org/10.1016/j.ultrasmedbio.2006.08.008>.
- [105] M.S. Tartis, D.E. Kruse, H. Zheng, H. Zhang, A. Kheirloomoom, J. Marik, K.W. Ferrara, Dynamic microPET imaging of ultrasound contrast agents and lipid delivery, 131 (3) (2008) 160–166, <https://doi.org/10.1016/j.jconrel.2008.07.030>.
- [106] S.M. Fix, A.G. Nyankima, M.D. McSweeney, J.K. Tsuruta, S.K. Lai, P.A. Dayton, Accelerated clearance of ultrasound contrast agents containing polyethylene glycol is associated with the generation of anti-polyethylene glycol antibodies, 44 (6) (2018) 1266–1280, <https://doi.org/10.1016/j.ultrasmedbio.2018.02.006>.
- [107] E. Stride, C. Coussios, Nucleation, mapping and control of cavitation for drug delivery, 1 (8) (2019) 495–509, <https://doi.org/10.1038/s42254-019-0074-y>.
- [108] S. Garg, A.A. Thomas, M.A. Borden, The effect of lipid monolayer in-plane rigidity on in vivo microbubble circulation persistence, 34 (28) (2013) 6862–6870, <https://doi.org/10.1016/j.biomaterials.2013.05.053>.
- [109] A.S. Abu Lila, H. Kiwada, T. Ishida, The accelerated blood clearance (ABC) phenomenon: clinical challenge and approaches to manage, 172 (1) (2013) 38–47, <https://doi.org/10.1016/j.jconrel.2013.07.026>.
- [110] P.S. Sheeran, J.D. Rojas, C. Puett, J. Hjelmquist, C.B. Arena, P.A. Dayton, Contrast-enhanced ultrasound imaging and in vivo circulatory kinetics with low-boiling-point nanoscale phase-change perfluorocarbon agents, 41 (3) (2015) 814–831, <https://doi.org/10.1016/j.ultrasmedbio.2014.10.020>.
- [111] K.G. Toft, S.O. Hustvedt, P.-A. Hals, I. Oulie, S. Uran, K. Landmark, P.T. Normann, T. Skotland, Disposition of perfluorobutane in rats after intravenous injection of sonazoid™, 32 (1) (2006) 107–114, <https://doi.org/10.1016/j.ultrasmedbio.2005.09.008>.
- [112] S. Kotopoulos, M. Postema, Microfoam formation in a capillary, 50 (2) (2010) 260–268, <https://doi.org/10.1016/j.ultras.2009.09.028>.
- [113] S.L. Mulvagh, H. Rakowski, M.A. Nannan, S.S. Abdelmoneim, H. Becher, S.M. Bierig, P.N. Burns, R. Castello, P.D. Coon, M.E. Hagen, J.G. Jollis, T.R. Kimball, D.W. Kitzman, I. Kronzon, A.J. Labovitz, R.M. Lang, J. Mathew, W.S. Moir, S.F. Nagueh, A.S. Pearlman, J.E. Perez, T.R. Porter, J. Rosenbloom, G.M. Strachan, S. Thanigaraj, K. Wei, A. Woo, E.H. Yu, W.A. Zoghbi, American society of echocardiography consensus statement on the clinical applications of ultrasound contrast agents in echocardiography, 21 (11) (2008) 1179–1201, <https://doi.org/10.1016/j.echo.2008.09.009>.
- [114] M.A. Borden, K.-H. Song, Reverse engineering the ultrasound contrast agent, 262 (2018) 39–49, <https://doi.org/10.1016/j.jcis.2018.10.004>.
- [115] A.H. Lo, O.D. Kripfgans, P.L. Carson, J.B. Fowlkes, Spatial control of gas bubbles and their effects on acoustic fields, 32 (1) (2006) 95–106, <https://doi.org/10.1016/j.ultrasmedbio.2005.09.009>.
- [116] K.J. Haworth, O.D. Kripfgans, Initial growth and coalescence of acoustically vaporized perfluorocarbon microdroplets, in: 2008 IEEE Ultrasonics Symposium, IEEE, 2008, pp. 623–626.
- [117] S.-T. Kang, C.-K. Yeh, Intracellular acoustic droplet vaporization in a single peritoneal macrophage for drug delivery applications, 27 (21) (2011) 13183–13188, <https://doi.org/10.1021/la203212p>.
- [118] O. Kripfgans, J. Fowlkes, M. Woydt, O. Eldevik, P. Carson, In vivo droplet vaporization for occlusion therapy and phase aberration correction, 49 (6) (2002) 726–738, <https://doi.org/10.1109/TUFFC.2002.1009331>.
- [119] B.L. Helfield, K. Yoo, J. Liu, R. Williams, P.S. Sheeran, D.E. Goertz, P.N. Burns, Investigating the accumulation of submicron phase-change droplets in tumors, 46 (10) (2020) 2861–2870, <https://doi.org/10.1016/j.ultrasmedbio.2020.06.021>.
- [120] S.K. Golombek, J.-N. May, B. Theek, L. Appold, N. Drude, F. Kiessling, T. Lammer, Tumor targeting via EPR: strategies to enhance patient responses, 130 (2018) 17–38, <https://doi.org/10.1016/j.addr.2018.07.007>.
- [121] C. Chin, C. Lancée, J. Borsboom, F. Mastik, M. Frijlink, N. De Jong, M. Versluis, D. Lohse, Brandaris 128: a digital 25 million frames per second camera with 128 highly sensitive frames, 74 (12) (2003) 5026–5034, <https://doi.org/10.1063/1.1626013>.
- [122] M. Cattaneo, O. Supponen, Shell viscosity estimation of lipid-coated microbubbles, 19 (2023) 5925–5941, <https://doi.org/10.1039/D3SM00871A>.
- [123] L. Rayleigh, VII. On the pressure developed in a liquid during the collapse of a spherical cavity, 34 (1941) 94–98, <https://doi.org/10.1080/14786440808635681>.
- [124] M.S. Plesset, The dynamics of cavitation bubbles, 16 (3) (2021) 277–282, <https://doi.org/10.1115/1.4009975>.
- [125] B.E. Noltingk, E.A. Neppiras, Cavitation produced by ultrasonics, 63 (9) (1950) 674, <https://doi.org/10.1088/0370-1301/63/9/305>.
- [126] E.A. Neppiras, B.E. Noltingk, Cavitation produced by ultrasonics: theoretical conditions for the onset of cavitation 64, 12 (1951) 1032, <https://doi.org/10.1088/0370-1301/64/12/302>.
- [127] H. Poritsky, The collapse or growth of a spherical bubble or cavity in a viscous fluid, 1952, pp. 813–821.
- [128] M. Brenner, S. Hilgenfeldt, D. Lohse, Single-bubble sonoluminescence, 74 (2) (2002) 425–484, <https://doi.org/10.1103/RevModPhys.74.425>.
- [129] A. Prosperetti, L. Crum, K. Commander, Nonlinear bubble dynamics, 83 (2) (1988) 502–514, <https://doi.org/10.1121/1.396145>.
- [130] D. Chatterjee, K. Sarker, A Newtonian rheological model for the interface of microbubble contrast agents, 29 (12) (2003) 1749–1757, [https://doi.org/10.1016/S0301-5629\(03\)01051-2](https://doi.org/10.1016/S0301-5629(03)01051-2).
- [131] N. Jaensson, P. Anderson, J. Vermant, Computational interfacial rheology, 290 (2021) 104507, <https://doi.org/10.1016/j.jnnfm.2021.104507>.
- [132] P. Marmottant, S. van der Meer, M. Emmer, M. Versluis, N. de Jong, S. Hilgenfeldt, D. Lohse, A model for large amplitude oscillations of coated bubbles accounting for buckling and rupture, 118 (6) (2005) 3499–3505, <https://doi.org/10.1121/1.2109427>.
- [133] E. Hermans, J. Vermant, Interfacial shear rheology of DPPC under physiologically relevant conditions, 10 (1) (2014) 175–186, <https://doi.org/10.1039/c3sm52091a>.
- [134] B. Dollet, P. Marmottant, V. Garbin, Bubble dynamics in soft and biological matter, 51 (2019) 331–355, <https://doi.org/10.1146/annurev-fluid-010518-040352>.
- [135] M. Versluis, E. Stride, G. Lajoinie, B. Dollet, T. Segers, Ultrasound contrast agent modeling: a review, 46 (9) (2020) 2117–2144.
- [136] T. Leighton, The Acoustic Bubble, Academic Press, 1994.
- [137] M. Borden, G. Martinez, J. Ricker, N. Tsvetkova, M. Longo, R. Gillies, P. Dayton, K. Ferrara, Lateral phase separation in lipid-coated microbubbles, 22 (9) (2006) 4291–4297, <https://doi.org/10.1021/la052841v>.
- [138] V. Daeichin, M. Inzunza-Ibarra, J. Lum, M. Borden, T. Murray, Photoacoustic impulse response of lipid-coated ultrasound contrast agents, 68 (6) (2021) 2311–2314, <https://doi.org/10.1109/TUFFC.2021.3052140>.
- [139] J.S. Lum, D.M. Stobbe, M.A. Borden, T.W. Murray, Photoacoustic technique to measure temperature effects on microbubble viscoelastic properties, 112 (11) (2018), <https://doi.org/10.1063/1.5005548>.
- [140] H. Mulvana, E. Stride, M. Tang, J.V. Hajnal, R. Eckersley, Temperature-dependent differences in the nonlinear acoustic behavior of ultrasound contrast agents revealed by high-speed imaging and bulk acoustics, 37 (9) (2011) 1509–1517, <https://doi.org/10.1016/j.ultrasmedbio.2011.05.020>.
- [141] P. Duncan, D. Needham, Test of the Epstein-plesset model for gas microparticle dissolution in aqueous media: effect of surface tension and gas undersaturation in solution, 20 (7) (2004) 2567–2578, <https://doi.org/10.1021/la034930i>.
- [142] H. Oguz, A. Prosperetti, The natural frequency of oscillation of gas bubbles in tubes, 103 (6) (1998) 3301–3308, <https://doi.org/10.1121/1.423043>.
- [143] S. Qin, K. Ferrara, Acoustic response of compliant microvessels containing ultrasound contrast agents, 51 (20) (2006) 5065–5088, <https://doi.org/10.1088/0031-9155/51/20/001>.
- [144] S. Qin, K. Ferrara, The natural frequency of nonlinear oscillation of ultrasound contrast agents in microvessels, 33 (7) (2007) 1140–1148, <https://doi.org/10.1016/j.ultrasmedbio.2006.12.009>.
- [145] C.F. Caskey, S.M. Stieger, S. Qin, P.A. Dayton, K.W. Ferrara, Direct observations of ultrasound microbubble contrast agent interaction with the microvessel wall, 122 (2) (2007) 1191–1200, <https://doi.org/10.1121/1.2747204>.
- [146] Y. Luan, G. Lajoinie, E. Gelderblom, I. Skachkov, A. van der Steen, H. Vos, M. Versluis, N. De Jong, Lipid shedding from single oscillating microbubbles, 40 (8) (2014) 1834–1846, <https://doi.org/10.1016/j.ultrasmedbio.2014.02.031>.
- [147] M. Versluis, High-speed imaging in fluids, 54 (2) (2013), <https://doi.org/10.1007/s00348-013-1458-x>.
- [148] M. Borden, D. Kruse, C. Caskey, S. Zhao, P. Dayton, K. Ferrara, Influence of lipid shell physicochemical properties on ultrasound-induced microbubble destruction, 52 (11) (2005) 1992–2002, <https://doi.org/10.1109/TUFFC.2005.1561668>.
- [149] J.-P. O'Brien, E. Stride, N. Ovenden, Surfactant shedding and gas diffusion during pulsed ultrasound through a microbubble contrast agent suspension, 134 (2) (2013) 1416–1427, <https://doi.org/10.1121/1.4812860>.
- [150] R. Apfel, C. Holland, Gauging the likelihood of cavitation from short-pulse, low-duty cycle diagnostic ultrasound, 17 (2) (1991) 179–185, [https://doi.org/10.1016/0301-5629\(91\)90125-G](https://doi.org/10.1016/0301-5629(91)90125-G).
- [151] C. Church, Frequency, pulse length, and the mechanical index, 6 (3) (2005) 162–168, <https://doi.org/10.1121/1.1901757>.
- [152] H. Flynn, Cavitation dynamics. II. Free pulsations and models for cavitation bubbles, 58 (6) (1975) 1160–1170, <https://doi.org/10.1121/1.380799>.
- [153] S. Stieger, C. Caskey, R. Adamson, S. Qin, F.-R. Curry, E. Wisner, K. Ferrara, Enhancement of vascular permeability with low-frequency contrast-enhanced ultrasound in the choroidal membrane model, 243 (1) (2007) 112–121, <https://doi.org/10.1148/radiol.2431060167>.
- [154] D. Miller, C. Dou, R. Wiggins, Frequency dependence of kidney injury induced by contrast-aided diagnostic ultrasound in rats, 34 (10) (2008) 1678–1687.
- [155] R. Jones, D. McMahon, K. Hynynen, Ultrafast three-dimensional microbubble imaging in vivo predicts tissue damage volume distributions during nonthermal brain ablation, 10 (16) (2020) 7211–7230, <https://doi.org/10.7150/thno.47281>.
- [156] W.-S. Chen, A. Brayman, T. Matula, L. Crum, Inertial cavitation dose and hemolysis produced in vitro with or without optison®, 29 (5) (2003) 725–737, [https://doi.org/10.1016/S0301-5629\(03\)00013-9](https://doi.org/10.1016/S0301-5629(03)00013-9).

- [157] J. Hwang, J. Tu, A. Brayman, T. Matula, L. Crum, Correlation between inertial cavitation dose and endothelial cell damage in vivo, 32 (10) (2006) 1611–1619, <https://doi.org/10.1016/j.ultrasmedbio.2006.07.016>.
- [158] Y. Yang, X. Zhang, D. Ye, R. Laforest, J. Williamson, Y. Liu, H. Chen, Cavitation dose painting for focused ultrasound-induced blood-brain barrier disruption, 9 (1) (2019), <https://doi.org/10.1038/s41598-019-39090-9>.
- [159] C. Smith, C. Coussios, Spatiotemporal assessment of the cellular safety of cavitation-based therapies by passive acoustic mapping, 46 (5) (2020) 1235–1243, <https://doi.org/10.1016/j.ultrasmedbio.2020.01.009>.
- [160] L. Somaglino, G. Bouchoux, J.-L. Mestas, C. Lafon, Validation of an acoustic cavitation dose with hydroxyl radical production generated by inertial cavitation in pulsed mode: application to in vitro drug release from liposomes, 18 (2) (2011) 577–588, <https://doi.org/10.1016/j.ultronch.2010.07.009>.
- [161] M. Aliabouzar, K.N. Kumar, K. Sarkar, Effects of droplet size and perfluorocarbon boiling point on the frequency dependence of acoustic vaporization threshold, 145 (2) (2019) 1105–1116, <https://doi.org/10.1121/1.5091781>.
- [162] M. Aliabouzar, O.D. Kripfgans, W.Y. Wang, B.M. Baker, J. Brian Fowlkes, M.L. Fabiilli, Stable and transient bubble formation in acoustically-responsive scaffolds by acoustic droplet vaporization: theory and application in sequential release, 72 (2021) 105430, <https://doi.org/10.1016/j.ultronch.2020.105430>.
- [163] P.A. Mountford, M.A. Borden, On the thermodynamics and kinetics of superheated fluorocarbon phase-change agents, 237 (2016) 15–27, <https://doi.org/10.1016/j.cis.2016.08.007>.
- [164] D. Qin, Q. Zou, S. Lei, W. Wang, Z. Li, Predicting initial nucleation events occurred in a metastable nanodroplet during acoustic droplet vaporization, 75 (2021) 105608, <https://doi.org/10.1016/j.ultronch.2021.105608>.
- [165] O.D. Kripfgans, M.L. Fabiilli, P.L. Carson, J.B. Fowlkes, On the acoustic vaporization of micrometer-sized droplets, 116 (1) (2004) 272–281, <https://doi.org/10.1121/1.1755236>.
- [166] O. Shpak, T.J.A. Kokhuis, Y. Luan, D. Lohse, N. De Jong, B. Fowlkes, M. Fabiilli, M. Versluis, Ultrafast dynamics of the acoustic vaporization of phase-change microdroplets, 134 (2) (2013) 1610–1621, <https://doi.org/10.1121/1.4812882>.
- [167] O. Shpak, M. Verweij, H.J. Vos, N. De Jong, D. Lohse, M. Versluis, Acoustic droplet vaporization is initiated by superharmonic focusing, 111 (5) (2014) 1697–1702, <https://doi.org/10.1073/pnas.1312171111>.
- [168] D.S. Li, O.D. Kripfgans, M.L. Fabiilli, J. Brian Fowlkes, J.L. Bull, Initial nucleation site formation due to acoustic droplet vaporization, 104 (6) (2014) 063703, <https://doi.org/10.1063/1.4864110>.
- [169] S. Fiorini, A. Prasanna, G. Shakya, O. Supponen, M. Cattaneo, Acoustic droplet vaporization of microdroplets, 2022.
- [170] Q. Wu, C. Mannaris, J.P. May, L. Bau, A. Polydorou, S. Ferri, D. Carugo, N.D. Evans, E. Stride, Investigation of the acoustic vaporization threshold of lipid-coated perfluorobutane nanodroplets using both high-speed optical imaging and acoustic methods, 47 (7) (2021) 1826–1843, <https://doi.org/10.1016/j.ultrasmedbio.2021.02.019>.
- [171] M. Aliabouzar, K.N. Kumar, K. Sarkar, Acoustic vaporization threshold of lipid-coated perfluoropentane droplets, 143 (4) (2018) 2001–2012, <https://doi.org/10.1121/1.5027817>.
- [172] M.L. Fabiilli, K.J. Haworth, N.H. Fakhri, O.D. Kripfgans, J.B. Fowlkes, The role of inertial cavitation in acoustic droplet vaporization, 56 (6) (2009), <https://doi.org/10.1109/TUFFC.2009.1132>.
- [173] A. Lo, O. Kripfgans, P. Carson, E. Rothman, J. Fowlkes, Acoustic droplet vaporization threshold: effects of pulse duration and contrast agent, 54 (5) (2007) 933–946, <https://doi.org/10.1109/TUFFC.2007.339>.
- [174] T.L. Szabo, F. Clougherty, C. Grossman, Effects on nonlinearity on the estimation of in situ values of acoustic output parameters, 18 (1) (1999) 33–41, <https://doi.org/10.7863/jum.1999.18.1.33>.
- [175] C.J. Miles, C.R. Doering, O.D. Kripfgans, Nucleation pressure threshold in acoustic droplet vaporization, 120 (3) (2016) 034903, <https://doi.org/10.1063/1.4958907>.
- [176] J.D. Rojas, M.A. Borden, P.A. Dayton, Effect of hydrostatic pressure, boundary constraints and viscosity on the vaporization threshold of low-boiling-point phase-change contrast agents, 45 (4) (2019) 968–979, <https://doi.org/10.1016/j.ultrasmedbio.2018.11.006>.
- [177] A.E. Saunders, Heating of bone and soft tissue by ultrasound, 55 (1) (2007) 52–56, <https://doi.org/10.1179/174313107X160024>.
- [178] S.-T. Kang, Y.-L. Huang, C.-K. Yeh, Characterization of acoustic droplet vaporization for control of bubble generation under flow conditions, 40 (3) (2014) 551–561, <https://doi.org/10.1016/j.ultrasmedbio.2013.10.020>.
- [179] S. Lin, G. Zhang, C.H. Leow, M.-X. Tang, Effects of microchannel confinement on acoustic vaporisation of ultrasound phase change contrast agents, 62 (17) (2017) 6884–6898, <https://doi.org/10.1088/1361-6560/aa8076>.
- [180] K. Loskutova, D. Grishenkov, M. Ghorbani, Review on acoustic droplet vaporization in ultrasound diagnostics and therapeutics, 2019 (2019) 1–20, <https://doi.org/10.1155/2019/9480193>.
- [181] G. Shakya, S.E. Hoff, S. Wang, H. Heinz, X. Ding, M.A. Borden, Vaporizable endoskeletal droplets via tunable interfacial melting transitions, 6 (14) (2020) eaaz7188, <https://doi.org/10.1126/sciadv.aaz7188>.
- [182] S. Guo, A. Shi, S. Xu, X. Du, X. Wang, Y. Zong, A. Bouakaz, M. Wan, Lowering of acoustic droplet vaporization threshold via aggregation, 111 (25) (2017) 254102, <https://doi.org/10.1063/1.5005957>.
- [183] S. Guo, X. Guo, X. Wang, X. Du, P. Wu, A. Bouakaz, M. Wan, Manipulation of nanodroplets via a nonuniform focused acoustic vortex, 13 (3) (2020) 034009, <https://doi.org/10.1103/PhysRevApplied.13.034009>.
- [184] Y. Zhao, D. Qin, J. Chen, J. Hou, T. Ilovitsh, M. Wan, L. Wu, Y. Feng, On-demand regulation and enhancement of the nucleation in acoustic droplet vaporization using dual-frequency focused ultrasound, 90 (2022) 106224, <https://doi.org/10.1016/j.ultronch.2022.106224>.
- [185] J. Chen, Z. Nan, Y. Zhao, L. Zhang, H. Zhu, D. Wu, Y. Zong, M. Lu, T. Ilovitsh, M. Wan, K. Yan, Y. Feng, Enhanced HIFU theranostics with dual-frequency-ring focused ultrasound and activatable perfluoropentane-loaded polymer nanoparticles, 12 (11) (2021) 1324, <https://doi.org/10.3390/mi12111324>.
- [186] P. Sontum, S. Kvåle, A.J. Healey, R. Skurtveit, R. Watanabe, M. Matsumura, J. Østensen, Acoustic cluster therapy (ACT) – a novel concept for ultrasound mediated, targeted drug delivery, 495 (2) (2015) 1019–1027, <https://doi.org/10.1016/j.jipharm.2015.09.047>.
- [187] A. Ishijima, J. Tanaka, T. Azuma, K. Minamihata, S. Yamaguchi, E. Kobayashi, T. Nagamune, I. Sakuma, The lifetime evaluation of vapourised phase-change nanodroplets, 69 (2016) 97–105, <https://doi.org/10.1016/j.ultras.2016.04.002>.
- [188] T. Lacour, T. Valier-Brasier, F. Coulouvrat, Ultimate fate of a dynamical bubble/droplet system following acoustic vaporization, 32 (5) (2020) 051702, <https://doi.org/10.1063/5.0004375>.
- [189] M. Guédra, F. Coulouvrat, A model for acoustic vaporization of encapsulated droplets, 138 (6) (2015) 3656–3667, <https://doi.org/10.1121/1.4937747>.
- [190] T. Lacour, M. Guédra, T. Valier-Brasier, F. Coulouvrat, A model for acoustic vaporization dynamics of a bubble/droplet system encapsulated within a hyperelastic shell, 143 (1) (2018) 23–37, <https://doi.org/10.1121/1.5019467>.
- [191] J. Rooney, Shear as a mechanism for sonically induced biological effects, 52 (6) (1972) 1718–1724, <https://doi.org/10.1121/1.1913306>.
- [192] J.W. Strutt, The Theory of Sound, Cambridge Library Collection - Physical Sciences, Cambridge University Press, 2011.
- [193] W. Nyborg, Acoustic streaming due to attenuated plane waves, 25 (1) (1953) 68–75, <https://doi.org/10.1121/1.1907010>.
- [194] P. Westervelt, The theory of steady rotational flow generated by a sound field, 25 (1) (1953) 60–67, <https://doi.org/10.1121/1.1907009>.
- [195] J. Stuart, Double boundary layers in oscillatory viscous flow, 24 (4) (1966) 673–687, <https://doi.org/10.1017/S0022112066000910>.
- [196] V. Bjerknes, Fields of Force: Supplementary Lectures, Applications to Meteorology; a Course of Lectures in Mathematical Physics Delivered December 1 to 23, 1905, Cornell University Library Historical Math Monographs, Columbia University Press, 1906.
- [197] Y. Huang, F. Hammit, T. Mitchell, Note on shock-wave velocity in high-speed liquid-solid impact, 44 (4) (1973) 1868–1869, <https://doi.org/10.1063/1.1662464>.
- [198] E. Johnsen, T. Colonius, Numerical simulations of non-spherical bubble collapse, 629 (2009) 231–262, <https://doi.org/10.1017/S0022112009006351>.
- [199] P. Prentice, A. Cuschieri, K. Dholakia, M. Prausnitz, P. Campbell, Membrane disruption by optically controlled microbubble cavitation, 1 (2) (2005) 107–110, <https://doi.org/10.1038/nphys148>.
- [200] M. Cattaneo, G. Shakya, O. Supponen, Jetting behaviour of ultrasound-driven microbubbles in contact with a soft substrate, <https://doi.org/10.1109/IUS51837.2023.10306798>, 2023.
- [201] A. Van Wamel, K. Kooiman, M. Hartevelde, M. Emmer, F.J. Ten Cate, M. Versluis, N. De Jong, Vibrating microbubbles poking individual cells: drug transfer into cells via sonoporation, 112 (2) (2006) 149–155, <https://doi.org/10.1016/j.jconrel.2006.02.007>.
- [202] E. Konofagou, Optimization of the ultrasound-induced blood-brain barrier opening, 2 (12) (2012) 1223–1237, <https://doi.org/10.7150/thno.5576>.
- [203] James H. Bezer, Paul Prentice, William Lim Kee Chang, Sophie V. Morse, Kirsten Christensen-Jeffries, Christopher J. Rowlands, Andriy S. Kozlov, James J. Choi, Microbubble dynamics in brain microvessels, 2023.
- [204] B. Helfield, X. Chen, S.C. Watkins, F.S. Villanueva, Biophysical insight into mechanisms of sonoporation, 113 (36) (2016) 9983–9988, <https://doi.org/10.1073/pnas.1606915113>.
- [205] P. Marmottant, S. Hilgenfeldt, Controlled vesicle deformation and lysis by single oscillating bubbles, 423 (6936) (2003) 153–156, <https://doi.org/10.1038/nature01613>.
- [206] Y. Zhou, K. Yang, J. Cui, J. Ye, C. Deng, Controlled permeation of cell membrane by single bubble acoustic cavitation, 157 (1) (2012) 103–111, <https://doi.org/10.1016/j.jconrel.2011.09.068>.
- [207] H. Chen, W. Kreider, A.A. Brayman, M.R. Bailey, T.J. Matula, Blood vessel deformations on microsecond time scales by ultrasonic cavitation, 106 (3) (2011) 034301, <https://doi.org/10.1103/PhysRevLett.106.034301>.
- [208] H. Chen, A.A. Brayman, W. Kreider, M.R. Bailey, T.J. Matula, Observations of translation and jetting of ultrasound-activated microbubbles in mesenteric microvessels, 37 (12) (2011) 2139–2148, <https://doi.org/10.1016/j.ultrasmedbio.2011.09.013>.
- [209] H. Chen, A. Brayman, A. Evan, T. Matula, Preliminary observations on the spatial correlation between short-burst microbubble oscillations and vascular bioeffects, 38 (12) (2012) 2151–2162, <https://doi.org/10.1016/j.ultrasmedbio.2012.08.014>.
- [210] K. Kooiman, M. Foppen-Hartevelde, A.F.V. Der Steen, N. De Jong, Sonoporation of endothelial cells by vibrating targeted microbubbles, 154 (1) (2011) 35–41, <https://doi.org/10.1016/j.jconrel.2011.04.008>.

- [211] I. De Cock, E. Zagato, K. Braeckmans, Y. Luan, N. de Jong, S.C. De Smedt, I. Lentacker, Ultrasound and microbubble mediated drug delivery: acoustic pressure as determinant for uptake via membrane pores or endocytosis, 197 (2015) 20–28, <https://doi.org/10.1016/j.jconrel.2014.10.031>.
- [212] Z. Fan, H. Liu, M. Mayer, C. Deng, Spatiotemporally controlled single cell sonoporation, 109 (41) (2012) 16486–16491, <https://doi.org/10.1073/pnas.1208198109>.
- [213] Z. Fan, D. Chen, C.X. Deng, Characterization of the dynamic activities of a population of microbubbles driven by pulsed ultrasound exposure in sonoporation, 40 (6) (2014) 1260–1272, <https://doi.org/10.1016/j.ultrasmedbio.2013.12.002>.
- [214] M. Ward, J. Wu, J.-F. Chiu, Experimental study of the effects of optison® concentration on sonoporation in vitro, 26 (7) (2000) 1169–1175, [https://doi.org/10.1016/S0301-5629\(00\)00260-X](https://doi.org/10.1016/S0301-5629(00)00260-X).
- [215] P. Qin, L. Xu, T. Han, L. Du, A. Yu, Effect of non-acoustic parameters on heterogeneous sonoporation mediated by single-pulse ultrasound and microbubbles, 31 (2016) 107–115, <https://doi.org/10.1016/j.ulsonch.2015.12.001>.
- [216] M. Shortencarier, P. Dayton, S. Bloch, P. Schumann, T. Matsunaga, G. Ferrara, A method for radiation-force localized drug delivery using gas-filled lipospheres, 51 (7) (2004) 822–831, <https://doi.org/10.1109/TUFFC.2004.1320741>.
- [217] F. Yang, N. Gu, D. Chen, X. Xi, D. Zhang, Y. Li, J. Wu, Experimental study on cell self-sealing during sonoporation, 131 (3) (2008) 205–210, <https://doi.org/10.1016/j.jconrel.2008.07.038>.
- [218] Y. Qiu, Y. Luo, Y. Zhang, W. Cui, D. Zhang, J. Wu, J. Zhang, J. Tu, The correlation between acoustic cavitation and sonoporation involved in ultrasound-mediated DNA transfection with polyethyleneimine (PEI) vitro, 145 (1) (2010) 40–48, <https://doi.org/10.1016/j.jconrel.2010.04.010>.
- [219] N. Kudo, K. Okada, K. Yamamoto, Sonoporation by single-shot pulsed ultrasound with microbubbles adjacent to cells, 96 (12) (2009) 4866–4876, <https://doi.org/10.1016/j.bj.2009.02.072>.
- [220] Y. Zhou, R. Kumon, J. Cui, C. Deng, The size of sonoporation pores on the cell membrane, 35 (10) (2009) 1756–1760, <https://doi.org/10.1016/j.ultrasmedbio.2009.05.012>.
- [221] Y. Hu, J.M. Wan, A.C. Yu, Membrane perforation and recovery dynamics in microbubble-mediated sonoporation, 39 (12) (2013) 2393–2405, <https://doi.org/10.1016/j.ultrasmedbio.2013.08.003>.
- [222] C.X. Deng, F. Sieling, H. Pan, J. Cui, Ultrasound-induced cell membrane porosity, 30 (4) (2004) 519–526, <https://doi.org/10.1016/j.ultrasmedbio.2004.01.005>.
- [223] I. Beekers, M. Vegter, K.R. Lattwein, F. Mastik, R. Beurskens, A.F. Van Der Steen, N. De Jong, M.D. Verweij, K. Kooiman, Opening of endothelial cell–cell contacts due to sonoporation, 322 (2020) 426–438, <https://doi.org/10.1016/j.jconrel.2020.03.038>.
- [224] M.T. Burgess, T.M. Porter, Control of acoustic cavitation for efficient sonoporation with phase-shift nanoemulsions, 45 (3) (2019) 846–858, <https://doi.org/10.1016/j.ultrasmedbio.2018.12.001>.
- [225] D. Sheng, L. Deng, P. Li, Z. Wang, Q. Zhang, Perfluorocarbon nanodroplets with deep tumor penetration and controlled drug delivery for ultrasound/fluorescence imaging guided breast cancer therapy, 7 (2) (2021) 605–616, <https://doi.org/10.1021/acsbomaterials.0c01333>.
- [226] M.A. Hassan, P. Campbell, T. Kondo, The role of ca²⁺ in ultrasound-elicited bio-effects: progress, perspectives and prospects, 15 (21) (2010) 892–906, <https://doi.org/10.1016/j.drudis.2010.08.005>.
- [227] Z. Fan, R. Kumon, J. Park, C. Deng, Intracellular delivery and calcium transients generated in sonoporation facilitated by microbubbles, 142 (1) (2010) 31–39, <https://doi.org/10.1016/j.jconrel.2009.09.031>.
- [228] I. Beekers, F. Mastik, R. Beurskens, P.Y. Tang, M. Vegter, A.F. Van Der Steen, N. De Jong, M.D. Verweij, K. Kooiman, High-resolution imaging of intracellular calcium fluctuations caused by oscillating microbubbles, 46 (8) (2020) 2017–2029, <https://doi.org/10.1016/j.ultrasmedbio.2020.03.029>.
- [229] J. Park, Z. Fan, R.E. Kumon, M.E. El-Sayed, C.X. Deng, Modulation of intracellular ca²⁺ concentration in brain microvascular endothelial cells in vitro by acoustic cavitation, 36 (7) (2010) 1176–1187, <https://doi.org/10.1016/j.ultrasmedbio.2010.04.006>.
- [230] X. Shen, Z. Song, E. Xu, J. Zhou, F. Yan, Sensitization of nerve cells to ultrasound stimulation through piezo1-targeted microbubbles, 73 (2016) 105494, <https://doi.org/10.1016/j.ulsonch.2021.105494>.
- [231] T.A. Tran, J.Y. Le Guennec, P. Bougnoux, F. Tranquart, A. Bouakaz, Characterization of cell membrane response to ultrasound activated microbubbles, 55 (1) (2008), <https://doi.org/10.1109/TUFFC.2008.615>.
- [232] L.J. Juffermans, O. Kamp, P.A. Dijkmans, C.A. Visser, R.J. Musters, Low-intensity ultrasound-exposed microbubbles provoke local hyperpolarization of the cell membrane via activation of BK(ca) channels, 34 (3) (2008) 502–508, <https://doi.org/10.1016/j.ultrasmedbio.2007.09.010>.
- [233] R. Kumon, M. Aehle, D. Sabens, P. Parikh, Y. Han, D. Kourennyi, C. Deng, Spatiotemporal effects of sonoporation measured by real-time calcium imaging, 35 (3) (2009) 494–506, <https://doi.org/10.1016/j.ultrasmedbio.2008.09.003>.
- [234] B. Helfield, X. Chen, S.C. Watkins, F.S. Villanueva, Transendothelial perforations and the sphere of influence of single-site sonoporation, 46 (7) (2020) 1686–1697, <https://doi.org/10.1016/j.ultrasmedbio.2020.02.017>.
- [235] Y. Zhou, J. Shi, J. Cui, C.X. Deng, Effects of extracellular calcium on cell membrane resealing in sonoporation, 126 (1) (2008) 34–43, <https://doi.org/10.1016/j.jconrel.2007.11.007>.
- [236] P. Qin, L. Xu, Y. Hu, W. Zhong, P. Cai, L. Du, L. Jin, A.C. Yu, Sonoporation-induced depolarization of plasma membrane potential: analysis of heterogeneous impact, 40 (5) (2014) 979–989, <https://doi.org/10.1016/j.ultrasmedbio.2013.11.024>.
- [237] C. Jia, L. Xu, T. Han, P. Cai, A.C. Yu, P. Qin, Generation of reactive oxygen species in heterogeneously sonoporated cells by microbubbles with single-pulse ultrasound, 44 (5) (2018) 1074–1085, <https://doi.org/10.1016/j.ultrasmedbio.2018.01.006>.
- [238] L. Juffermans, P. Dijkmans, R. Musters, C. Visser, O. Kamp, Transient permeabilization of cell membranes by ultrasound-exposed microbubbles is related to formation of hydrogen peroxide, 291 (4) (2006) 595–601, <https://doi.org/10.1152/ajpheart.01120.2005>.
- [239] L.J. Juffermans, A. van Dijk, C.A. Jongenelen, B. Drukarch, A. Reijerkerk, H.E. de Vries, O. Kamp, R.J. Musters, Ultrasound and microbubble-induced intra- and intercellular bioeffects in primary endothelial cells, 35 (11) (2009) 1917–1927, <https://doi.org/10.1016/j.ultrasmedbio.2009.06.1091>.
- [240] B.D. Meijering, L.J. Juffermans, A. Van Wamel, R.H. Henning, I.S. Zuhorn, M. Emmer, A.M. Versteilen, W.J. Paulus, W.H. Van Gilst, K. Kooiman, N. De Jong, R.J. Musters, L.E. Deelman, O. Kamp, Ultrasound and microbubble-targeted delivery of macromolecules is regulated by induction of endocytosis and pore formation, 104 (5) (2009) 679–687, <https://doi.org/10.1161/CIRCRESAHA.108.183806>.
- [241] X. Chen, R.S. Leow, Y. Hu, J.M. Wan, A.C. Yu, Single-site sonoporation disrupts actin cytoskeleton organization, 11 (95) (2014), <https://doi.org/10.1098/rsif.2014.0071>.
- [242] M. Samandari, K. Abrinia, M. Mokhtari-Dizaji, A. Tamayol, Ultrasound induced strain cytoskeleton rearrangement: an experimental and simulation study, 60 (2017) 39–47, <https://doi.org/10.1016/j.jbiomech.2017.06.003>.
- [243] C. Jia, J. Shi, T. Han, A.C. Yu, P. Qin, Spatiotemporal dynamics and mechanisms of actin cytoskeletal re-modeling in cells perforated by ultrasound-driven microbubbles, 48 (5) (2020) 760–777, <https://doi.org/10.1016/j.ultrasmedbio.2021.12.014>.
- [244] Z. Wen, C. Liu, Z. Teng, Q. Jin, Z. Liao, X. Zhu, S. Huo, Ultrasound meets the cell membrane: for enhanced endocytosis and drug delivery, 33 (2023).
- [245] J. Hauser, M. Ellisman, H.-U. Steinau, E. Stefan, M. Dudda, M. Hauser, Ultrasound enhanced endocytotic activity of human fibroblasts, 35 (12) (2009) 2084–2092, <https://doi.org/10.1016/j.ultrasmedbio.2009.06.1090>.
- [246] J.-L. Lee, C.-W. Lo, C. Inserra, J.-C. Béra, W.-S. Chen, Ultrasound enhanced PEI-mediated gene delivery through increasing the intracellular calcium level and PKC- δ protein expression, 31 (9) (2014) 2354–2366, <https://doi.org/10.1007/s11095-014-1332-4>.
- [247] M. Afadzi, S.P. Strand, E.A. Nilssen, S.-E. Måsoy, T.F. Johansen, R. Hansen, B.A. Angelsen, C. de L. Davies, Mechanisms of the ultrasound-mediated intracellular delivery of liposomes and dextrans, 60 (1) (2013) 21–33, <https://doi.org/10.1109/TUFFC.2013.2534>.
- [248] F. Fekri, R.C. Delos Santos, R. Karshafian, C.N. Antonescu, Ultrasound microbubble treatment enhances clathrin-mediated endocytosis and fluid-phase uptake through distinct mechanisms, 11 (6) (2016), <https://doi.org/10.1371/journal.pone.0156754>.
- [249] A. Zeghimi, J.M. Escoffre, A. Bouakaz, Role of endocytosis in sonoporation-mediated membrane permeabilization and uptake of small molecules: a electron microscopy study, 12 (6) (2015), <https://doi.org/10.1088/1478-3975/12/6/066007>.
- [250] A. Delalande, C. Leduc, P. Midoux, M. Postema, C. Pichon, Efficient gene delivery by sonoporation is associated with microbubble entry into cells and the clathrin-dependent endocytosis pathway, 41 (7) (2015) 1913–1926, <https://doi.org/10.1016/j.ultrasmedbio.2015.03.010>.
- [251] M. Derieppe, K. Rojek, J.-M. Escoffre, B.D. de Senneville, C. Moonen, C. Bos, Recruitment of endocytosis in sonopermeabilization-mediated drug delivery: a real-time study, 12 (4) (2015), <https://doi.org/10.1088/1478-3975/12/4/046010>.
- [252] B. Geers, I. Lentacker, A. Alonso, N.N. Sanders, J. Demeester, S. Meairs, S.C. De Smedt, Elucidating the mechanisms behind sonoporation with adeno-associated virus-loaded microbubbles, 8 (6) (2011) 2244–2251, <https://doi.org/10.1021/mp200112y>.
- [253] S. Moosavi Nejad, S.H.R. Hosseini, H. Akiyama, K. Tachibana, Optical observation of cell sonoporation with low intensity ultrasound, 413 (2) (2011) 218–223, <https://doi.org/10.1016/j.bbrc.2011.08.072>.
- [254] B.L. Helfield, X. Chen, B. Qin, S.C. Watkins, F.S. Villanueva, Mechanistic insight into sonoporation with ultrasound-stimulated polymer microbubbles, 43 (11) (2017) 2678–2689, <https://doi.org/10.1016/j.ultrasmedbio.2017.07.017>.
- [255] C. Jia, J. Shi, Yao Yao, T. Han, A.C. Yu, P. Qin, Plasma membrane blebbing dynamics involved in the reversibly perforated cell by ultrasound-driven microbubbles, 47 (3) (2021) 733–750, <https://doi.org/10.1016/j.ultrasmedbio.2020.11.029>.
- [256] S. Roovers, G. Lajoinie, I. De Cock, T. Brans, H. Dewitte, K. Braeckmans, M. Versluis, S.C. De Smedt, I. Lentacker, Sonoprinting of nanoparticle-loaded microbubbles: unraveling the multi-timescale mechanism, 217 (2019) 119250, <https://doi.org/10.1016/j.biomaterials.2019.119250>.
- [257] N. Kudo, High-speed in situ observation system for sonoporation of cells with size- and position-controlled microbubbles, 64 (1) (2017) 273–280, <https://doi.org/10.1109/TUFFC.2016.2606551>.
- [258] J. Shi, T. Han, A.C. Yu, P. Qin, Faster calcium recovery and membrane resealing in repeated sonoporation for delivery improvement, 352 (2020) 385–398, <https://doi.org/10.1016/j.jconrel.2022.10.027>.

- [259] G.A. Curtiss, D.M. Leppinen, Q.X. Wang, J.R. Blake, Ultrasonic cavitation near a tissue layer, 730 (2013) 245–272, <https://doi.org/10.1017/jfm.2013.341>.
- [260] E.-A. Brujan, K. Nahen, P. Schmidt, A. Vogel, Dynamics of laser-induced cavitation bubbles near elastic boundaries: influence of the elastic modulus, 433 (2001) 283–314, <https://doi.org/10.1017/S0022112000003335>.
- [261] H. Yu, C.Y. Tay, W.S. Leong, S.C.W. Tan, K. Liao, L.P. Tan, Mechanical behavior of human mesenchymal stem cells during adipogenic and osteogenic differentiation, 393 (1) (2010) 150–155, <https://doi.org/10.1016/j.bbrc.2010.01.107>.
- [262] F. Chowdhury, S. Na, D. Li, Y.-C. Poh, T.S. Tanaka, F. Wang, N. Wang, Material properties of the cell dictate stress-induced spreading and differentiation in embryonic stem cells, 9 (1) (2010) 82–88, <https://doi.org/10.1038/nmat2563>.
- [263] M. Krieg, G. Fläschner, D. Alsteens, B.M. Gaub, W.H. Roos, G.J.L. Wuite, H.E. Gaub, C. Gerber, Y.F. Dufrène, D.J. Müller, Atomic force microscopy-based mechanobiology, 1 (1) (2018) 41–57, <https://doi.org/10.1038/s42254-018-0001-7>.
- [264] C.F. Guimarães, L. Gasperini, A.P. Marques, R.L. Reis, The stiffness of living tissues and its implications for tissue engineering, 5 (5) (2020) 351–370, <https://doi.org/10.1038/s41578-019-0169-1>.
- [265] B.S. Garra, Elastography: history, principles, and technique comparison, 40 (4) (2015) 680–697, <https://doi.org/10.1007/s00261-014-0305-8>.
- [266] S. Kwon, K.S. Kim, Qualitative analysis of contribution of intracellular skeletal changes to cellular elasticity, 77 (7) (2020) 1345–1355, <https://doi.org/10.1007/s00018-019-03328-6>.
- [267] S. Jalali, M. Tafazzoli-Shadpour, N. Haghhighipour, R. Omidvar, F. Safshekan, Regulation of endothelial cell adherence and elastic modulus by substrate stiffness, 22 (2) (2015) 79–89, <https://doi.org/10.1080/15419061.2016.1265949>.
- [268] M.C. Murphy, D.T. Jones, C.R. Jack, K.J. Glaser, M.L. Senjem, A. Manduca, J.P. Felmlee, R.E. Carter, R.L. Ehman, J. Huston, Regional brain stiffness changes across the Alzheimer's disease spectrum, 10 (2016) 283–290, <https://doi.org/10.1016/j.nicl.2015.12.007>.
- [269] R. Masuzaki, R. Tateishi, H. Yoshida, T. Sato, T. Ohki, T. Goto, H. Yoshida, S. Sato, Y. Sugioka, H. Ikeda, S. Shiina, T. Kawabe, M. Omata, Assessing liver tumor stiffness by transient elastography, 1 (3) (2007) 394–397, <https://doi.org/10.1007/s12072-007-9012-7>.
- [270] S. Salerno, E. Curcio, A. Bader, L. Giorno, E. Drioli, L. De Bartolo, Gas permeable membrane bioreactor for the co-culture of human skin derived mesenchymal stem cells with hepatocytes and endothelial cells, 563 (2018) 694–707, <https://doi.org/10.1016/j.memsci.2018.06.029>.
- [271] S.-T. Kang, Y.-C. Lin, C.-K. Yeh, Mechanical bioeffects of acoustic droplet vaporization in vessel-mimicking phantoms, 21 (5) (2014) 1866–1874, <https://doi.org/10.1016/j.ultrasch.2014.03.007>.
- [272] A. Guibal, C. Boullaran, M. Bruce, M. Vallin, F. Pilleul, T. Walter, J.Y. Scoazec, N. Boublay, J. Dumortier, T. Lefort, Evaluation of shearwave elastography for the characterisation of focal liver lesions on ultrasound, 23 (4) (2013) 1138–1149, <https://doi.org/10.1007/s00330-012-2692-y>.
- [273] S. Iyer, R.M. Gaikwad, V. Subba-Rao, C.D. Woodworth, I. Sokolov, Atomic force microscopy detects differences in the surface brush of normal and cancerous cells, 4 (6) (2009) 389–393, <https://doi.org/10.1038/nnano.2009.77>.
- [274] W. Xu, R. Mezencev, B. Kim, L. Wang, J. McDonald, T. Sulchek, Cell stiffness is a biomarker of the metastatic potential of ovarian cancer cells, 7 (10) (2012) e46609, <https://doi.org/10.1371/journal.pone.0046609>.
- [275] Q. Li, G. Lee, C. Ong, C. Lim, AFM indentation study of breast cancer cells, 374 (4) (2008) 609–613, <https://doi.org/10.1016/j.bbrc.2008.07.078>.
- [276] D. Jaiswal, N. Cowley, Z. Bian, G. Zheng, K.P. Claffey, K. Hoshino, Stiffness analysis of 3d spheroids using microtweezers, 12 (11) (2017) e0188346, <https://doi.org/10.1371/journal.pone.0188346>.
- [277] J.R. Ramos, J. Pabijan, R. Garcia, M. Lekka, The softening of human bladder cancer cells happens at an early stage of the malignancy process, 5 (2014) 447–457, <https://doi.org/10.3762/bjnano.5.52>.
- [278] S.E. Cross, Y.-S. Jin, J. Rao, J.K. Gimzewski, Nanomechanical analysis of cells from cancer patients, 2 (12) (2007) 780–783, <https://doi.org/10.1038/nnano.2007.388>.
- [279] M. Zhang, P. Nigwekar, B. Castaneda, K. Hoyt, J.V. Joseph, A. Di Sant'Agnes, E.M. Messing, J.G. Strang, D.J. Rubens, K.J. Parker, Quantitative characterization of viscoelastic properties of human prostate correlated with histology, 34 (7) (2008) 1033–1042, <https://doi.org/10.1016/j.ultrasmedbio.2007.11.024>.
- [280] W.A. Lam, M.J. Rosenbluth, D.A. Fletcher, Chemotherapy exposure increases leukemia cell stiffness, 109 (8) (2007) 3505–3508, <https://doi.org/10.1182/blood-2006-08-043570>.
- [281] J. Ren, H. Huang, Y. Liu, X. Zheng, Q. Zou, An atomic force microscope study revealed two mechanisms in the effect of anticancer drugs on rate-dependent young's modulus of human prostate cancer cells, 10 (5) (2015) e0126107, <https://doi.org/10.1371/journal.pone.0126107>.
- [282] C.D. Arvanitis, G.B. Ferraro, R.K. Jain, The blood-brain barrier and blood tumour barrier in brain tumours and metastases, 20 (1) (2020) 26–41, <https://doi.org/10.1038/s41568-019-0205-x>.
- [283] N. Sheikov, N. McDannold, N. Vykhodtseva, F. Jolesz, K. Hynynen, Cellular mechanisms of the blood-brain barrier opening induced by ultrasound in presence of microbubbles, 30 (7) (2004) 979–989, <https://doi.org/10.1016/j.ultrasmedbio.2004.04.010>.
- [284] K. Hynynen, N. McDannold, N. Sheikov, F. Jolesz, N. Vykhodtseva, Local and reversible blood–brain barrier disruption by noninvasive focused ultrasound at frequencies suitable for trans-skull sonications, 24 (2005) 12–20, <https://doi.org/10.1016/j.neuroimage.2004.06.046>.
- [285] N. Sheikov, N. McDannold, S. Sharma, K. Hynynen, Effect of focused ultrasound applied with an ultrasound contrast agent on the tight junctional integrity of the brain microvascular endothelium, 34 (7) (2008) 1093–1104, <https://doi.org/10.1016/j.ultrasmedbio.2007.12.015>.
- [286] X. Shang, P. Wang, Z. Zhang, Mechanism of low-frequency ultrasound in opening blood–tumor barrier by tight junction, 43 (3) (2011) 346–369, <https://doi.org/10.1007/s12031-010-9451-9>.
- [287] S. Jalali, Y. Huang, K. Hynynen, Focused ultrasound-mediated bbb disruption is associated with an increase in activation of AKT: experimental study in rats, 10 (1) (2010), <https://doi.org/10.1186/1471-2377-10-114>.
- [288] J. Deng, Q. Huang, F. Wang, Y. Liu, Z. Wang, Z. Wang, Q. Zhang, B. Lei, Y. Cheng, The role of caveolin-1 in blood–brain barrier disruption induced by focused ultrasound combined with microbubbles, 46 (3) (2012) 677–687, <https://doi.org/10.1007/s12031-011-9629-9>.
- [289] M. Olsman, V. Sereti, M. Mühlenpfordt, K.B. Johnsen, T.L. Andresen, A.J. Urquhart, C. De Lange Davies, Focused ultrasound and micro bubble treatment increases delivery of transferrin receptor-targeting liposomes to the brain, 47 (5) (2021) 1343–1355, <https://doi.org/10.1016/j.ultrasmedbio.2021.01.014>.
- [290] R. Pandit, W.K. Koh, R.K.P. Sullivan, T. Palliyaguru, R.G. Parton, J. Götz, Role for caveolin-mediated transcytosis in facilitating transport of large cargoes into the brain via ultrasound, 327 (2020) 667–675, <https://doi.org/10.1016/j.jconrel.2020.09.015>.
- [291] C.-y. Xia, Y.-h. Liu, P. Wang, Y.-x. Xue, Low-frequency ultrasound irradiation increases blood–tumor barrier permeability by transcellular pathway in a rat glioma model, 48 (1) (2012) 281–290, <https://doi.org/10.1007/s12031-012-9770-0>.
- [292] J. Zhang, H. Liu, X. Du, Y. Guo, X. Chen, S. Wang, J. Fang, P. Cao, B. Zhang, Z. Liu, W. Zhang, Increasing of blood–brain tumor barrier permeability through transcellular and paracellular pathways by microbubble-enhanced diagnostic ultrasound in a c6 glioma model, 11 (2017), <https://doi.org/10.3389/fmins.2017.00086>.
- [293] H. Cho, H.-Y. Lee, M. Han, J.-r. Choi, S. Ahn, T. Lee, Y. Chang, J. Park, Localized down-regulation of p-glycoprotein by focused ultrasound and microbubbles induced blood–brain barrier disruption in rat brain, <https://doi.org/10.1038/srep31201>, 2016.
- [294] M. Aryal, K. Fischer, C. Gentile, S. Gitto, Y.-Z. Zhang, N. McDannold, Effects on p-glycoprotein expression after blood–brain barrier disruption using focused ultrasound and microbubbles, 12 (1) (2017), <https://doi.org/10.1371/journal.pone.0166061>.
- [295] H. Choi, E.-H. Lee, M. Han, S.-H. An, J. Park, Diminished expression of p-glycoprotein using focused ultrasound is associated with JNK-dependent signaling pathway in cerebral blood vessels, 13 (1350) (2019), <https://doi.org/10.3389/fmins.2019.01350>.
- [296] Z. Zhang, K. Xu, Y. Bi, G. Yu, S. Wang, X. Qi, H. Zhong, Low intensity ultrasound promotes the sensitivity of rat brain glioma to doxorubicin by down-regulating the expressions of p-glycoprotein and multidrug resistance protein 1 in vitro and in vivo, 8 (8) (2013), <https://doi.org/10.1371/journal.pone.0070685>.
- [297] S. Goutal, M. Gerstenmayer, S. Auvity, F. Caillé, S. Mériaux, I. Buvat, B. Larrat, N. Tournier, Physical blood–brain barrier disruption induced by focused ultrasound does not overcome the transporter-mediated efflux of erlotinib, 292 (2018) 210–220, <https://doi.org/10.1016/j.jconrel.2018.11.009>.
- [298] S. Goutal, A. Novell, S. Leterrier, L. Breuil, E. Selingue, M. Gerstenmayer, S. Marie, B. Saubaméa, F. Caillé, O. Langer, C. Truillet, B. Larrat, N. Tournier, Imaging the impact of blood–brain barrier disruption induced by focused ultrasound on p-glycoprotein function, 361 (2023) 483–492, <https://doi.org/10.1016/j.jconrel.2023.08.012>.
- [299] C.T. Curley, B.P. Mead, K. Negron, N. Kim, W.J. Garrison, G.W. Miller, K.M. Kingsmore, E.A. Thim, J. Song, J.M. Munson, A.L. Klibanov, J.S. Suk, J. Hanes, R.J. Price, Augmentation of brain tumor interstitial flow via focused ultrasound promotes brain-penetrating nanoparticle dispersion and transfection, 6 (18) (2020), <https://doi.org/10.1126/sciadv.aay1344>.
- [300] C.D. Arvanitis, V. Askoxylakis, Y. Guo, M. Datta, J. Klopper, G.B. Ferraro, M.O. Bernabeu, D. Fukumura, N. McDannold, R.K. Jain, Mechanisms of enhanced drug delivery in brain metastases with focused ultrasound-induced blood–tumor barrier disruption, 115 (37) (2018) 8717–8726, <https://doi.org/10.1073/pnas.1807105115>.
- [301] B. Baseri, J. Choi, Y.-S. Tung, E. Konofagou, Multi-modality safety assessment of blood–brain barrier opening using focused ultrasound and definity microbubbles: a short-term study, 36 (9) (2010) 1445–1459, <https://doi.org/10.1016/j.ultrasmedbio.2010.06.005>.
- [302] C. Poon, M. Mühlenpfordt, M. Olsman, S. Kotopoulos, C. De Lange Davies, K. Hynynen, Real-time intravital multiphoton microscopy to visualize focused ultrasound and microbubble treatments to increase blood–brain barrier permeability, 180 (2022) 62235, <https://doi.org/10.3791/62235>.
- [303] L.H. Treat, N. McDannold, N. Vykhodtseva, Y. Zhang, K. Tam, K. Hynynen, Targeted delivery of doxorubicin to the rat brain at therapeutic levels using MRI-guided focused ultrasound, 121 (4) (2007) 901–907, <https://doi.org/10.1002/jic.22732>.
- [304] J. Mei, Y. Cheng, Y. Song, Y. Yang, F. Wang, Y. Liu, Z. Wang, Experimental study on targeted methotrexate delivery to the rabbit brain via magnetic

- resonance imaging-guided focused ultrasound, 28 (7) (2009) 871–880, <https://doi.org/10.7863/jum.2009.28.7.871>.
- [305] X. Wang, P. Liu, W. Yang, L. Li, P. Li, Z. Liu, Z. Zhuo, Y. Gao, Microbubbles coupled to methotrexate-loaded liposomes for ultrasound-mediated delivery of methotrexate across the blood–brain barrier, 9 (2014) 4899–4909, <https://doi.org/10.2147/IJN.S69845>.
- [306] M. Aryal, J. Park, N. Vykhotseva, Y.-Z. Zhang, N. McDannold, Enhancement in blood-tumor barrier permeability and delivery of liposomal doxorubicin using focused ultrasound and microbubbles: evaluation during tumor progression in a rat glioma model, 60 (6) (2015) 2511–2527, <https://doi.org/10.1088/0031-9155/60/6/2511>.
- [307] K. Baccarria, M. Canney, L. Goldwirt, C. Fernandez, J. Piquet, M.-C. Perier, C. Lafon, J.-Y. Chapelon, A. Carpentier, Ultrasound-induced opening of the blood-brain barrier to enhance temozolomide and irinotecan delivery: an experimental study in rabbits, 124 (6) (2016) 1602–1610, <https://doi.org/10.3171/2015.4.JNSI42893>.
- [308] J. Park, M. Aryal, N. Vykhotseva, Y.-Z. Zhang, N. McDannold, Evaluation of permeability, doxorubicin delivery, and drug retention in a rat brain tumor model after ultrasound-induced blood-tumor barrier disruption, 28 (250) (2017) 77–85, <https://doi.org/10.1016/j.jconrel.2016.10.011>.
- [309] S. Alli, C.A. Figueiredo, B. Golbourn, N. Sabha, M.Y. Wu, A. Bondoc, A. Luck, D. Coluccia, C. Maslink, C. Smith, H. Wurdak, K. Hynynen, M. O'Reilly, J.T. Rutka, Brainstem blood brain barrier disruption using focused ultrasound: a demonstration of feasibility and enhanced doxorubicin delivery, 10 (281) (2018) 29–41, <https://doi.org/10.1016/j.jconrel.2018.05.005>.
- [310] M. Kinoshita, N. McDannold, F.A. Jolesz, K. Hynynen, Noninvasive localized delivery of herceptin to the mouse brain by MRI-guided focused ultrasound-induced blood–brain barrier disruption, 103 (31) (2006) 11719–11723, <https://doi.org/10.1073/pnas.0604318103>.
- [311] V.L. Tran, A. Novell, N. Tournier, M. Gerstenmayer, A. Schweitzer-Chaput, C. Mateos, B. Jego, A. Bouleau, H. Nozach, A. Winkeler, B. Kuhnast, B. Larraz, C. Truillet, Impact of blood-brain barrier permeabilization induced by ultrasound associated to microbubbles on the brain delivery and kinetics of cetuximab: an immunoPET study using 89Zr-cetuximab, 328 (2020) 304–312, <https://doi.org/10.1016/j.jconrel.2020.08.047>.
- [312] Y. Liu, Y. Gong, W. Xie, A. Huang, X. Yuan, H. Zhou, X. Zhu, X. Chen, J. Liu, J. Liu, X. Qin, Microbubbles in combination with focused ultrasound for the delivery of quercetin-modified sulfur nanoparticles through the blood brain barrier into the brain parenchyma and relief of endoplasmic reticulum stress to treat Alzheimer's disease, 12 (11) (2020) 6498–6511, <https://doi.org/10.1039/C9NR09713A>.
- [313] C. Brighi, L. Reid, A.L. White, L.A. Genovesi, M. Kojic, A. Millar, Z. Bruce, B.W. Day, S. Rose, A.K. Whittaker, S. Puttick, MR-guided focused ultrasound increases antibody delivery to nonenhancing high-grade glioma, 2 (1) (2020), <https://doi.org/10.1093/naojnl/vdaa030>.
- [314] B.P. Mead, P. Mastorakos, J.S. Suk, A.L. Kibanov, J. Hanes, R.J. Price, Targeted gene transfer to the brain via the delivery of brain-penetrating DNA nanoparticles with focused ultrasound, 223 (2016) 109–117, <https://doi.org/10.1016/j.jconrel.2015.12.034>.
- [315] K. Ogawa, N. Kato, M. Yoshida, T. Hiu, T. Matsuo, S. Mizukami, D. Omata, R. Suzuki, K. Maruyama, H. Mukai, S. Kawakami, Focused ultrasound/microbubbles-assisted BBB opening enhances LNP-mediated mRNA delivery to brain, 348 (2022) 34–41, <https://doi.org/10.1016/j.jconrel.2022.05.042>.
- [316] Q. Huang, J. Deng, F. Wang, S. Chen, Y. Liu, Z. Wang, Z. Wang, Y. Cheng, Targeted gene delivery to the mouse brain by MRI-guided focused ultrasound-induced blood–brain barrier disruption, 233 (1) (2012) 350–356, <https://doi.org/10.1016/j.expneurol.2011.10.027>.
- [317] C.M. Gorick, V.R. Breza, K.M. Nowak, V.W. Cheng, D.G. Fisher, A.C. Debski, M.R. Hoch, Z.E. Demir, N.M. Tran, M.R. Schwartz, N.D. Sheybani, R.J. Price, Applications of focused ultrasound-mediated blood-brain barrier opening, 191 (2022) 114583, <https://doi.org/10.1016/j.addr.2022.114583>.
- [318] S. Schoen, M.S. Kilinc, H. Lee, Y. Guo, F.L. Degertekin, G.F. Woodworth, C. Arvanitis, Towards controlled drug delivery in brain tumors with microbubble-enhanced focused ultrasound, 180 (2022) 114043, <https://doi.org/10.1016/j.addr.2021.114043>.
- [319] A. Drea, N. Lemaire, G. Bouchoux, L. Goldwirt, M. Canney, L. Goli, A. Bouzidi, C. Schmitt, J. Guehenec, M. Verreault, M. Sanson, J.-Y. Delattre, K. Mokhtari, F. Sottolini, A. Carpentier, A. Idhah, Temporary blood–brain barrier disruption by low intensity pulsed ultrasound increases carboplatin delivery and efficacy in preclinical models glioblastoma, 144 (1) (2019) 33–41, <https://doi.org/10.1007/s11060-019-03204-0>.
- [320] N. McDannold, Y. Zhang, J.G. Supko, C. Power, T. Sun, C. Peng, N. Vykhotseva, A.J. Golby, D.A. Reardon, Acoustic feedback enables safe and reliable carboplatin delivery across the blood-brain barrier with a clinical focused ultrasound system and improves survival in a rat glioma model, 9 (21) (2019) 6284–6299, <https://doi.org/10.7150/thno.35892>.
- [321] L.H. Treat, N. McDannold, Y. Zhang, N. Vykhotseva, K. Hynynen, Improved anti-tumor effect of liposomal doxorubicin after targeted blood-brain barrier disruption by MRI-guided focused ultrasound in rat glioma, 38 (10) (2012) 1716–1725, <https://doi.org/10.1016/j.ultrasmedbio.2012.04.015>.
- [322] M. Aryal, N. Vykhotseva, Y.-Z. Zhang, J. Park, N. McDannold, Multiple treatments with liposomal doxorubicin and ultrasound-induced disruption of blood–tumor and blood–brain barriers improve outcomes in a rat glioma model, 169 (1) (2013) 103–111, <https://doi.org/10.1016/j.jconrel.2013.04.007>.
- [323] R.-J. Park, Y.-Z. Zhang, N. Vykhotseva, N. McDannold, Ultrasound-mediated blood-brain/blood-tumor barrier disruption improves outcomes with trastuzumab in a breast cancer brain metastasis model, 163 (3) (2012) 277–284, <https://doi.org/10.1016/j.jconrel.2012.09.007>.
- [324] Y.-Z. Zhao, Q. Lin, H.L. Wong, X.-T. Shen, W. Yang, H.-L. Xu, K.-L. Mao, F.-R. Tian, H.-J. Yang, J. Xu, J. Xiao, C.-T. Lu, Glioma-targeted therapy using cilengitide nanoparticles combined with UTMD enhanced delivery, 224 (2016) 112–125, <https://doi.org/10.1016/j.jconrel.2016.01.015>.
- [325] J.F. Jordao, C.A. Ayala-Grosso, K. Markham, Y. Huang, R. Chopra, J. McLaurin, K. Hynynen, I. Aubert, Antibodies targeted to the brain with image-guided focused ultrasound reduces amyloid- β plaque load in the TgCRND8 mouse model of Alzheimer's disease, 5 (5) (2010), <https://doi.org/10.1371/journal.pone.0010549>.
- [326] B.P. Mead, N. Kim, G.W. Miller, D. Hodges, P. Mastorakos, A.L. Kibanov, J.W. Mandell, J. Hirsh, J.S. Suk, J. Hanes, R.J. Price, Novel focused ultrasound gene therapy approach noninvasively restores dopaminergic neuron function in a rat Parkinson's disease model, 17 (6) (2017) 3533–3542, <https://doi.org/10.1021/acs.nanolett.7b00616>.
- [327] C.-Y. Lin, Y.-C. Lin, C.-Y. Huang, S.-R. Wu, C.-M. Chen, H.-L. Liu, Ultrasound-responsive neurotrophic factor-loaded microbubble-liposome complex: preclinical investigation for Parkinson's disease treatment, 321 (2020) 518–528, <https://doi.org/10.1016/j.jconrel.2020.02.044>.
- [328] N. McDannold, N. Vykhotseva, K. Hynynen, Blood-brain barrier disruption induced by focused ultrasound and circulating preformed microbubbles appears to be characterized by the mechanical index, 34 (5) (2008) 834–840, <https://doi.org/10.1016/j.ultrasmedbio.2007.10.016>.
- [329] M.A. O'Reilly, Y. Huang, K. Hynynen, The impact of standing wave effects on transcranial focused ultrasound disruption of the blood-brain barrier in a rat model, 55 (18) (2010) 5251–5267, <https://doi.org/10.1088/0031-9155/55/18/001>.
- [330] A.M. Sonabend, A. Gould, C. Amidei, R. Ward, K.A. Schmidt, D.Y. Zhang, C. Gomez, J.F. Bebawy, B.P. Liu, G. Bouchoux, C. Desseaux, I.B. Helenowski, R.V. Lukas, K. Dxit, P. Kumthekar, V.A. Arrieta, M.S. Lesniak, A. Carpentier, H. Zhang, M. Muzzio, M. Canney, R. Stupp, Repeated blood–brain barrier opening with an implantable ultrasound device for delivery of albumin-bound paclitaxel in patients with recurrent glioblastoma: a phase 1 trial, 24 (5) (2023) 509–522, [https://doi.org/10.1016/S1470-2045\(23\)00112-2](https://doi.org/10.1016/S1470-2045(23)00112-2).
- [331] K.-T. Chen, W.-Y. Chai, Y.-J. Lin, C.-J. Lin, P.-Y. Chen, H.-C. Tsai, C.-Y. Huang, J.S. Kuo, H.-L. Liu, K.-C. Wei, Neuronavigation-guided focused ultrasound for transcranial blood-brain barrier opening and immunostimulation in brain tumors, 7 (6) (2021), <https://doi.org/10.1126/sciadv.abd0772>.
- [332] H. Park, M.J. Kim, H.H. Jung, W.S. Chang, H.S. Choi, I. Rachmilevitch, E. Zadicario, J.W. Chang, Safety and feasibility of multiple blood-brain barrier disruptions for the treatment of glioblastoma in patients undergoing standard adjuvant chemotherapy, 134 (2) (2020) 475–483, <https://doi.org/10.3171/2019.10.JNS192206>.
- [333] P. Anastasiadis, D. Gandhi, Y. Guo, A.-K. Ahmed, S.M. Bentzen, C. Arvanitis, G.F. Woodworth, Localized blood–brain barrier opening in infiltrating gliomas with MRI-guided acoustic emissions-controlled focused ultrasound, 118 (37) (2021), <https://doi.org/10.1073/pnas.2103280118>.
- [334] Y. Meng, R.M. Reilly, R.C. Pezo, M. Trudeau, A. Sahgal, A. Singnurkar, J. Perry, S. Myrehaug, C.B. Pople, B. Davidson, M. Llinas, C. Hyen, Y. Huang, C. Hamani, S. Suppiah, K. Hynynen, N. Lipsman, MR-guided focused ultrasound enhances delivery of trastuzumab to her2-positive brain metastases, 13 (615) (2021), <https://doi.org/10.1126/scitranslmed.abj4011>.
- [335] A.R. Rezaei, M. Ranjan, P.-F. D'Haese, M.W. Haut, J. Carpenter, U. Najib, R.I. Mehta, J.L. Chazen, Z. Zibly, J.R. Yates, S.L. Hodder, M. Kaplitt, Noninvasive hippocampal blood–barrier opening in Alzheimer's disease with focused ultrasound, 117 (17) (2020) 9180–9182, <https://doi.org/10.1073/pnas.2002571117>.
- [336] P.-F. D'Haese, M. Ranjan, A. Song, M.W. Haut, J. Carpenter, G. Dieb, U. Najib, P. Wang, R.I. Mehta, J.L. Chazen, S. Hodder, D. Claassen, M. Kaplitt, A.R. Rezaei, β -amyloid plaque reduction in the hippocampus after focused ultrasound-induced blood–brain barrier opening in Alzheimer's disease, 14 (2020) 593672, <https://doi.org/10.3389/fnhum.2020.593672>.
- [337] S.H. Park, K. Baik, S. Jeon, W.S. Chang, B. Seok Ye, J.W. Chang, Extensive frontal focused ultrasound mediated blood–brain barrier opening for the treatment of Alzheimer's disease: a proof-of-concept study, 10 (1) (2021) 44, <https://doi.org/10.1186/s40035-021-00269-8>.
- [338] C. Gasca-Salas, B. Fernández-Rodríguez, J.A. Pineda-Pardo, R. Rodríguez-Rojas, I. Obeso, F. Hernández-Fernández, M. del Álamo, D. Mata, P. Guida, C. Ordás-Bandera, J.I. Montero-Roblas, R. Martínez-Fernández, G. Foffani, I. Rachmilevitch, J.A. Obeso, Blood-brain barrier opening with focused ultrasound in Parkinson's disease dementia, 12 (1) (2021) 779, <https://doi.org/10.1038/s41467-021-21022-9>.
- [339] S. Roovers, T. Segers, G. Lajoie, J. Deprez, M. Versluis, S.C. De Smedt, I. Lentacker, The role of ultrasound-driven microbubble dynamics in drug delivery: from microbubble fundamentals to clinical translation, 35 (31) (2019) 10173–10191, <https://doi.org/10.1021/acs.langmuir.8b03779>.
- [340] L. Yao, T. Luo, G. Yang, J. Yin, H. Li, Z. Liu, An experimental study: treatment of subcutaneous c6 glioma in rats using acoustic droplet vaporization, 42 (9) (2023) 1951–1963, <https://doi.org/10.1002/jum.16212>.

- [341] R. Song, C. Zhang, F. Teng, J. Tu, X. Guo, Z. Fan, Y. Zheng, D. Zhang, Cavitation-facilitated transmembrane permeability enhancement induced by acoustically vaporized nanodroplets, 79 (2021) 105790, <https://doi.org/10.1016/j.ultronch.2021.105790>.
- [342] S.-Y. Wu, S.M. Fix, C.B. Arena, C.C. Chen, W. Zheng, O.O. Olumolade, V. Papadopoulou, A. Novell, P.A. Dayton, E.E. Konofagou, Focused ultrasound-facilitated brain drug delivery using optimized nanodroplets: vaporization efficiency dictates large molecular delivery, 63 (3) (2018) 035002, <https://doi.org/10.1088/1361-6560/aaa30d>.
- [343] J. Shi, P.W. Kantoff, R. Wooster, O.C. Farokhzad, Cancer nanomedicine: progress, challenges and opportunities, 17 (1) (2017) 20–37, <https://doi.org/10.1038/nrc.2016.108>.
- [344] R. Sun, J. Xiang, Q. Zhou, Y. Piao, J. Tang, S. Shao, Z. Zhou, Y.H. Bae, Y. Shen, The tumor EPR effect for cancer drug delivery: current status, limitations, and alternatives, 191 (2022) 114614, <https://doi.org/10.1016/j.addr.2022.114614>.
- [345] V. Frenkel, Ultrasound mediated delivery of drugs and genes to solid tumors, 60 (10) (2008) 1193–1208, <https://doi.org/10.1016/j.addr.2008.03.007>.
- [346] S. Snipstad, K. Vikedal, M. Maardalen, A. Kurbatskaya, E. Sulheim, C. de Lange Davies, Ultrasound and microbubbles to beat barriers in tumors: improving delivery of nanomedicine, 177 (2021) 113847, <https://doi.org/10.1016/j.addr.2021.113847>.
- [347] S. Snipstad, S. Berg, Y. Mørch, A. Bjørkøy, E. Sulheim, R. Hansen, I. Grimstad, A. van Wamel, A.F. Maaland, S.H. Trop, C. de Lange Davies, Ultrasound improves the delivery and therapeutic effect of nanoparticle-stabilized microbubbles in breast cancer xenografts, 43 (11) (2017) 2651–2669, <https://doi.org/10.1016/j.ultrasmedbio.2017.06.029>.
- [348] F. Yan, L. Li, Z. Deng, Q. Jin, J. Chen, W. Yang, C.-K. Yeh, J. Wu, R. Shandas, X. Liu, H. Zheng, Paclitaxel-liposome-microbubble complexes as ultrasound-triggered therapeutic drug delivery carriers, 166 (3) (2013) 246–255, <https://doi.org/10.1016/j.jconrel.2012.12.025>.
- [349] T.-Y. Wang, J.W. Choe, K. Pu, R. Devulapally, S. Bachawal, S. Machtaler, S.M. Chowdhury, R. Luong, L. Tian, B. Khuri-Yakub, J. Rao, R. Paulmurugan, J.K. Willmann, Ultrasound-guided delivery of microRNA loaded nanoparticles into cancer, 203 (2015) 99–108, <https://doi.org/10.1016/j.jconrel.2015.02.018>.
- [350] C.-Y. Lin, J.-R. Li, H.-C. Tseng, F.-M. Wu, W.-L. Lin, Enhancement of focused ultrasound with microbubbles on the treatments of anticancer nanodrug in mouse tumors, 8 (6) (2012) 900–907, <https://doi.org/10.1016/j.nano.2011.10.005>.
- [351] B. Theek, M. Baues, T. Ojha, D. Möckel, S.K. Veettil, J. Steitz, L. van Bloois, G. Storm, F. Kiessling, T. Lammers, Sonoporation enhances liposome accumulation and penetration in tumors with low EPR, 231 (2016) 77–85, <https://doi.org/10.1016/j.jconrel.2016.02.021>.
- [352] M. Olsman, V. Sereti, K. Andreassen, S. Snipstad, A. van Wamel, R. Eliassen, S. Berg, A.J. Urquhart, T.L. Andresen, C. de Lange Davies, Ultrasound-mediated delivery enhances therapeutic efficacy of MMP sensitive liposomes, 325 (2020) 121–134, <https://doi.org/10.1016/j.jconrel.2020.06.024>.
- [353] S. Kotopoulos, G. Dimcevski, O.H. Gilja, D. Hoem, M. Postema, Treatment of human pancreatic cancer using combined ultrasound, microbubbles, and gemcitabine: a clinical case study, 40 (7) (2013) 072902, <https://doi.org/10.1118/1.4808149>.
- [354] N. Rapoport, K.-H. Nam, R. Gupta, Z. Gao, P. Mohan, A. Payne, N. Todd, X. Liu, T. Kim, J. Shea, C. Scaife, D.L. Parker, E.-K. Jeong, A.M. Kennedy, Ultrasound-mediated tumor imaging and nanotherapy using drug loaded, block copolymer stabilized perfluorocarbon nanoemulsions, 153 (1) (2011) 4–15, <https://doi.org/10.1016/j.jconrel.2011.01.022>.
- [355] C.-P. Spatarelu, S. Jandhyala, G.P. Luke, Dual-drug loaded ultrasound-responsive nanodroplets for on-demand combination chemotherapy, 133 (2023), <https://doi.org/10.1016/j.ultras.2023.107056>.
- [356] L.C. Moyer, K.F. Timbie, P.S. Sheeran, R.J. Price, G.W. Miller, P.A. Dayton, High-intensity focused ultrasound ablation enhancement in vivo via phase-shift nanodroplets compared to microbubbles, 3 (1) (2015) 7, <https://doi.org/10.1186/s40349-015-0029-4>.
- [357] D. Pajek, A. Burgess, Y. Huang, K. Hynynen, High-intensity focused ultrasound sonothrombolysis: the use of perfluorocarbon droplets to achieve clot lysis at reduced acoustic power, 40 (9) (2014) 2151–2161, <https://doi.org/10.1016/j.ultrasmedbio.2014.03.026>.